Light and elevated Temperature Induced Degradation (LeTID) of the Carrier Lifetime in Multicrystalline Silicon

Von der Fakultät für Mathematik und Physik

der Gottfried Wilhelm Leibniz Universität Hannover

zur Erlangung des Grades

Doktor der Naturwissenschaften

Dr. rer. nat.

genehmigte Dissertation

von

Dennis Bredemeier, M.Sc.

geboren am 21.08.1990 in Bremen

2020

Referent:	Prof. Dr. Jan Schmidt
Korreferenten:	Prof. Dr. Herbert Pfnür und Prof. Dr. Arthur Weeber
Tag der Promotion:	13.03.2020

Kurzzusammenfassung

Aus multikristallinem Silizium hergestellte Solarzellen zeigen eine ausgeprägte Degradation ihrer Energieumwandlungseffizienz unter Beleuchtung bei erhöhter Temperatur. In der Literatur wird dieses Phänomen häufig als LeTID-Effekt ("Light and elevated Temperature Induced Degradation") bezeichnet. Diese Arbeit untersucht sowohl die Eigenschaften als auch die Ursache der Degradation.

Diese Arbeit zeigt zum ersten Mal, dass die Degradation der Effizienz auf eine Degradation der Volumenlebensdauer des Siliziummaterials zurückgeführt werden kann. Wird die Beleuchtung bei erhöhter Temperatur über die maximale Degradation hinaus fortgesetzt, zeigt sich eine Regeneration der Ladungsträgerlebensdauer auf Werte vergleichbar mit den initialen Werten vor Degradation. Auf diesen Erkenntnissen basierend werden Untersuchungen auf Silizium-Lebensdauerproben durchgeführt, um die fundamentale Defektphysik und den Einfluss von Prozessschritten sowie den Bedingungen der Probenbeleuchtung zu evaluieren.

Kurzzeitige Hochtemperaturbehandlungen, wie sie typischerweise als letzter Prozessschritt während der Herstellung von Solarzellen angewendet werden, zeigen einen starken Einfluss auf das Ausmaß der Degradation. Mit steigender Spitzentemperatur während der Temperaturbehandlung steigt das Ausmaß der Degradation an. Darüber hinaus zeigen Proben, welche zuvor einen Phosphor-Getterschritt erhalten haben, eine deutlich verminderte Degradation gegenüber Proben, welche diesen Prozessschritt nicht erhalten haben. Weiterhin hat die Probendicke einen großen Einfluss auf das Ausmaß der Degradation sowie auf die Rate der Regeneration. Dünnere Proben zeigen eine weniger ausgeprägte Degradation und eine früher einsetzende Regeneration als dickere Proben.

Schließlich wird der Einfluss von verschiedenen Schichten zur Oberflächenpassivierung untersucht. Nur Proben, bei denen wasserstoffreiches Siliziumnitrid (SiN_x) Teil der Oberflächenpassivierung ist, zeigen eine ausgeprägte Degradation der Ladungsträgerlebensdauer. Von diesem Ergebnis ausgehend wird der Einfluss von SiN_x-Passivierschichten im Detail untersucht. Im SiN_x gebundener Wasserstoff diffundiert während der schnellen Temperaturbehandlung aus der Schicht in das Siliziumvolumen hinein. Zum ersten Mal wird gezeigt, dass das Ausmaß der beobachteten Degradation direkt mit der Konzentration des eindiffundierten Wasserstoffs korreliert. Dies zeigt deutlich, dass Wasserstoff direkt am LeTID-Mechanismus beteiligt ist.

Aufbauend auf den experimentellen Ergebnissen dieser Arbeit wird ein Defektmodell entwickelt. Das Defektmodell beinhaltet schwach oder nicht rekombinationsaktive Metall-Wasserstoff-Komplexe als wahrscheinliche Vorstufe für den die Lebensdauer limitierenden Defekt. Die Degradation wird durch eine Dissoziation des Metall-Wasserstoff-Komplexes erklärt und die Regeneration durch die Diffusion des rekombinationsaktiven Metalls zu den Waferoberflächen. Messungen an Proben mit unterschiedlichen Dicken erlauben die Bestimmung des Diffusionskoeffizienten des Metalls in Silizium zu $(5 \pm 2) \times 10^{-11}\ \mathrm{cm^2\ s^{-1}}$ bei einer Temperatur von 75 °C. Im Ergebnis sind Kobalt und Nickel wahrscheinliche Kandidaten für die metallische Spezies.

Abstract

Solar cells fabricated on multicrystalline silicon show a pronounced degradation of their energy conversion efficiency under illumination at elevated temperature. This effect is frequently denoted LeTID ('Light and elevated Temperature Induced Degradation') in the literature. Within this thesis, the properties and the root cause of the degradation phenomenon is investigated in detail.

It is shown for the first time that the degradation in efficiency is caused by a pronounced degradation of the carrier lifetime in the silicon bulk. Upon prolonged illumination at elevated temperature, a regeneration of the carrier lifetime is observed which leads to lifetime values comparable to the inital value. Based on this finding, a series of comprehensive lifetime studies is performed to elucidate the fundamental defect physics and the impact of process steps as well as the illumination conditions on the carrier lifetime degradation and regeneration.

Rapid thermal annealing, which is typically applied as the last process step during solar cell fabrication, is found to have a strong impact on the degradation extent. The degradation extent strongly increases with increasing peak temperature. In contrast to that, samples which receive a phosphorus gettering treatment show a less pronounced degradation than samples without phosphorus gettering. Furthermore, the degradation extent and the regeneration rate strongly depend on the wafer thickness. Thin samples show a less pronounced degradation and the regeneration of the carrier lifetime sets in earlier.

Finally, we show that the surface passivation scheme of the lifetime samples affects the LeTID effect. Only samples with hydrogen-rich silicon nitride (SiN_x) films being part of the surface passivation scheme show the most pronounced degradation of the carrier lifetime. Based on these findings, the role of SiN_x passivation layers on the lifetime-limiting defect is examined in detail. Hydrogen bound within the SiN_x films diffuses into the silicon bulk upon rapid thermal annealing. For the first time, a direct correlation between the hydrogen concentration in the silicon bulk and the degradation extent is shown, clearly proofing that hydrogen is directly involved in the LeTID mechanism.

Finally, a defect model based on the experimental findings of this thesis is derived. The defect model includes weakly or even non-recombination active metal-hydrogen complexes as the most likely precursor for the lifetime-limiting defect. The degradation is caused by a dissociation of the metal-hydrogen complexes, whereas the regeneration is caused by the diffusion of the recombination active metal to the wafer surfaces. Measurements on samples with different thicknesses point towards a diffusion coefficient of $(5 \pm 2) \times 10^{-11}\,\mathrm{cm}^2\,\mathrm{s}^{-1}$ of the metallic species in silicon at 75 °C. In conclusion, cobalt and nickel are likely candidates for the metallic species.

Schlagwörter: Solarzellen, Silizium, Lichtinduzierte Degradation, Ladungsträgerlebensdauer, Rekombination, Siliziumnitrid, Defekte

Keywords: solar cells, silicon, light-induced degradation, charge carrier lifetime, recombination, silicon nitride, defects

Contents

Chapter 1

Introduction

The transition of the energy system from fossil fuels to renewable energy sources is a great challenge. Photovoltaic (PV) energy generation with its fast growing market and decreasing costs plays a major role in the energy transition. A cumulative global PV installation of 515 GW at the end of 2018 with a total power generation of 443 TWh in 2017 underlines the relevance of photovoltaics [1]. Levelized costs of energy (LCOE) in the range from 4 to 7 ct€ for PV power plants in germany make PV electricity generation also very attractive from an economical point of view [1].

The global production share of crystalline silicon PV is around 95 percent with a record efficiency for monocrystalline silicon solar cells of 26.7 % [1, 2]. However, multicrystalline silicon (mc-Si) holds more than half of the world's market share, because of lower fabrication costs of mc-Si wafers [3]. The drawback of using mc-Si wafers is a lower energy conversion efficiency due to increased recombination because of increased impurity concentrations and crystallographic defects. The current record efficiency for an mc-Si solar cell is 22.3 % and thus considerably lower than for monocrystalline silicon solar cells [2, 4]. To achieve mc-Si solar cells which are nevertheless competetive with monocrystalline silicon solar cells, the PV industry shifts towards mc-Si solar cells with a cell structure that enables high efficiencies. This is the passivated emitter and rear solar cell (PERC), which enables higher energy conversion efficiencies than the full aluminium back surface field structure (Al-BSF). In contrast to the Al-BSF solar cells, the PERC solar cells feature a rear-side Al_2O_3/SiN_x stack passivation [5].

In 2012, Ramspeck et al. [6] reported that mc-Si PERC solar cells show a pronounced light-induced degradation upon illumination at elevated temperature (> 50 °C). They were not able to explain this effect by known degradation mechanisms such as the boron-oxygen defect activation [7–9] or the iron-boron pair dissociation [10, 11] and hence attributed the effect to a new degradation mechanism [6]. Since the degradation is particularly pronounced on mc-Si solar cells with an Al_2O_3/SiN_x-passivated rear surface, this degradation mechanism strongly interferes with the introduction of mc-Si PERC solar cells into the market [6, 12, 13]. The increasing number of studies on this phenomenon in recent years underlines the practical and fundamental relevance of the effect, which is frequently denoted 'LeTID' (Light and elevated Temperature Induced Degradation) in the literature [13].

Before the beginning of this thesis, there were only two reports published on LeTID of mc-Si solar cells in the literature. As described above, Ramspeck et al. [6] were the first who reported on an unexpected and pronounced efficiency degradation of mc-Si PERC solar cells under illumination at elevated temperature. Subsequently, Fertig et al. [12] showed degradation experiments on three different mc-Si solar cell architectures and concluded that an aluminium oxide surface passivation might play a role in the degradation mechanism.

The focus of this thesis is to reveal the fundamental physics behind the efficiency degradation in mc-Si PERC solar cells. It is shown that a pronounced change in the bulk carrier lifetime causes LeTID and eventually, upon further illumination at elevated temperature, a regeneration. A detailed analysis of the impact of processing steps on the carrier lifetime evolution as well as the detailed kinetics of the degradation and regeneration processes enables us to narrow down the possible root causes of the phenomenon. Furthermore, we introduce a LeTID defect model, which consistently describes the experimental findings presented in this thesis and in the literature.

Chapter 2 starts with an overview of the fabrication proccesses of multicrystalline silicon (mc-Si), Czochralski-grown silicon (Cz-Si) and float-zone silicon (FZ-Si). Subsequently, intrinsic semiconductors are introduced and the doping of such to utilize them for technological applications is elucidated. In the following, the different recombination channels for excess charge carriers are described.

Chapter 3 gives an overview of techniques used for the characterization of silicon samples and thin film coatings. At first, integral and spatially resolved measurement techniques for the carrier lifetime of silicon wafers are described. The chapter concludes with an introduction to thin film characterization techniques such as ellipsometry for the determination of film thickness and refractive index, Fourier Transform Infrared Spectroscopy (FTIR) and Nuclear Reaction Analysis (NRA) for the determination of hydrogen concentrations and Rutherford Backscattering Spectroscopy (RBS) for the determination of the composition and areal atomic density of the films.

Chapter 4 starts with an overview of processing steps used for the fabrication of silicon lifetime samples. In the following, the degradation and regeneration of the carrier lifetime in mc-Si lifetime samples is investigated in detail. The impact of sample processing steps on the defect activation kinetics as well as on the LeTID extent is investigated. Furthermore, the impact of illumination intensity and sample temperature on the defect activation kinetics is analyzed.

Chapter 5 introduces the properties of hydrogen-rich silicon nitride coatings and the in-diffusion of hydrogen from these coatings into the silicon bulk. Since the results of chapter 4 point towards an involvement of hydrogen in the defect physics of the carrier lifetime instability in mc-Si, this chapter investigates the impact of hydrogen-rich silicon nitride films on the degradation extent. A method for the determination of hydrogen concentrations in boron-doped monocrystalline silicon is introduced.

Chapter 6 combines the results of the previous chapters in a defect model that describes both the carrier lifetime degradation and regeneration. Indications for the involvement of hydrogen as well as the involvement of a metallic impurity are combined in a defect model, assuming that metal-hydrogen complexes play a major role. The chapter concludes with a comparison between the proposed LeTID defect model and experiments in the literature.

Chapter 7 summarizes the results presented in this thesis.

Chapter 2

Properties of crystalline silicon

This chapter introduces the fabrication processes for silicon materials commonly used in the PV industry. Furthermore, fundamental quantities of semiconductor physics and recombination processes that limit the efficiency of silicon solar cells are introduced.

2.1 Silicon materials

Starting point for all silicon materials is silicon dioxide which is abundant in the earth's crust. In a first extraction step, metallurgical-grade silicon with a purity of more than 98 % is obtained via reduction of the raw material in an electric arc furnace [14]. Since this purity is not sufficient for photovoltaic applications, further purification steps are needed. The most widely used process for further purification is the Siemens process where the metallurgical-grade silicon is transferred into gaseous trichlorosilane [14]. High-purity polycrystalline silicon is then obtained by chemical vapor deposition (CVD) onto seed rods [15]. Polycrystalline silicon is the starting point for all subsequent crystallization techniques for both monocrystalline and multicrystalline silicon.

2.1.1 Multicrystalline silicon

Within this thesis, we investigate commercially available block-cast boron-doped multicrystalline silicon. Figure 2.1 shows a schematic of the casting setup for the production of multicrystalline silicon. High-purity polycrystalline silicon feedstock and the doping material is fed into a quartz crucible. The inner side of the crucible is coated with pre-annealed silicon nitride powder, preventing direct contact of the silicon melt with the crucible [16]. Directional solidification of the melt starts at the bottom of the crucible and

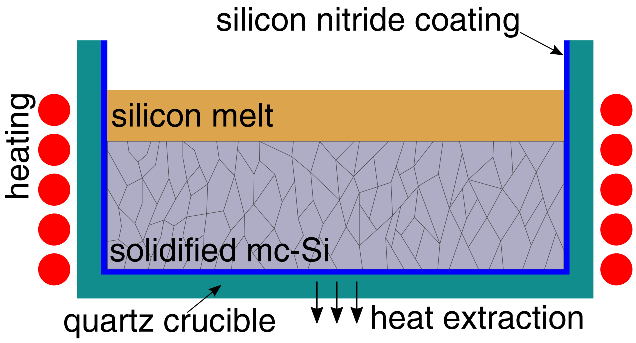

FIGURE 2.1: Schematic of a casting setup with directional solidification for the production of multicrystalline silicon.

progresses to the top [16]. After complete solidification, the ingot is detached from the crucible and sawn into (depending on the ingot size) multiple bricks, each with a base area of approximately 156 mm × 156 mm. However note that there are different industry standards for the actual wafer size with the industry moving towards larger wafers. The finished as-cut wafers are sawn from these bricks with a typical thickness of 180 µm.

The goal during directional solidification is a planar interface between the melt and the solidified part, ensuring a columnar growth of the mc-Si ingot. A characteristic feature of multicrystalline silicon material are columnar single crystals, with multiple sizes and crystal orientations of the grains. This leads to inhomogeneous material properties such as the grain size distribution.

Albeit the fabrication of multicrystalline silicon is easily-scalable and hence more suitable for low-cost silicon wafer production, impurities and crystallographic defects in the material are a drawback. At the high temperature of the molten silicon, metal contaminants diffuse from the crucible and the crucible's coating into the silicon. Because these contaminants, mostly metals, are often recombination-active, they limit the bulk carrier lifetime especially in the edge regions of the wafers. This zone of reduced carrier lifetime is often referred to as 'red zone' [17]. To increase the mc-Si material quality, there are efforts to minimize the impuritiy concentrations by using highly pure crucibles and coatings [18].

Another source of recombination are crystallographic defects such as dislocations. Since grain boundaries impede the propagation of dislocations during crystal growth, another way to improve mc-Si material is solidification into small grains. This high-performance (HP) mc-Si material is casted with a seed nucleation layer in the crucible,

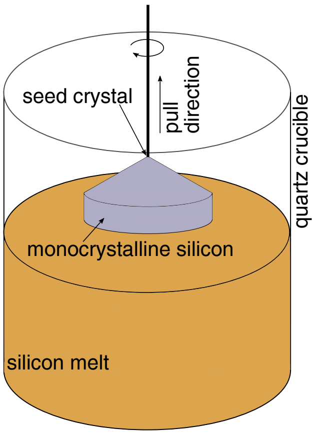

FIGURE 2.2: Schematic of the Czochralski growth process for the production of monocrystalline silicon.

inducing the growth of many small grains and thus reduced dislocation density [19, 20].

2.1.2 Czochralski-grown silicon

During the Czochralski growth process, a single crystal is grown from the liquid phase using a seed crystal in contact with the melt. By rotating and slowly pulling this seed crystal from the melt, a single crystal is formed. A schematic of the growth process is shown in Fig. 2.2. The result is a dislocation and impurity lean monocrystalline ingot, which is widely used within the microelectronic and PV industry. However, the Cz-grown silicon ingots feature very high oxygen concentrations stemming from the quartz crucible which are beneficial for the fabrication of integrated circuits but unfavorable for solar cells [21, 22]. On the one hand, the high oxygen concentration adds mechanical strength to the samples leading to reduced wafer breakage [23]. Furthermore, a high oxygen concentration is beneficial for metal-impurity gettering by using its ability to form oxygen precipitates and lattice defects [24]. On the other hand, boron-oxygen related recombination centres limit the conversion efficiency of Cz-Si solar cells [25, 26].

2.1.3 Float-zone silicon

In the float-zone process, the polysilicon rod is mounted vertically in an inert gas environment with admixtures of doping gases such as diborane for the growth of *p*-type silicon and phosphine for *n*-type silicon. As shown in Fig. 2.3, a heating coil moves along the height of the rod and melts a small segment of the silicon. Starting from a seed crystal

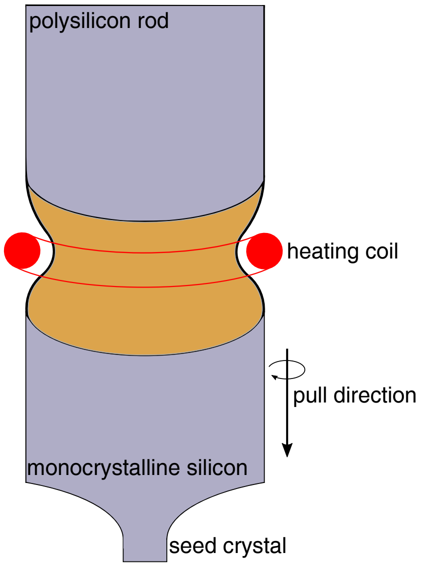

FIGURE 2.3: Schematic of the float-zone process for the production of monocrystalline silicon.

with given orientation, the melt crystallizes into monocrystalline silicon [27]. Since the molten silicon is in sole contact to the gas environment, there is no in-diffusion of impurities apart from the dopant atoms into the silicon. In addition to that, metal impurities are gettered into the liquid phase of the molten silicon, because of a larger solubility of metallic impurities in molten silicon. Thus, the top part of the crystal is discarded due to the accumulation of metallic impurities. The high-purity bulk of FZ-Si enables highest carrier lifetimes and serves as a reference e.g. for the investigation of surface passivation layers. Since the production of FZ-Si material is expensive and the maximum diameter of the processed ingots is limited, FZ-Si is used for highest efficiency research solar cells only.

2.2 Intrinsic semiconductors and doping

The electrical properties of semiconductors such as silicon are characterized by a forbidden energy gap between the valence band and the conduction band. Let E_V be the upper boundary of the valence band and E_C the lower boundary of the conduction band, then the width of the energy gap is $E_{\text{gap}} = E_C - E_V$. The total number of occupied states in both bands depends on both the Fermi-Dirac distribution $f(E)$ and on the densities of states D_V and D_C in the respective band. With

$$\begin{aligned} D_V(E) &= 4\pi(m_h^*/h^2)^{3/2} \cdot (E_V - E)^{1/2} \quad \text{and} \\ D_C(E) &= 4\pi(m_e^*/h^2)^{3/2} \cdot (E - E_C)^{1/2} \end{aligned} \tag{2.1}$$

being the densities of states, m_e^* being the effective mass of electrons, m_h^* the effective mass of holes and h the Planck constant. The electron and hole densities are given by:

$$n_0 = \int_{E_C}^{\infty} D_C(E)f(E)\mathrm{d}E \quad \text{and} \quad p_0 = \int_{-\infty}^{E_V} D_V(E)f(E)\mathrm{d}E, \tag{2.2}$$

with n_0 the electron density and p_0 the hole density. In most cases, the conditions $(E_C - E_F) \gg k_BT$ and $(E_F - E_V) \gg k_BT$ are satisfied with E_F being the Fermi energy, k_B the Boltzmann constant and T the absolute temperature. Therefore, the Fermi-Dirac distribution can be approximated by the Boltzmann distribution $f_B(E) = \exp\big(-(E - E_F)/(k_BT)\big)$ which simplifies the integration of Eqn. 2.2. Thus, the total densities of electrons and holes in the respective bands are:

$$\begin{aligned} n_0 &= \underbrace{2\left(\frac{2\pi m_e^* k_BT}{h^2}\right)^{3/2}}_{=N_C} \exp\left(\frac{E_F - E_C}{k_BT}\right) = N_C \exp\left(\frac{E_F - E_C}{k_BT}\right) \quad \text{and} \\ p_0 &= \underbrace{2\left(\frac{2\pi m_h^* k_BT}{h^2}\right)^{3/2}}_{=N_V} \exp\left(\frac{E_V - E_F}{k_BT}\right) = N_V \exp\left(\frac{E_V - E_F}{k_BT}\right) \end{aligned} \tag{2.3}$$

with N_V and N_C being the effective densities of states for the valence band and the conduction band, respectively. A fundamental quantity of a semiconductor is the intrinsic carrier density n_i, which is connected to n_0 and p_0 by the mass action law:

$$n_i^2 = n_0 \cdot p_0 = N_C N_V \exp\left(-\frac{E_{\text{gap}}}{k_BT}\right). \tag{2.4}$$

In an ideal intrinsic semiconductor, the condition $n_i = n_0 = p_0$ is satisfied. Using this relationship, the value of the intrinsic Fermi energy E_i can be calculated from Eqn. 2.3:

$$\begin{aligned} & n_0 = p_0 \\ \Rightarrow\ & N_C \exp\left(\frac{E_F - E_C}{k_B T}\right) = N_V \exp\left(\frac{E_V - E_F}{k_B T}\right) \\ \Leftrightarrow\ & E_F = \frac{E_C - E_V}{2} + \frac{k_B T}{2} \ln\left(\frac{N_V}{N_C}\right) \equiv E_i. \end{aligned} \tag{2.5}$$

In order to apply semiconductors such as silicon for technological applications, dopants are introduced into the material which intendedly increase the number of electrons or holes. Dopants are separated into two groups: donors and acceptors. Elements from the fifth group of the periodic table of the elements (such as phosphorus, arsenic and antimony) have five valence electrons and are used to increase the number of electrons in silicon. On the other hand, elements from the third group (such as boron, gallium and indium) are used to increase the number of holes in silicon. Hence, the balance between n_0 and p_0 is disturbed and a new equilibrium adjusts with one carrier species being majorities and the other species being minorities. If the electrons are majority carriers the material is called n-type and if holes are the majority carriers the material is called p-type.

2.3 Recombination and carrier lifetime

Exciting electron-hole pairs in a semiconductor results in excess charge carriers. Under the reasonable assumption of charge neutrality, the excess carrier concentrations Δn for electrons and Δp for holes are equal. Thus, the total concentrations of charge carriers now reads:

$$\begin{aligned} n &= n_0 + \Delta n = n_0 + \Delta p \quad \text{for electrons} \quad \text{and} \\ p &= p_0 + \Delta p = p_0 + \Delta n \quad \text{for holes.} \end{aligned} \tag{2.6}$$

The excitation of excess carriers can e.g. be accomplished by illuminating the sample with light of sufficiently high photon energies ($h\nu > E_g$). However, due to recombination processes a steady-state condition is established, where the total generation rate G_{total}

of excess carriers equals the total recombination rate U_{total}. Note that the total generation rate is composed of the thermal generation rate G_{thermal} and the generation rate due to the illumination $G_{\text{illumination}}$. Upon switching off the illumination, the initial state is restored with an effective recombination rate $U_{\text{eff}} = U_{\text{total}} - G_{\text{thermal}}$, since the thermal generation is also taking place in the dark. Thus, the decay of excess carriers Δn is described by a first-order differential equation:

$$\frac{\partial \Delta n(t)}{\partial t} = -U_{\text{eff}}(\Delta n). \tag{2.7}$$

Under the simplified assumption that $U_{\text{eff}}(\Delta n)$ is proportional to Δn, the solution of Eqn. 2.7 is a mono-exponential decay with the time constant τ independent of Δn. This time constant is defined as the carrier lifetime. Thus, the definition of the carrier lifetime can be written as:

$$\tau \equiv \frac{\Delta n}{U_{\text{eff}}}. \tag{2.8}$$

Note that the recombination rate U_{eff} frequently shows a superlinear dependence on Δn, making the carrier lifetime depend on the excess carrier density Δn.

2.3.1 Radiative recombination

The radiative band-to-band recombination describes the direct recombination of an electron from the conduction band with a hole from the valence band. The energy difference between the electron and the hole is emitted as a photon of corresponding energy. Therefore, the process can be considered as the inverse process of the photogeneration. Since in each radiative recombination event exactly one electron and one hole is involved, the recombination rate depends on both the concentration of electrons in the conduction band n and the concentration of holes in the valence band p. Thus, the total radiative recombination rate $U_{\text{rad.total}}$ is given by [28]:

$$U_{\text{rad.total}} = B \cdot n \cdot p, \tag{2.9}$$

with B being the coefficient of radiative recombination. Subtracting the radiative recombination rate in the equilibrium state from the total radiative recombination rate yields the effective radiative recombition rate:

$$U_{\mathrm{rad.eff}} = B\left(np - n_i^2\right). \tag{2.10}$$

Due to screening effects, the proportionality factor $B(\Delta n, p_0, n_0)$ is dependent on the excess carrier density Δn and the base doping density p_0 for *p*-type silicon and n_0 for *n*-type silicon [29].

2.3.2 Auger recombination

In contrast to the process of radiative recombination described above, for Auger recombination the energy released upon recombination of an electron with a hole is not emitted in the form of a photon with corresponding energy. It is rather transferred to a third particle being an electron in an electron-electron-hole event (eeh-event) or a hole in an electron-hole-hole event (ehh-event). Under the assumption of non-interacting quasi-free particles [30–32], the Auger recombination rate depends on the concentrations of each particle involved:

$$U_{\mathrm{Auger.total}} = C_{\mathrm{eeh}} n^2 p + C_{\mathrm{ehh}} n p^2 \tag{2.11}$$

with C_{eeh} and C_{ehh} being the corresponding Auger coefficients [33]. Substracting the Auger recombination in the equilibrium state yields the effective Auger recombination rate:

$$U_{\mathrm{Auger.eff}} = C_{\mathrm{eeh}}\left(n^2 p - n_i^2 n_0\right) + C_{\mathrm{ehh}}\left(np^2 - n_i^2 p_0\right). \tag{2.12}$$

The Auger coefficients ideally do not depend on neither the doping density of the silicon nor on the excess carrier density. However, there are deviations from this ideal case including effects due to phonon and Coulomb interaction [34, 35]. Especially at low excess carrier densities, the Auger recombination is Coulomb-enhanced. This is accounted for by the enhancement factors g_{eeh} and g_{ehh}. The resulting Auger coefficients C^*_{eeh} and C^*_{ehh} which include the enhancement factors are:

$$C^*_{\mathrm{eeh}} = g_{\mathrm{eeh}} \cdot C_{\mathrm{eeh}} \qquad \text{and} \qquad C^*_{\mathrm{ehh}} = g_{\mathrm{ehh}} \cdot C_{\mathrm{ehh}}. \tag{2.13}$$

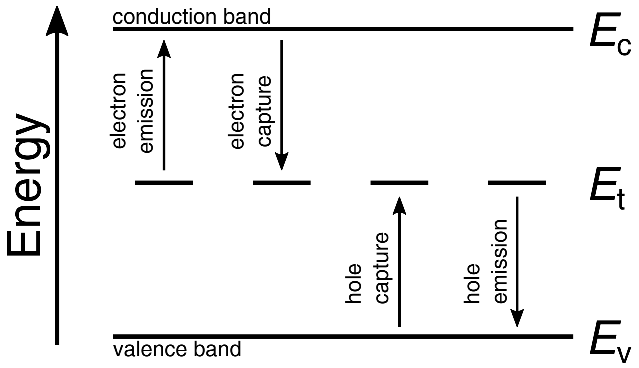

FIGURE 2.4: Band diagram with a single monovalent energy state E_t within the band gap. The diagram shows four possible interactions of electrons or holes with the energy state at E_t: (i) electron emission into the conduction band, (ii) electron capture from the conduction band, (iii) hole capture from the valence band and (iv) hole emission into the valence band.

The enhancement factors depend on both the doping density of the silicon and the excess carrier density [34–36].

2.3.3 Intrinsic lifetime

Both the radiative recombination as well as the Auger recombination occur intrinsically in crystalline silicon, thus they sum up to the intrinsic effective recombination rate $U_{\mathrm{intr.eff}}$. According to equation 2.8, the intrinsic carrier lifetime τ_{intr} is:

$$\tau_{\mathrm{intr}} = \frac{\Delta n}{U_{\mathrm{rad.eff}} + U_{\mathrm{Auger.eff}}}, \tag{2.14}$$

and thus:

$$\frac{1}{\tau_{\mathrm{intr}}} = \frac{1}{\tau_{\mathrm{rad}}} + \frac{1}{\tau_{\mathrm{Auger}}}, \tag{2.15}$$

with τ_{rad} being the lifetime limited by radiative recombination and τ_{Auger} the lifetime limited by Auger recombination.

2.3.4 Extrinsic lifetime

Shockley-Read-Hall recombination statistics

In addition to the intrinsic recombination, there is extrinsic recombination due crystallographic defects, impuritites in the bulk and surface states. In the most simple case, the recombination involves a single monovalent state within the silicon band gap. In this case, the recombination can be described using the recombination statistics of Shockley, Read and Hall (SRH-statistics) [37, 38]. In the following, the derivation of the SRH statistics is outlined based on the interactions of electrons or holes with an energy state within the band gap as shown in Fig. 2.4 and following a description from Schlachetzki [39].

If there is a defect state with an energy level E_t in the semiconductor band gap, then electrons and holes may interact with the defect through the processes shown in Fig. 2.4. Let N_t be the density of the defect and f_t the probability that the defect is occupied by an electron. Then, the electron emission rate $R_{\text{electron.e}}$ is proportional to both N_t and f_t: $R_{\text{electron.e}} \propto N_t f_t$. Using the same approach, the electron capture rate $R_{\text{electron.c}}$ is proportional to $N_t(1 - f_t)$ and to the density of electrons in the conduction band: $R_{\text{electron.c}} \propto N_t(1 - f_t)n$. Thus, the net capture rate for electrons is:

$$R_{\text{electron.c.net}} = R_{\text{eletron.c}} - R_{\text{electron.e}} = c_n N_t(1 - f_t)n - e_n N_t f_t \tag{2.16}$$

with c_n and e_n being proportionality constants for the electron capture and emission, respectively. Analogously, the net capture rate for holes $R_{\text{hole.c.net}}$ is derived from the hole capture $R_{\text{hole.c}}$ and emission rates $R_{\text{hole.e}}$:

$$R_{\text{hole.c.net}} = R_{\text{hole.c}} - R_{\text{hole.e}} = c_h N_t f_t p - e_h N_t(1 - f_t) \tag{2.17}$$

with c_h and e_h being proportionality constants for the hole capture and emission, respectively.

In equilibrium, the respective capture and emission rates are equal and thus the net rates for electrons and holes vanish. Using Eqns. 2.16 and 2.17, this yields the following expressions for the emission coefficients for electrons e_n and holes e_h:

$$\begin{aligned} e_n &= c_n n \left(\frac{1 - f_t}{f_t}\right) \quad \text{and} \\ e_h &= c_h p \left(\frac{f_t}{1 - f_t}\right). \end{aligned} \tag{2.18}$$

Using the electron and hole densities in equilibrium given by Eqn. 2.3 and further using the Fermi-Dirac distribution $f_t = f(E_t)$ for the occupation probability of the defect, the emission coefficients can be written as follows, introducing the so-called SRH densities n_1 and p_1:

$$\begin{aligned} e_n &= c_n N_C \exp\left(-\frac{E_C - E_t}{k_B T}\right) = c_n n_1 \quad \text{and} \\ e_h &= c_h N_V \exp\left(-\frac{E_t - E_V}{k_B T}\right) = c_h p_1. \end{aligned} \tag{2.19}$$

In the case that the Fermi level coincidences with the energy level of the defect (i.e. $E_t = E_F$), the densities n_1 and p_1 describe the charge carrier concentrations in the conduction band and in the valence band, respectively.

The injection of excess charge carriers will cause a disturbance of the equilibrium situation, however, after a certain time interval, a steady-state condition will readjust. Within this steady-state condition, the number of electrons and holes interacting with the defect have to be equal, thus that $R_{\text{electron.c.net}} = R_{\text{hole.c.net}}$. Using Eqns. 2.16 and 2.17 and inserting Eqn. 2.19 yields an expression for the occupation probability f_t in dependence of the defect parameters n_1, p_1, c_n and c_p as well as of the electron and hole concentrations n and p [40]:

$$f_t = \frac{e_n n + e_p p_1}{e_p p + e_p p_1 + e_n n + e_n n_1}. \tag{2.20}$$

Using that $R_{\text{electron.c.net}} = R_{\text{hole.c.net}}$, the net recombination rate for electrons and holes is:

$$R_{\text{electron.c.net}} = R_{\text{hole.c.net}} = \frac{np - n_1 p_1}{\tau_{n0}(p + p_1) + \tau_{p0}(n + n_1)} \tag{2.21}$$

with $\tau_{n0} = (N_t c_n)^{-1}$ and $\tau_{p0} = (N_t c_p)^{-1}$ being the capture time constants. The proportionality constants c_n and c_p for the electron and hole capture processes can be identified with the product of the capture cross-sections σ_n (for electrons) and σ_p (for holes) with the thermal velocity ν_{th} [40]. Using $n_1 p_1 = n_i^2$, we obtain the effective SRH recombination rate $U_{\text{SRH.eff}}$:

$$U_{\text{SRH.eff}} = \frac{\left(np - n_i^2\right) \nu_{\text{th}} N_{\text{t}}}{\sigma_{\text{p}}^{-1}\left(n + n_1\right) + \sigma_{\text{n}}^{-1}\left(p + p_1\right)}. \tag{2.22}$$

Using equation 2.8, the SRH effective recombination rate can be expressed in terms of the corresponding SRH lifetime τ_{SRH}:

$$\tau_{\mathrm{SRH}} = \frac{\tau_{\mathrm{p0}}\,(n_0 + n_1 + \Delta n) + \tau_{\mathrm{n0}}\,(p_0 + p_1 + \Delta n)}{p_0 + n_0 + \Delta n}. \tag{2.23}$$

Both the energy level E_t and the ratio of the capture time constants $Q = \tau_{\mathrm{p0}}/\tau_{\mathrm{n0}} = \sigma_{\mathrm{n}}/\sigma_{\mathrm{p}}$ are characteristics for a certain defect and can be extracted from injection-dependent measurements of the SRH lifetime.

Voronkov et al. [41] and Murphy et al. [42] suggested a different notation of the SRH lifetime which yields an easy way of extracting the Q value from the SRH lifetime. Let X be the ratio of minority carrier to majority carrier densities $X = n/p$, then the SRH lifetime in p-type material is given by [42]:

$$\tau_{\mathrm{SRH}} = \frac{1}{\sigma_n \nu_{\mathrm{th}} N_t}\left(1 + \frac{Qn_1}{p_0} + \frac{p_1}{p_0} + X\left(Q - \frac{Qn_1}{p_0} - \frac{p_1}{p_0}\right)\right). \tag{2.24}$$

If the SRH lifetime is plotted as a function of X, the plot becomes linear with the slope $\mathrm{d}\tau_{\mathrm{SRH}}/\mathrm{d}X$ and the axis intercept $\tau_{\mathrm{SRH}.X\to 0}$. The ratio of the slope divided by the axis intercept yields:

$$\frac{\mathrm{d}\tau_{\mathrm{SRH}}/\mathrm{d}X}{\tau_{\mathrm{SRH}.X\to 0}} = \frac{Q - \frac{Qn_1}{p_0} - \frac{p_1}{p_0}}{1 + \frac{Qn_1}{p_0} + \frac{p_1}{p_0}} = \frac{Q - \xi}{1 + \xi} \tag{2.25}$$

with $\xi = \frac{Qn_1}{p_0} + \frac{p_1}{p_0}$. Under the assumption that the defect has an energy level close to the middle of the band gap and for typical doping densities of p-type silicon material (i.e. $p_0 > 1 \times 10^{13}\,\mathrm{cm}^{-3}$), ξ becomes negligibly small. Thus, the result of equation 2.25 equals Q. Figure 2.5 shows (a) the SRH lifetime for three different single-level defects plotted versus the excess carrier density and (b) plotted versus the carrier density ratio n/p. For both defects with an energy level of $E_c - E_t = 0.56\,\mathrm{eV}$, the value of Q can be calculated according to Eqn. 2.25. However, for the third defect with an energy level of $E_c - E_t = 0.2\,\mathrm{eV}$, the condition $\xi \to 0$ is not fulfilled. Note that despite $\xi \to 0$ is not fulfilled, the SRH lifetime is nevertheless a linear function of the carrier density.

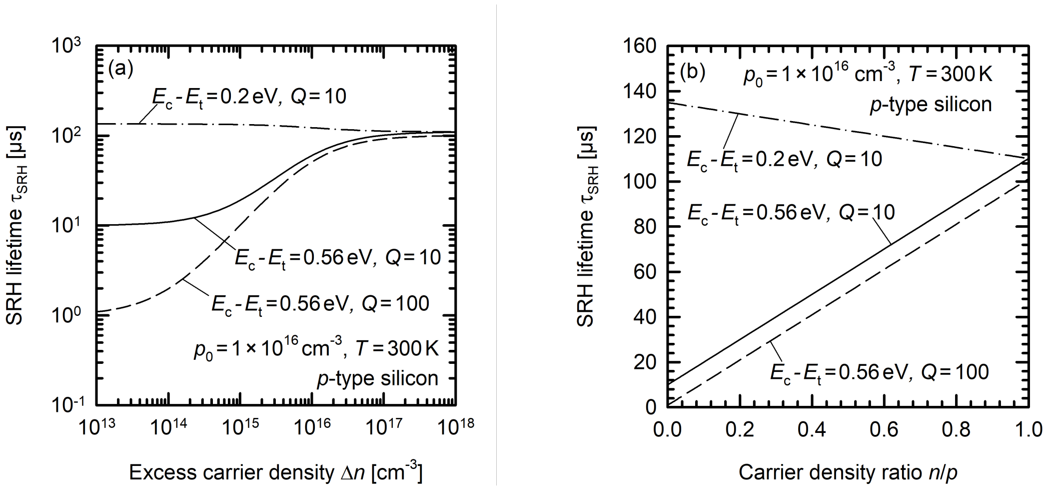

FIGURE 2.5: (a) SRH lifetime for three different single-level defects plotted versus the excess carrier density. (b) SRH lifetime for the same single-level defects as shown in (a) plotted versus the ratio of minority to majority carrier densities.

Surface recombination

Because the samples have finite dimensions, there is an impact related to the recombination at the sample's surfaces U_{surface}. This effect is due to surface states which lie within the band gap and hence cause a locally increased recombination. The surface recombination rate U_{surface} for surface states with a state density $D_{\text{it}}(E)$ can be written analogously to the Shockley-Read-Hall recombination statistics:

$$U_{\text{surface}} = \int_{E_V}^{E_C} \frac{\left(n_s p_s - n_i^2\right) \nu_{\text{th}} D_{\text{it}}(E)}{\sigma_{\text{p}}^{-1}(E)(n_s + n_1(E)) + \sigma_{\text{n}}^{-1}(E)(p_s + p_1(E))} \mathrm{d}E \tag{2.26}$$

with n_s and p_s being the electron and hole concentrations at the silicon surface [43]. The surface state density $D_{\text{it}}(E)$ is used, because the surface states are quasi-continuously distributed in the band gap. The surface recombination rate U_{surface} describes the recombination per unit area of the silicon surface, thus the recombination depends on the number of electrons and holes reaching the surface. Therefore, the surface recombination rate U_{surface} is usually translated into a surface recombination velocity S:

$$S \equiv \frac{U_{\text{surface}}}{\Delta n_s}, \quad \text{(no band bending)} \tag{2.27}$$

which accounts for the excess carrier concentration at the silicon surface Δn_s. If there is a band bending present at the silicon surface, typically the excess carrier concentration at the edge of the space charge region Δn_d is used and the effective recombination velocity S_{eff} is defined as:

$$S_{\text{eff}} = \frac{U_{\text{surface}}}{\Delta n_d}. \tag{2.28}$$

Since the high surface recombination velocity of a bare silicon surface limits the effective carrier lifetime, measurements of the bulk lifetime are difficult. Therefore, passivation layers such as aluminium oxide and silicon nitride which lower the surface recombination are deposited onto the silicon surfaces [44]. For sufficiently small values of the surface recombination velocities, the effective carrier lifetime τ_{eff} is a function of the bulk carrier lifetime τ_{b}, the surface recombination velocity S_{eff} and the wafer thickness W [45]:

$$\frac{1}{\tau_{\text{eff}}} = \frac{1}{\tau_{\text{b}}} + \frac{1}{\tau_{\text{surface}}} = \frac{1}{\tau_{\text{b}}} + \frac{2S_{\text{eff}}}{W}. \tag{2.29}$$

Note that this only holds true for an equal surface recombination velocity S_{eff} on the front and rear side of the wafer. Sproul [45] showed that Eqn. 2.29 is valid within 4 % if $SW/D < 0.25$ is satisfied, with D being the diffusion coefficient of the excess carriers. Under low injection conditions the value of D equals the diffusion coefficient of minority carriers, however under high injection conditions D is the ambipolar diffusion coefficient [45].

2.3.5 Effective carrier lifetime

The actually measured effective carrier lifetime τ_{eff} consists of the individual lifetimes of the respective recombination channels. The recombination rate corresponding to the effective carrier lifetime is the sum of the respective recombination rates:

$$\begin{aligned} U_{\text{eff}} &= U_{\text{intr.eff}} + U_{\text{extr.eff}} + U_{\text{surface}} \\ \Rightarrow \quad \tau_{\text{eff}}^{-1} &= \underbrace{\frac{1}{\tau_{\text{rad}}} + \frac{1}{\tau_{\text{Auger}}} + \frac{1}{\tau_{\text{SRH}}}}_{=1/\tau_{\text{b}}} + \frac{1}{\tau_{\text{surface}}}, \end{aligned} \tag{2.30}$$

with τ_{b} being the bulk lifetime. Figure 2.6 shows the calculated intrinsic lifetime for 1.2 Ω cm p-type silicon, an assumed SRH defect ($E_t - E_V = 0.56$ eV and $Q = 10$) and the resulting bulk lifetime.

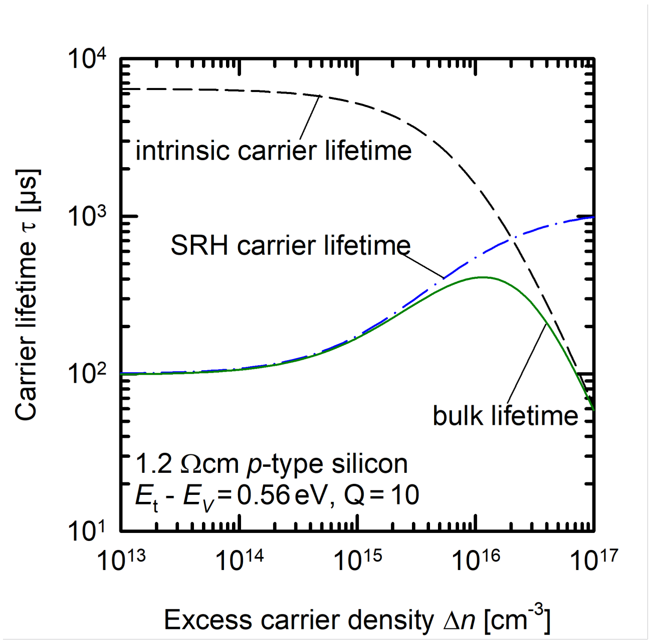

FIGURE 2.6: Intrinsic carrier lifetime, SRH carrier lifetime and the resulting effective carrier lifetime plotted versus the excess carrier density for 1.2 Ω cm *p*-type silicon. A single monovalent SRH defect with $E_t - E_V = 0.56$ eV and $Q = 10$ is assumed.

2.3.6 Effective defect density

To study the evolution of recombination-active defects in crystalline silicon, the effective defect density N^* can be calculated from the measured effective carrier lifetime. Under the assumption that all recombination channels except the recombination channel associated with the defect under investigation are constant, the inverse of the initial carrier lifetime $\tau_{\text{eff}}(0)$ is substracted from the inverse of the carrier lifetime $\tau_{\text{eff}}(t)$ at a time t, measured e.g. during a degradation process. This yields the time-dependent effective defect density:

$$N^*(t) = \frac{1}{\tau_{\text{eff}}(t)} - \frac{1}{\tau_{\text{eff}}(0)}. \qquad (2.31)$$

Thus, all contributions from constant recombination channels cancel out. Under the assumption that other recombination-active defects and the surface recombination remain constant, the effective defect density is proportional to the actual concentration of the recombination-active defect in the sample.

Chapter 3

Characterization techniques

In this chapter, the characterization techniques applied in this thesis are presented. At first, the integral and spatially resolved techniques for the measurement of the carrier lifetime are introduced. After that, the applied thin film characterization techniques are described, including measurements of film thickness, refractive index, mass and atomic density as well as the hydrogen content of the respective films.

3.1 Carrier lifetime measurements

The measurements of the carrier lifetime throughout this thesis are based on measuring the time dependent photoconductance of the silicon sample. The measurement techniques are subdivided into integral measurements that average the carrier lifetime over the sensor area and camera-based spatially resolved measurements.

3.1.1 Integral lifetime measurements

The silicon sample under investigation is excited by flash-light illumination and the evolution of the photoconductance is measured using the eddy-current method (WCT-120, Sinton Instruments). This method uses an oscillating circuit and the sample is placed on top of a coil (cf. Fig. 3.1) [46]. The high-frequency magnetic field produced by the coil induces eddy currents in the silicon sample, which in turn create a magnetic field opposed to the magnetic field of the coil. Since the strength of the opposed magnetic field depends on the conductance of the sample, measuring the impedance of the coil enables contactless and time-resolved determination of the sample's conductance. During flash light illumination, the sample's conductivity σ changes due to the change in excess

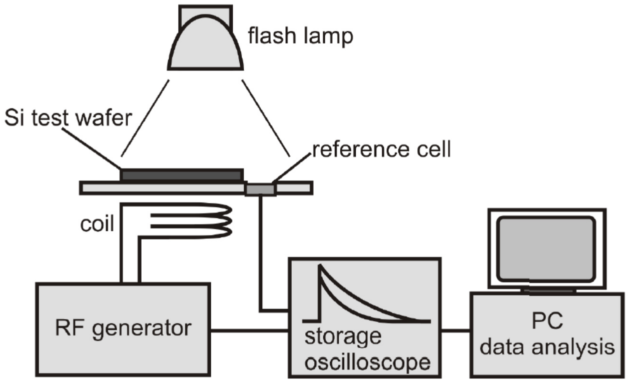

FIGURE 3.1: Schematic of the experimental setup of the WCT-120 from Sinton Instruments for the integral measurement of the carrier lifetime. Schematic taken from [46].

carrier concentration Δn:

$$\sigma = \sigma_0 + \Delta\sigma = \frac{q_e}{W}\int_0^W (n_0\mu_n + p_0\mu_p)\mathrm{d}x + \frac{q_e}{W}\int_0^W (\Delta n\mu_n + \Delta p\mu_p)\mathrm{d}x, \tag{3.1}$$

with σ_0 being the sample's conductance in the dark, $\Delta\sigma$ the photoconductivity, q_e the elementary charge, W the sample thickness, μ_n and μ_p the mobilities for electrons and holes, respectively. For a homogeneous excitation, i.e. assuming that Δn is constant over the thickness of the silicon wafer, Eqn. 3.1 simplifies to:

$$\sigma = \sigma_0 + \underbrace{q_e\Delta n\left(\mu_n + \mu_p\right)}_{\text{photoconductivity } \Delta\sigma}. \tag{3.2}$$

Note that the carrier mobilities μ_n and μ_p themselves depend on the excess carrier densities, thus extracting the excess carrier density from photoconductance measurements requires a self-consistent solution of Eqn. 3.2. The value for the sum of both mobilities can be obtained from a semi-empirical expression given in reference [47].

The evolution of the excess carrier concentration Δn is linked with both the generation and recombination of carriers through the continuity equation:

$$\frac{\partial\Delta n(\vec{x},t)}{\partial t} = G(\vec{x},t) - U(\vec{x},t) + \frac{1}{q_e}\nabla\vec{J}(\vec{x},t), \tag{3.3}$$

with $\vec{J}$ being the current density. Since there are no compensating currents in the case of homogeneous generation and recombination, we assume $\nabla\cdot\vec{J} = 0$ and that the dependence on the coordinate $\vec{x}$ vanishes. Using the definition of the carrier lifetime in

Eqn. 2.8 yields [48]:

$$\tau_{\text{eff}} = \frac{\Delta n(t)}{G(t) - \frac{\partial \Delta n(t)}{\partial t}}. \tag{3.4}$$

This so-called generalized data analysis is valid for any time dependence of the flash excitation and thus of the generation rate. Equation 3.4 has two limiting cases. If the decay time constant of the flash excitation is much larger than the carrier lifetime, the sample is under quasi-steady-state conditions (QSS) with $\tau_{\text{eff}} = \frac{\Delta n}{G}$, where the generation and recombination rates are equal at each point in time. However, if the decay time constant is much shorter than the flash excitation, the photoconductance decay (PCD) is analyzed after the flash terminates, such that $G = 0$ is assumed. In this case, Eqn. 3.4 simplifies to:

$$\tau_{\text{eff}} = -\frac{\Delta n(t)}{\frac{\partial \Delta n(t)}{\partial t}}. \tag{3.5}$$

Most of the lifetime measurements in this thesis are performed using the WCT-120 lifetime tester from Sinton Instruments which corresponds to the schematic shown in Fig. 3.1. This measurement setup is equipped with a 10.7 MHz radio frequency (rf) oscillating circuit for the eddy current measurements. The diameter of the coil is 18 mm and thus the measured lifetime values are averaged over a circular area of approximately 250 mm^2. The flash excitation can be varied between a flash with long decay time constant ($\approx$ 2.1 ms) for QSS measurements and a flash with short time constant ($\approx$ 30 µs) for PCD measurements. To achieve a homogeneous excitation over the sample thickness, a long-pass filter with a cut-off wavelength of 700 nm is installed in front of the flash light. The time dependence of the flash excitation is measured using a calibrated silicon reference solar cell and converted into the generation rate by applying an optical factor which accounts for the different optical properties between reference cell and silicon sample. Furthermore, the output voltage of the rf measurement setup is recorded and calibrated using a set of silicon wafers with known conductances. The excess carrier density Δn is calculated from the self-consistent solution of Eqn. 3.2 and the carrier lifetime is calculated by using the QSS, PCD or generalized data analysis approach. Within this study, if not stated otherwise, the measured lifetime values are reported at a constant

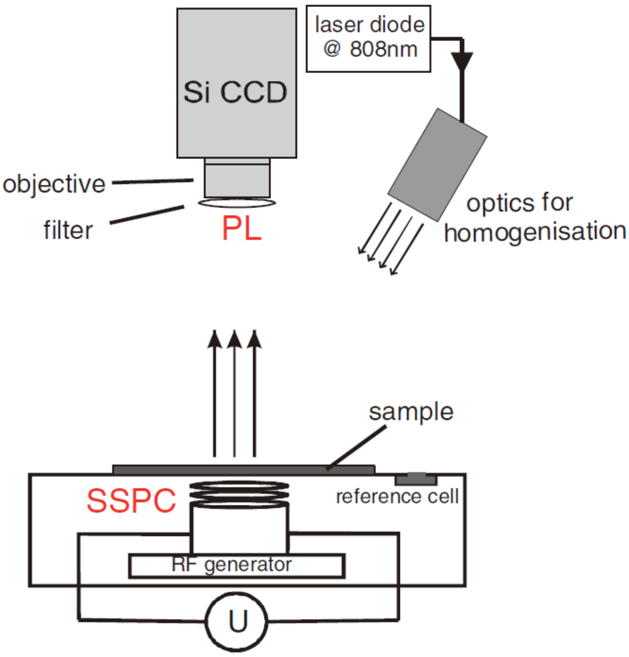

FIGURE 3.2: Schematic of the experimental setup for the spatially resolved measurement of the carrier lifetime. Schematic taken from [49].

excess carrier density of $\Delta n = 1 \times 10^{15}\,\mathrm{cm}^{-3}$.

3.1.2 Spatially resolved lifetime measurements

Photoconductance-calibrated photoluminescence (PL) imaging is used for spatially resolved measurements of the carrier lifetime [49]. The silicon sample under test is homogenously excited by an 808 nm laser, as depicted in Fig. 3.2. According to Eqn. 2.9 the radiative recombination rate is proportional to the product of the electron and the hole concentrations. As a consequence, the PL intensity I_{PL} measured with a charge-coupled device (CCD) camera [49] is given by:

$$I_{\mathrm{PL}} \propto U_{\mathrm{rad.total}} \approx B\Delta n(\Delta n + N_A)\,, \tag{3.6}$$

for p-type silicon with I_{PL} being the PL signal intensity and N_A the acceptor concentration. Thus, the PL signal shows a quadratic dependence on the excess carrier concentration Δn in the sample. The actual excess carrier concentration Δn is measured using the photoconductance-based method described in subsection 3.1.1. The PL signal intensity I_{PL} is calibrated to the excess carrier density Δn under steady-state conditions by using different illumination intensities and hence different excess carrier concentrations. By

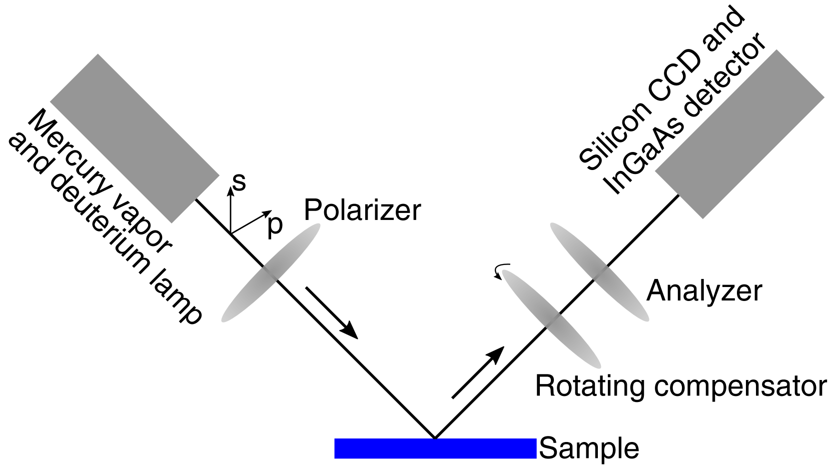

FIGURE 3.3: Schematic of the setup used for ellipsometry measurements in this thesis.

applying this calibration procedure, as described in detail by Herlufsen et al. [49], the spatially resolved measurement of the PL signal $I_{\mathrm{PL}}(x,y)$ is converted into a spatially resolved map of the excess carrier concentration $\Delta n(x,y)$. Under steady-state conditions, the excess carrier concentration is directly linked to the carrier lifetime τ_{eff} and the generation rate G via $\tau_{\mathrm{eff}} = \Delta n/G$. The generation rate G is calculated from the photon flux of the illumination Φ, which is measured using a calibrated silicon reference cell:

$$G = \Phi\,(1 - R_{808})\,\frac{1}{W}, \tag{3.7}$$

with R_{808} being the reflectivity at a wavelength of 808 nm and W the thickness of the wafer under test [49]. Dividing the spatially resolved excess carrier concentration $\Delta n(x,y)$ by the generation rate G thus yields the spatially resolved carrier lifetime $\tau_{\mathrm{eff}}(x,y)$.

3.2 Thin film characterization techniques

3.2.1 Ellipsometry

In this thesis, the optical properties of silicon nitride layers are characterized by spectrally resolved ellipsometry. Ellipsometry is an optical characterization technique which measures the ratio of amplitudes tan (Ψ) between s- and p-polarized light as well as the phase difference Δ upon light reflection (or transmission) at the sample [50]. The spectrally resolved ellipsometry tool applied in this thesis (M-2000UI, J.A. Woollam) measures pairs of (Ψ,Δ) each 1.6 nm in the wavelength range from 250 to 970 nm and each 6.1 nm

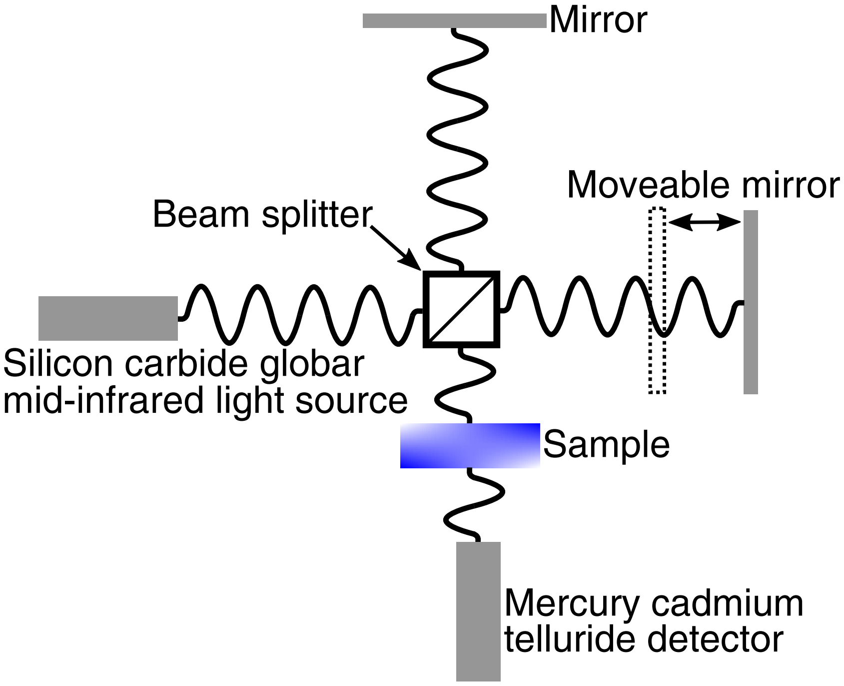

FIGURE 3.4: Schematic of the basic working principle of FTIR measurements.

in the wavelength range from 970 to 1690 nm after light reflection at multiple angles in the range from 60° to 80° at the sample. The schematic of the experimental setup used in this thesis is shown in Fig. 3.3. For the evaluation of the measurement data the *WVASE32* software (J. A. Woollam) from the manufacturer of the ellipsometer is used. Within this software a model of the sample's structure is generated and optical properties are taken from literature data [51]. The software then performs a fit of the measurement data, fitting the thickness of the thin film, the wavelength-dependent refractive index n and the wavelength-dependent extinction coefficient k.

3.2.2 Fourier Transform Infrared Spectroscopy (FTIR)

In this thesis, fourier transform infrared spectroscopy (FTIR) is used for measurements of concentrations of different atomic bonds within the silicon nitride films. These bonds are detected by their characteristic absorption peaks in the mid-infrared regime (2500 nm to 25 000 nm). The schematic of the basic working principle of FTIR measurements is shown in Fig. 3.4. FTIR measurements in this thesis are performed with a *VERTEX 70* (Bruker) FTIR spectrometer. The light source is a silicon carbide globar which emits light in the mid-wavelength infrared regime. A beam splitter divides the light beam onto two paths: one with a stationary mirror and the other one with a moveable mirror. Both beams

TABLE 3.1: Silicon nitride absorption peak locations and calibration constants taken from [53], as used within this thesis.

Wave number ν [cm^{-1}]	Calibration factor K [cm^{-1}]
Si-N related modes	
880	2.1×10^{16}
1030	2.1×10^{16}
Si-H related mode	
2180	5.9×10^{16}
N-H related mode	
3320	8.2×10^{16}

interfere with each other after reflection at the respective mirror and the resulting beam passes the sample. Finally, a mercury cadmium telluride (MCD) detector measures the intensity of the resulting beam. Because of the moving mirror, the measured intensity shows a dependence on the displacement of the mirror. The resulting interferogram is a sum of the interferograms at each wavelength. Applying a fourier transformation and comparing the spectrum with a reference measurement without sample in the beam allows for the calculation of the sample's transmission for each wavelength in the spectrum of the light source.

By determining the concentration of hydrogen-containing bonds, the total hydrogen concentration [H] within the films is calculated. The hydrogen fraction H in the silicon nitride films is defined as [52]:

$$H = \frac{[\mathrm{Si-H}] + [\mathrm{N-H}]}{[\mathrm{Si-H}] + [\mathrm{N-H}] + [\mathrm{Si-N}]} = \frac{[\mathrm{H}]}{[\mathrm{H}] + [\mathrm{Si-N}]}, \tag{3.8}$$

neglecting silicon-silicon ([Si − Si]), nitrogen-nitrogen ([N − N]) as well as hydrogen-hydrogen bonds ([H − H]). Because of these assumptions, which hold true for nearly stochiometric films but add additional uncertainty for silicon-rich films, the results of the FTIR measurements are compared with results from nuclear reaction analysis (NRA) described in the next subsection. As shown in Fig. 3.5(a), it is found that the hydrogen concentrations measured using FTIR are well validated by the NRA measurements. Evaluation of the absorption spectra include background correction, baseline fitting, deconvolution of the absorption peaks and calculation of the areas under the absorption peaks listed in Table 3.1. Figure 3.5(b) shows an exemplary FTIR measurement of a FZ-Si sample coated with silicon nitride on both surfaces. The absorption coefficient α

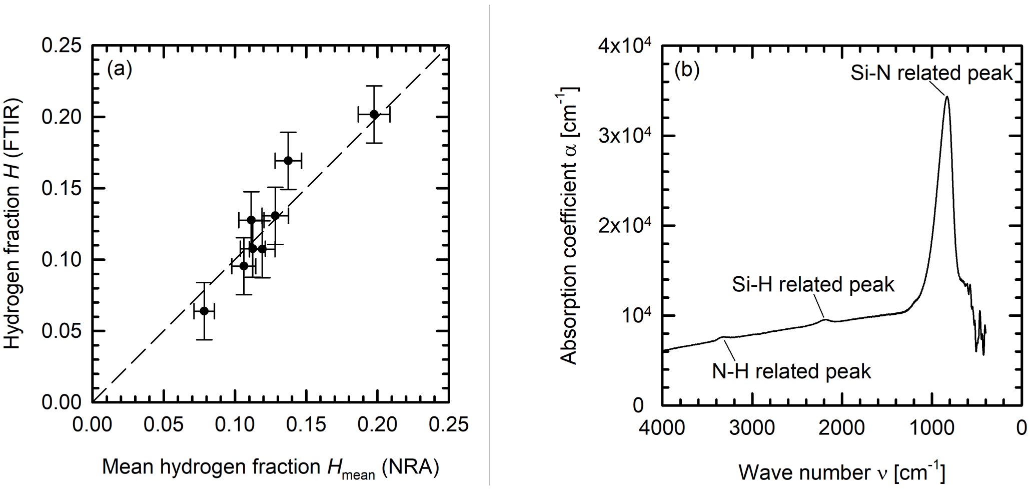

FIGURE 3.5: (a) Hydrogen fraction H measured using FTIR plotted versus the mean hydrogen fraction in the same films measured using nuclear reaction analysis (NRA). The results from FTIR measurements are well validated by the NRA results. The dashed line is the bisecting line. (b) FTIR meaurement of a FZ-Si sample coated with hydrogen-rich silicon nitride on both surfaces. The absorption peaks related to silicon-nitrogen bonds, silicon-hydrogen bonds and to nitrogen-hydrogen bonds allow for the calculation of the overall hydrogen concentration within the film.

is calculated from the measured transmission T corrected by the baseline:

$$\alpha = \frac{-\log_{10}(T)}{\log_{10}(\mathrm{e})d} \approx 2.3026\frac{-\log_{10}(T)}{d} \tag{3.9}$$

with d being the SiN$_x$ film thickness. Note that d is the total film thickness including the front and the rear side coating. With the absorption coefficient α, the concentration of the bond in question is [53]:

$$[\mathrm{X}-\mathrm{Y}] = K([\mathrm{X}-\mathrm{Y}]) \int_{\nu_{\text{lower}}}^{\nu_{\text{upper}}} \alpha(\nu)\mathrm{d}\nu. \tag{3.10}$$

The absorption peak area is located between the wavenumbers ν_{lower} and ν_{upper} and multiplied with the calibration factors shown in table 3.1. Note that the concentrations determined via FTIR are averaged over the whole film thickness.

3.2.3 Nuclear Reaction Analysis (NRA)

In contrast to the FTIR method described in the subsection before, the Nuclear Reaction Analysis (NRA) allows for depth-resolved hydrogen profiling. Double positively charged nitrogen ions of the isotope ^{15}N are irradiated onto the sample and react with protons at

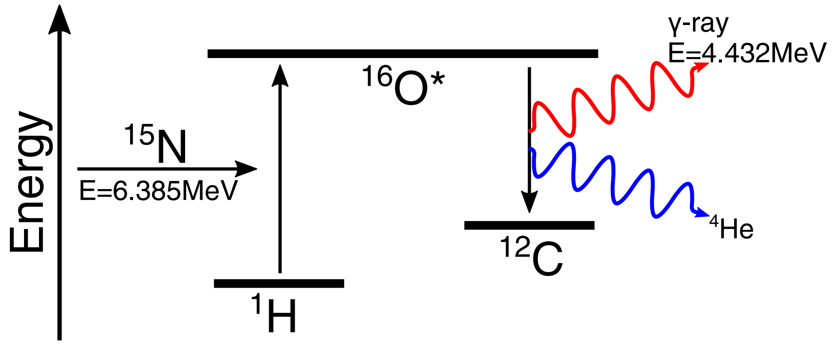

FIGURE 3.6: Working principle of the NRA measurements performed in this thesis.

rest in a resonant reaction:

$$^{15}\mathrm{N} + {}^{1}\mathrm{H} \longrightarrow {}^{16}\mathrm{O}^{*} \longrightarrow {}^{12}\mathrm{C} + {}^{4}\mathrm{He} + \gamma \tag{3.11}$$

at an energy of the incident nitrogen isotopes of 6.385 MeV [54]. Each reaction is accompanied by the emission of a gamma-ray with an energy of E_γ = 4.432 MeV, hence, the count rate of those gamma-rays can be directly correlated to the hydrogen content. By adjusting the energy of the nitrogen isotopes and exploiting the fact that the isotopes lose energy while passing through the thin film, the location of the resonant reaction changes, enabling depth-resolved measurements. Since the resonance of the nuclear reaction is quite narrow with 12 keV, this results in a depth resolution of $\approx$ 5 nm in silicon nitride films [54]. Assuming a constant stopping power for each silicon nitride film, the energy offset of the incident ion beam to the resonance energy is converted into a depth information. The count rate of the gamma-rays is calibrated to the total amount of hydrogen using a reference material with known hydrogen content. Figure 3.6 shows the working principle of the NRA method used in this thesis. The experiments are performed at the Helmholtz-Zentrum Dresden-Rossendorf using a 6 MeV tandem accelerator. The experimental setup allows measurements with a limit of detection of 0.02 atom percent hydrogen.

3.2.4 Rutherford Backscattering Spectroscopy (RBS)

Rutherford Backscattering Spectroscopy (RBS) is used for the determination of the composition of the silicon nitride films (silicon-to-nitrogen ratio) and the areal atomic density σ_{atom}. We use $^{4}\mathrm{He}^{+}$ ions with an incident energy of 1.7 MeV at a scattering angle of

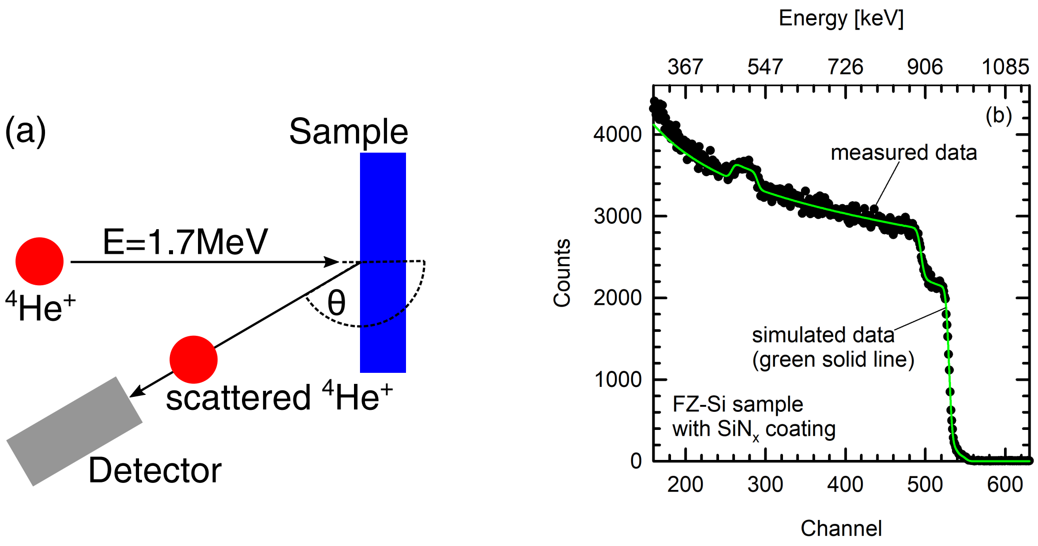

FIGURE 3.7: (a) Working principle of the RBS measurements performed in this thesis. (b) RBS measurement result for a FZ-Si sample coated with silicon nitride. The measurements are evaluated by fitting simulated data (green solid line) to the measured data (black circles).

$\theta = 170°$. The helium ions scatter at the atoms within the thin film, whereby a part of their kinetic energy is transferred onto the scatter partner. A schematic of the measurement principle is shown in Fig. 3.7(a). Since the energy loss depends on the mass of the scatter partner, energy-resolved detection of the scattered helium ions enables the identification of atoms present in the thin film. Thus, the measurement results are energy-resolved counts of helium ions leaving the thin film after scatterring, as shown in Fig. 3.7(b). For the evaluation of the results, the SimNRA software is used [55].

Evaluation of the data includes fitting the measured data points. The fit variables are the thin film composition (i.e. fractions of the involved elements) and the areal atomic density σ (i.e. the count of atoms per area). By combining RBS measurements with another independent method, such as ellipsometry for the determination of the film thickness, the mass density of the film ρ can be determined:

$$\rho = (m_{\mathrm{Si}} \cdot c_{\mathrm{Si}} + m_{\mathrm{N}} \cdot c_{\mathrm{N}} + m_{\mathrm{H}} \cdot c_{\mathrm{H}})\,\frac{\sigma}{d}, \tag{3.12}$$

with m being the mass per atom of the respective element, c the fraction of the respective element in the film and d the film thickness. Note that hydrogen cannot be detected in the RBS measurements, since it is lighter than the used projectile. This error is corrected within the evaluation of the RBS data, because the hydrogen concentration within the respective film is known from NRA measurements.

The RBS experiments were performed at the Helmholtz-Zentrum Dresden-Rossendorf using a 2 MeV van de Graaff accelerator.

Chapter 4

Light-induced lifetime instabilities in multicrystalline silicon

Solar cells fabricated on multicrystalline silicon show a pronounced degradation upon illumination at elevated temperature ($\gtrsim 50\,^\circ$C), as first reported by Ramspeck et al. [6]. Ramspeck et al. [6] were not able to explain this effect by known degradation mechanisms such as the boron-oxygen defect activation [7–9] or the iron-boron pair dissociation [10, 11] and, hence, attributed the effect to a new degradation mechanism. Since the degradation is particularly pronounced in mc-Si solar cells with an Al_2O_3/SiN_x-passivated rear surface, this degradation mechanism strongly interferes with the introduction of mc-Si passivated emitter and rear solar cells (PERC) into the market [6, 12, 13].

In this chapter, the light-induced degradation at elevated temperature (LeTID) is investigated on mc-Si lifetime samples. To elucidate the underlying defect physics, the impact of various sample treatments on the carrier lifetime degradation and regeneration cycles is examined.

4.1 Sample processing

The as-cut silicon wafers are first cleaned with a surface-active agent and subsequently etched in a potassium hydroxide solution followed by a chemical polishing process based on hydrofluoric and nitric acids to remove the saw damage. After an RCA cleaning sequence, a phosphorus diffusion is then performed in a quartz-tube furnace at a process temperature of $\approx 850\,^\circ$C resulting in n^+-layers on both wafer surfaces with a sheet resistance between 50 and 60 Ω/sq (except the samples without phosphorus diffusion in subsection 4.4). This process step is known to effectively getter metallic impurities from the silicon bulk into the n^{+}-layers [56]. The phosphosilicate glass is etched back using hydrofluoric acid and the n^{+}-layers are removed (except for the group A samples in subsection 4.2) using the same chemical polishing process as used for the saw damage removal. After an RCA cleaning sequence, the samples are coated with 10 nm aluminium oxide (Al_2O_3) single layers (samples in subsection 4.7), 100 nm silicon nitride (SiN_x) single layers (samples from group A in 4.2) or with a stack passivation consisting of 10 nm Al_2O_3 and 100 nm SiN_x (samples in subsections 4.3, 4.4, 4.5, 4.6 and 4.7) [5]. The Al_2O_3 layers are deposited using plasma-assisted atomic layer deposition (PA-ALD) in a FlexAL system (Oxford Instruments) and the SiN_x layers are deposited using plasma-enhanced chemical vapor deposition (PECVD) in a SiNA tool (Meyer Burger). However, for the samples examined in group B in subsection 4.2, we use a stack passivation of 5 nm Al_2O_3 deposited by thermal ALD in an InPassion LAB system (SolayTec) and 100 nm SiN_x deposited by the SiNA tool. For the results presented in this chapter, the refractive index of the SiN_x layers, measured at a wavelength of 633 nm, is tuned to $n = 2.05$. Both deposition techniques will be described in more detail within the next sections. Finally, the samples receive a rapid thermal annealing (RTA) treatment in an industrial conveyor-belt furnace (DO-FF-8.600-300, centrotherm international AG). This high-temperature treatment corresponds to the contact firing, which is the last process step during the production of solar cells with screen-printed contacts. Throughout this study, a constant belt-speed of 6.8 m/min is applied at a set-peak temperature varying between 650 and 900 °C.

ALD of Al_2O_3

Within this thesis, PA-ALD and thermal ALD are used for the deposition of Al_2O_3 layers. Atomic layer deposition is a highly conformal deposition technique and allows precise control of the film thickness.

In the PA-ALD process, the precursor for the aluminium is tri-methyl-aluminium (TMA), which is injected into the process chamber and binds to hydroxyl (OH) groups at the silicon wafer surface. In a second step, the aluminium is oxidized by an inductively coupled remote oxygen plasma. In order to remove the remaining precursor and any byproducts, the chamber is purged with oxygen after each cycle. This prepares the next deposition

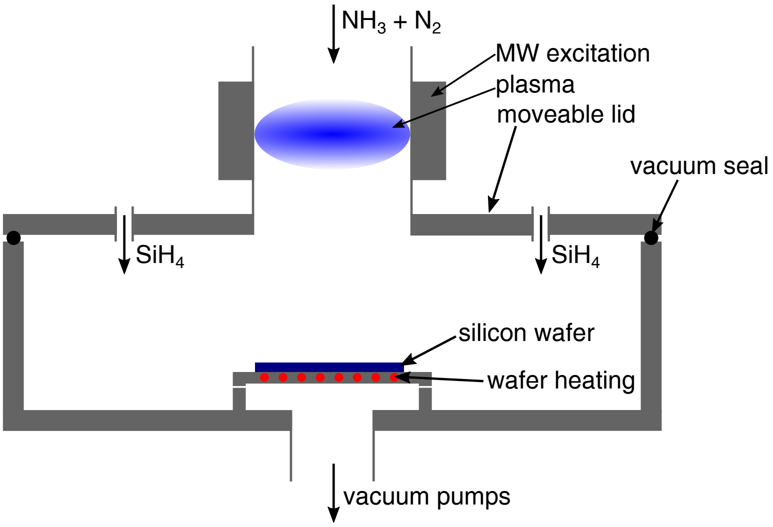

FIGURE 4.1: Schematic of the Oxford Plasmalab 80 Plus remote-PECVD tool used for SiN$_x$ deposition in this thesis.

cycle which deposits another monolayer of aluminium oxide. To facilitate the reactions during the depositon, the wafers are placed on a heated stage with typical temperatures around 200 °C. We use the commercially available FlexAL system (Oxford Instruments) for PA-ALD deposited layers.

In contrast to the PA-ALD process, the thermal ALD process uses gaseous water instead of an oxygen plasma for the oxidation of the aluminium. We use the commercially available InPassion LAB (SolayTec) tool for the layers deposited by thermal ALD.

PECVD of SiN$_x$

Within this thesis, we use two different plasma-enhanced chemical vapor deposition (PECVD) tools for the deposition of SiN$_x$ layers. The first one is an industrial-type inline tool (SiNA, Meyer Burger) and the second one is a labscale tool (Oxford Plasmalab 80 Plus, Oxford Instruments). Both tools use ammonia (NH$_3$) and silane (SiH$_4$) as process gases, although the Plasmalab 80 Plus uses a mixture of ammonia and nitrogen (N$_2$) and the SiNA uses additional hydrogen (H$_2$) as process gas. Both tools excite the NH$_3$ by microwave radiation with a frequency of 2.45 GHz. In contrast to the direct-PECVD method, where the silicon wafer is in direct contact with the plasma, both deposition systems applied here use a remote plasma (remote-PECVD), where the plasma is spatially separated from the wafer. The advantage of the remote-PECVD method in comparison to the direct-PECVD method is the reduced ion bombardment of the wafer, which leads to a decrease in surface damage [43]. The excited NH_3 reacts with the separately injected SiH_4 in the chamber and forms a SiN_x film on the silicon surface. By changing the ratio between the SiH_4 gas flow and the NH_3 gas flow, SiN_x films with different silicon-to-nitrogen ratios are obtained. The silicon-to-nitrogen ratio has a pronounced impact on the SiN_x film properties such as refractive index and atomic density. To facilitate the formation of the SiN_x film on the wafer surface, the wafer is placed on a heating element with typical temperatures between 300 and 500 °C. The thickness of the SiN_x film is adjusted via the process time. The resulting SiN_x films are typically rich in hydrogen, since the hydrogen from the process gases is partly incorporated into the films. A schematic of the Oxford Plasmalab 80 Plus used in this thesis is shown in Fig. 4.1.

In contrast to the Oxford lab-type tool, the industrial-type SiNA deposition tool features a moving sample carrier, which transports the silicon wafers through five process chambers. The first process chamber is the entry loadlock, where the wafers are pre-heated at a temperature of 350 °C. Pre-heating is continued in the second chamber. Subsequently, the deposition of the SiN_x films takes place in the third chamber at a set-temperature of typically 500 °C. In the fourth chamber, the samples cool down. Finally, the last chamber is the exit loadlock. The thickness of the film is adjusted via the speed of the sample carrier. Details of the SiNA system have been published by Moschner et al. [57].

4.2 Lifetime degradation and regeneration

Within this thesis, we investigate the different stages of the carrier lifetime evolution in mc-Si lifetime samples under illumination at elevated temperatures. The samples are divided into two groups, with one group not having the n^+-layers etched back after phosphorus diffusion (group A). Samples from group A receive a passivation with SiN_x single layers, while the samples without n^+-layers (group B) receive an Al_2O_3/SiN_x stack passivation. Samples from group A represent the front side of a PERC solar cell, whereas the samples from group B represent the rear side of such a solar cell. The sample architecture for both groups is shown in the insets in Fig. 4.2. All silicon nitride layers are deposited

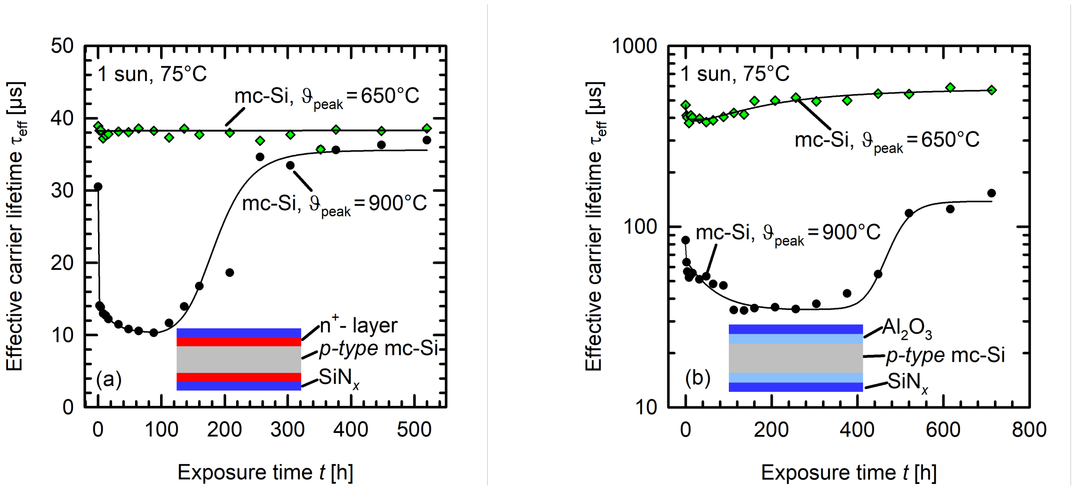

FIGURE 4.2: Effective carrier lifetime of mc-Si lifetime samples from (a) group A and (b) group B plotted versus the exposure time to an illumination of 1 sun at 75 °C. The solid lines are guides to the eyes.

using the industrial-type PECVD tool (SiNA) resulting in layers with a refractive index of $n = 2.05$ and a thickness of $d = 100$ nm.

The carrier lifetimes of samples both with and without n^+-layers show a pronounced degradation after rapid thermal annealing (RTA) at a set-peak temperature of 900 °C, as can be seen in the lifetime measurements in Figs. 4.2(a) and 4.2(b). The observed degradation can be subdivided into two stages. The first stage is finalised within the first 2 hours and is characterized by a fast and pronounced reduction in lifetime. This stage is followed by a slower exponential degradation, terminating within $\approx$ 100 h. The presence of two stages of degradation was also observed on mc-Si solar cells in the study of Ramspeck et al., where the published degradation data cannot be fitted with a single-exponential decay, but require a fast initial plus a slow degradation component. The detailed kinetics of the degradation is discussed in section 4.5. Figures 4.2(a) and 4.2(b) show that after complete degradation the lifetimes increase again (regeneration) and finally reach values even higher than the respective initial lifetime. Note that this study cannot exclude that the initial lifetime measurement has been performed in a slightly degraded state. If this has been the case, e.g. due to a degradation during the cool-down of the RTA treatment, the regeneration would not reach necessarily higher lifetimes than the initial ones, but just comprarable lifetimes to the initial state.

As a reference, monocrystalline Czochralski-grown silicon (Cz-Si) wafers are processed in parallel to the mc-Si wafers. On the boron-doped Cz-Si wafers with a resistivity of 4.5 Ω cm, the well-known degradation and regeneration processes associated with the boron-oxygen complex are observed, which are, however, very different concerning the time constants compared to our observations on mc-Si. The lowest effective carrier lifetime measured on the Cz-Si reference wafers was 124 µs for group A and 671 µs for group B, thus well above the highest lifetimes of the corresponding mc-Si samples. Hence, this study shows for the first time that a degradation of the surface passivation quality of the samples cannot be considered as the main cause of the observed behaviour and that the lifetime evolution is due to a recombination center in the silicon bulk. Nakayashiki et al. confirmed more recently that the evolution of the carrier lifetime is indeed caused by a bulk defect [58]. They etched back the passivation layers of mc-Si PERC semifabricates after complete degradation and repassivated the samples by submerging them in hydrofluoric acid. Because the passivation layers have been replaced, their results show that the degradation effect on their samples is not due to a loss in surface passivation quality.

4.3 Impact of rapid thermal annealing

Within this thesis, we show for the first time that samples RTA-treated with a reduced peak temperature of 650 °C remain stable in group A and show a very weak degradation from an initial lifetime of 472 µs to a lifetime of 375 µs in the case of group B, as can be seen in Fig. 4.2. The temperature range between 650 °C and 900 °C is chosen to cover the range of relevant temperatures in a typical solar cell fabrication process and to clearly separate the impact of different peak temperatures on the degradation and regeneration extents. On another set of lifetime samples, we investigate the dependence of the maximum defect density on the measured RTA peak temperature in more detail, as shown in Fig. 4.3. The mc-Si samples with a base resistivity of 1.4 Ω cm are passivated with an Al_2O_3/SiN_x stack of 10 nm Al_2O_3 and 100 nm SiN_x with a refractive index of n = 2.05. All samples were pre-gettered and the set-peak temperature during RTA treatment is varied in the range from 650 to 900 °C in steps of 50 °C. After the firing step, the samples are exposed to the light of a halogen lamp at 0.5 suns illumination intensity and 120 °C, until the maximum defect density is reached. In Fig. 4.3, the maximum defect density N^*_{max} is plotted versus the actual measured peak temperature $\vartheta_{\text{firing.actual}}$

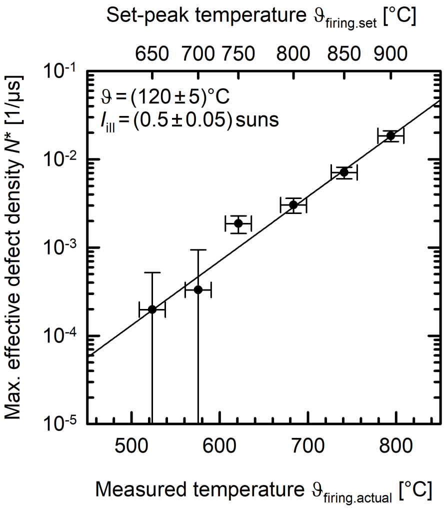

FIGURE 4.3: Maximum defect density N^*_{max} of neighboring 1.4 Ω cm mc-Si wafers with Al_2O_3/SiN_x stack passivation degraded at 0.5 suns illumination and 120 °C plotted versus the measured peak temperature $\vartheta_{firing.actual}$ during the RTA treatment. The top axis displays the corresponding set-peak temperature. The solid line is an exponential fit to the data points.

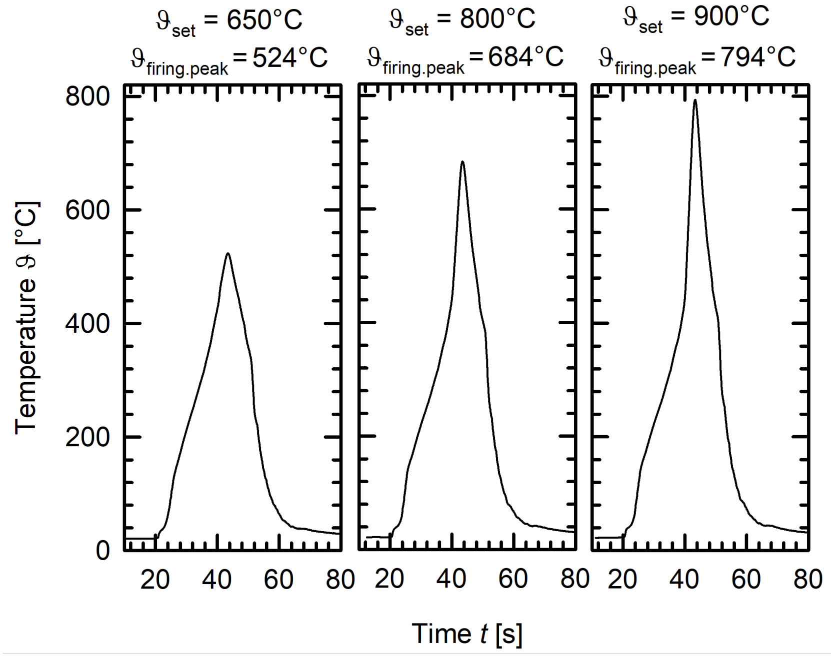

FIGURE 4.4: Measured temperature profiles during RTA treatment for the mc-Si lifetime samples investigated in Fig. 4.3 plotted versus the measurement time. The measurements are shifted that the temperature peaks are located at the same time. The actual sample temperature is tracked using a temperature tracker (DQ1860A, Datapaq) and a type-K thermocouple (KMQXL-IM050-300, Omega).

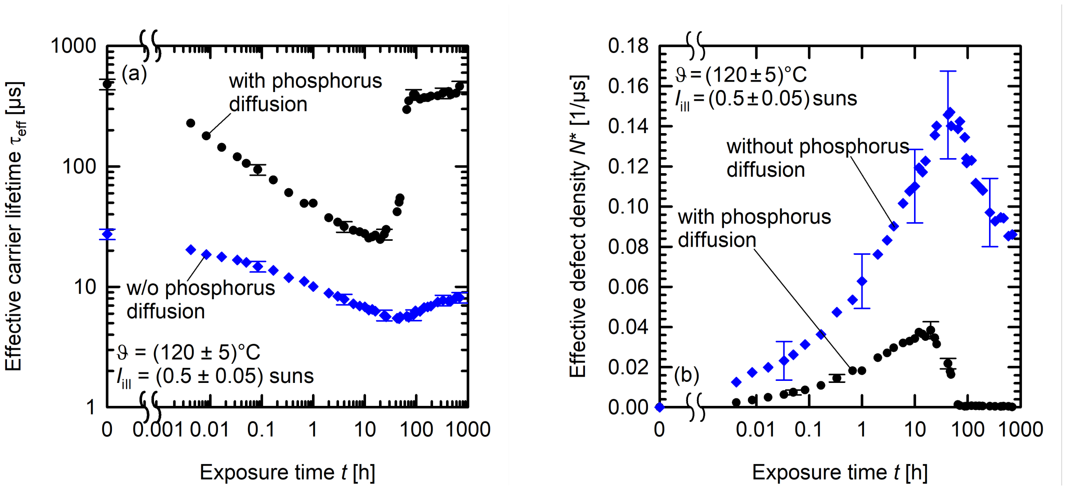

FIGURE 4.5: (a) Effective carrier lifetime of neighboring 1.4 Ω cm high-performance mc-Si wafers plotted versus the exposure time at 0.5 suns illumination and 120 °C. One mc-Si sample received a phosphorus diffusion and subsequent removal of the diffused region (black circles), while the other sample received no phosphorus diffusion (blue diamonds). Both wafer surfaces are passivated by Al_2O_3/SiN_x-stacks and are fired at 900 °C. (b) Effective defect density calculated from the data shown in (a) plotted versus the exposure time. The degradation extent on the samples without phosphorus diffusion is four times more pronounced than on samples that received a phosphorus diffusion.

during the firing step. We observe that the maximum defect density N^*_{max} drastically increases with increasing RTA temperature. Chan et al. published a study showing a similar dependence of the maximum defect density on the peak temperature during RTA treatment [59]. Figure 4.4 shows the temperature profiles during RTA treatment exemplarily for three different set-peak temperatures of 650, 800 and 900 °C. Note that with increasing set-peak temperature not only the measured peak temperature increases, but also the heating and cooling rates. This might as well impact the maximum defect density, since Eberle et al. reported that either the ramp-up and ramp-down rates or a longer time above a certain threshold temperature have a significant influence on the degradation in mc-Si lifetime samples [60].

4.4 Impact of phosphorus gettering

Figure 4.5(a) shows the lifetime evolution of two neighbouring high-performance mc-Si samples with Al_2O_3/SiN_x stack passivation after RTA treatment at 900 °C. Prior to surface passivation, one sample received a phosphorus diffusion step, known to effectively getter metallic impurities from the silicon bulk [56]. The n^{+}-diffused regions were removed by etching prior to surface passivation. Both samples show a pronounced degradation in their lifetime, however, the degradation is about four times more pronounced in terms of the maximum defect density for the non-diffused sample. This result is in good agreement with published results from Zuschlag et al., who reported that phosphorus gettering significantly decreases the degradation extent [61]. Since the lifetime on the non-diffused sample in the fully degraded state is only 5.5 µs and the excess carrier concentration at constant illumination intensity is proportional to the carrier lifetime, this results in a relatively low excess carrier concentration. As will be discussed in section 4.5, the degradation rate depends on the excess carrier density. Thus, the degradation rate of the non-diffused sample (blue diamonds in Fig. 4.5) is expected to be smaller than in the diffused sample. The non-diffused sample reaches the maximum degradation after $\approx$ 46 h in contrast to the diffused sample that reaches the maximum degradation after about 20 h. In addition, the slow regeneration observed on the non-diffused sample can be attributed to a correlation of the regeneration rate with the excess carrier concentration. Note that the carrier lifetime of a FZ-Si reference sample shows a lifetime evolution similar to that described by Sperber et al. [62]. However, the carrier lifetime in the FZ-Si reference sample remains above 1 ms throughout the entire observed time period. Hence, there is no relevant impact of a change in the surface passivation quality on the measured lifetimes in the examined mc-Si samples.

4.5 Impact of illumination intensity and temperature

4.5.1 Temperature dependence of degradation kinetics

For the first time, we investigate the detailed kinetics of the carrier lifetime degradation in mc-Si lifetime samples. Figures 4.6(a) and 4.6(b) show measurements at a constant illumination intensity of 0.5 suns at temperatures ranging from 75 to 120 °C. For all temperatures, a two-stage lifetime degradation is observed: a fast stage and a subsequent slow stage. Thus, it is not possible to fit the effective defect density $N^{*}(t)$ evolution with a

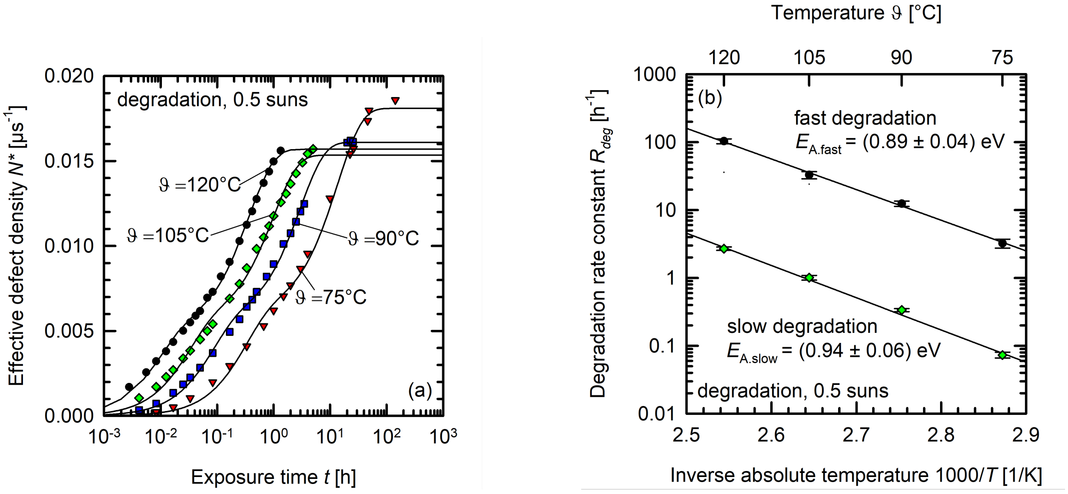

FIGURE 4.6: (a) Measured effective defect density N^* calculated from lifetime measurements versus the exposure time t in hours with double-exponential rise-to-maximum fits (solid lines). Degradation conditions are 0.5 suns light intensity and temperatures ranging from 75 to 120 °C. (b) Degradation rate constants R_{deg} of the fast and slow stages of degradation plotted versus the inverse absolute temperature $1/T$ with fits according to the Arrhenius law.

mono-exponential rise-to-maximum fit. However, using a sum of two exponential rise-to-maximum fits, an excellent agreement with the experimental $N^*(t)$ evolution is observed:

$$N^*(t) = a\left(1 - \exp(-R_{\mathrm{deg.fast}}t)\right) + b\left(1 - \exp(-R_{\mathrm{deg.slow}}t)\right), \tag{4.1}$$

with a and b being pre-factors determining the maximum defect concentration. We extract the fast and slow degradation rates from this double-exponential fit. Figure 4.6(b) shows an Arrhenius plot of the respective degradation rate constants $R_{\mathrm{deg.fast}}$ and $R_{\mathrm{deg.slow}}$ according to Eqn. 4.1 with the temperature-independent pre-factor κ_0, the activation energy E_A, the Boltzmann constant k_B and the absolute temperature T:

$$R_{\mathrm{deg}} = \kappa_0 \cdot \exp\left(-\frac{E_A}{k_B T}\right). \tag{4.2}$$

From the Arrhenius fit, we obtain an activation energy of $E_{\mathrm{A.fast}} = (0.89 \pm 0.04)$ eV for the fast stage and $E_{\mathrm{A.slow}} = (0.94 \pm 0.06)$ eV for the slow stage. Note that the difference in the two activation energies is within the respective measurement uncertainties. Hence, both activation energies are very similar or even identical. The pre-exponential factors κ_0 determined at 0.5 suns illumination intensity differ, however, significantly by one order of magnitude: $\kappa_{0.\mathrm{fast}} = 8.26 \times 10^9\,\mathrm{s}^{-1}$ for the fast stage and $\kappa_{0.\mathrm{slow}} = 9.37 \times 10^8\,\mathrm{s}^{-1}$

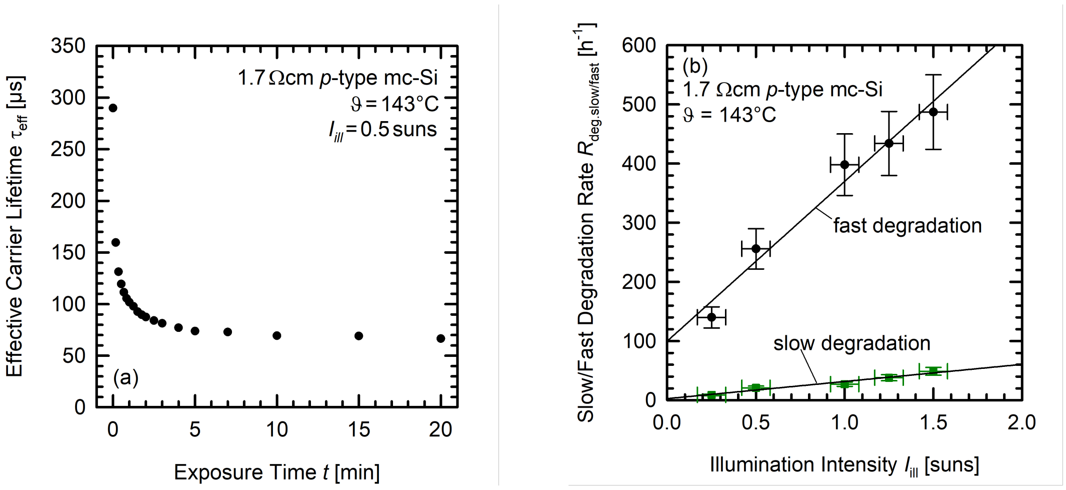

FIGURE 4.7: (a) Evolution of the carrier lifetime τ_{eff} under illumination at 0.5 suns light intensity and a temperature of 143 °C. The lifetime drops from initially 290 µs to 60 µs within 20 min. (b) Degradation rate constants $R_{deg.fast}$ and $R_{deg.slow}$ at 143 °C of the fast and slow degradation components versus the illumination intensity I_{ill} in suns (black circles and green squares) with linear fits (solid lines).

for the slow stage of degradation. As can be seen in Fig. 4.7(a), the relatively large activation energy of the slow degradation leads to a full degradation at 143 °C within 20 min on the examined sample. The lifetime drops from initially 290 µs to 66 µs after 20 min. Upon further illumination at elevated temperature the lifetime regeneration sets in. Based on the activation energy of the slow degradation, this degradation would take 56 h at a reduced temperature of 75 °C until the minimum lifetime is reached.

4.5.2 Illumination intensity dependence of degradation kinetics

The experiments to determine the impact of the applied illumination intensity on the degradation kinetics are carried out at a constant sample temperature of 143 °C. The illumination intensity is varied from 0.25 to 1.5 suns. As can be seen in Fig. 4.7(b), the degradation rate constants $R_{deg.fast}$ and $R_{deg.slow}$ show a linear increase with the applied illumination intensity I_{ill} at constant temperature. With $a_{slow} = (29.4 \pm 4.9)\,\text{suns}^{-1}\text{h}^{-1}$, $a_{fast} = (271.9 \pm 99.3)\,\text{suns}^{-1}\text{h}^{-1}$, $b_{slow} = (2.6 \pm 4.7)\,\text{h}^{-1}$ and $b_{fast} = (99.3 \pm 33.3)\,\text{h}^{-1}$, the illumination dependence can be expressed as follows:

$$R_{deg.fast} = a_{fast} \cdot I_{ill} + b_{fast}, \tag{4.3}$$

$$R_{deg.slow} = a_{slow} \cdot I_{ill} + b_{slow}. \tag{4.4}$$

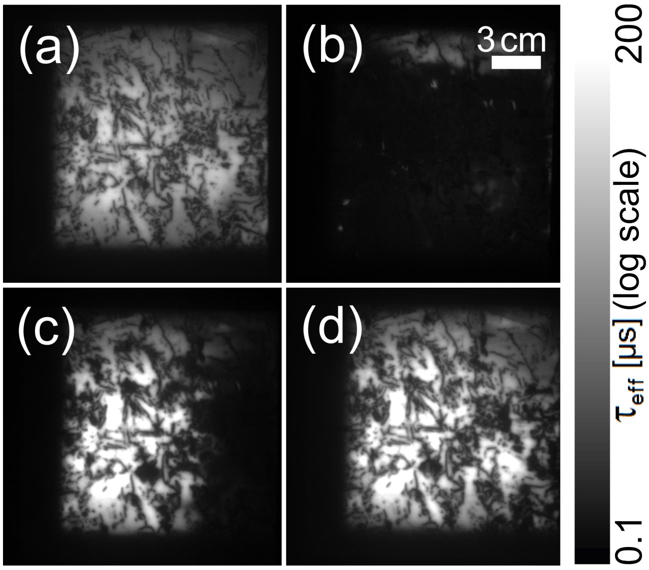

FIGURE 4.8: Carrier lifetime images measured by PC-PLI of an mc-Si lifetime sample at different timesteps during illumination at 1 sun light intensity and 75 °C. (a) Initial state, (b) after 48 hours of illumination, (c) after 448 hours, (d) after 616 hours. The carrier lifetime regeneration clearly proceeds from the left to the right of the wafer, corresponding to a wedge profile of the wafer thickness with the left side of the wafer being 21 µm thinner than the right.

Note that $b_{\text{fast}} \gg 0$, which would indicate that there is a fast degradation stage even without illumination. However, the lowest illumination intensity applied in this thesis is 0.25 suns. It can be conjectured that the dependence of the fast degradation rate on the illumination intensity changes for very low intensities.

Kwapil et al. observed that the degradation rate of mc-Si PERC solar cells depends almost linearly on the excess carrier density at the p-n junction [63]. They applied different forward bias voltages to the solar cells in the dark at a temperature of 75 °C and measured the current through the solar cell. Since this current is proportional to the change in the effective defect density, they extracted the degradation rate from the evolution of the current. The results from Kwapil et al. fit well with the findings of this thesis that the degradation rates depend linearly on the applied illumination intensity.

4.6 Impact of wafer thickness

For the first time, we show that there is a pronounced dependence of the carrier lifetime evolution on the wafer thickness. In this thesis, a series of lifetime degradation and regeneration measurements on mc-Si lifetime samples of various thicknesses are performed.

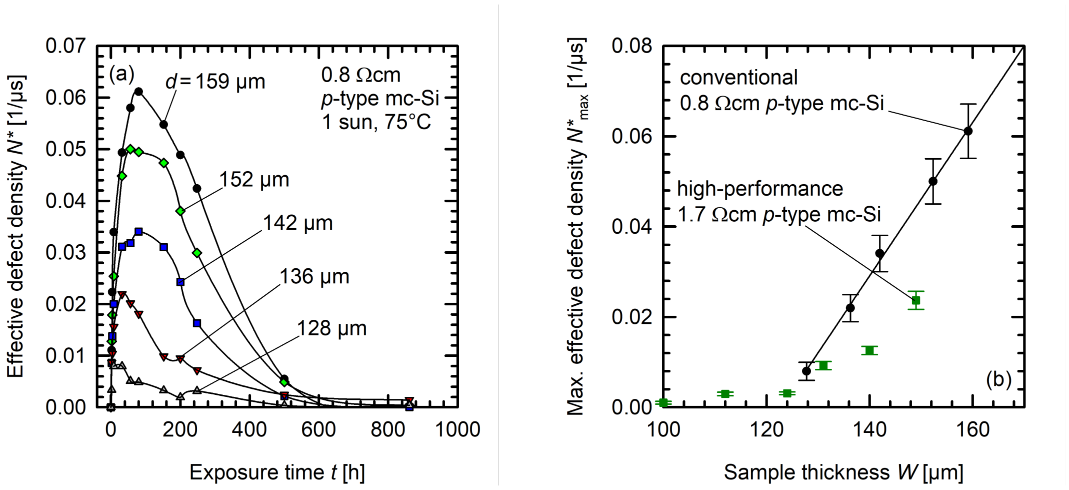

FIGURE 4.9: (a) Evolution of the effective defect concentration $N^*(t)$ extracted from lifetimes measured using the QSSPC technique on 0.8 Ω cm p-type mc-Si wafers of various thicknesses during 1 sun illumination intensity at 75 °C. The solid lines are guides to the eyes. (b) Maximum defect concentration N^*_{max} extracted from (a) (black circles) plotted versus the sample thickness d. The solid line is a linear fit to the measured data. The fit indicates that no pronounced degradation is expected for mc-Si wafers thinner than ≈ 120 µm for the degradation conditions applied within this thesis. In addition, measurements taken on high-performance mc-Si wafers (green squares) are shown, which experimentally confirm the negligible degradation extent for wafer thicknesses below ≈ 120 µm.

Figure 4.8 shows spatially resolved carrier lifetime measurements at different times during the degradation and regeneration cycle. The excitation level is chosen to result in an area-averaged excess carrier concentration of $1 \times 10^{14}\,\text{cm}^{-3}$. Both the fast and slow degradation stages occur relatively homogeneously over the wafer area. However, the lifetime regeneration starts locally and then proceeds from left to right over the wafer. This observation can be explained by a thickness dependence of the carrier lifetime regeneration, since the wafer features a wedge profile with the left side being 21 µm thinner than the right side. Note that the edge regions show a reduced lifetime even in the initial lifetime images due to impurities diffusing from the crucible into the bulk material during the crystallization process ('red zone') [17].

In a second experiment, we investigate the thickness dependence in more detail with wafer thicknesses ranging between 128 and 159 µm. The mc-Si samples with a base resistivity of 0.8 Ω cm receive an RTA treatment at a constant set-peak temperature of 900 °C. The actual sample temperature is tracked using a temperature tracker and a type-K thermocouple within the furnace on equally processed wafers. The measured peak temperature slightly increases with decreasing wafer thickness, however, within the thickness range examined in this thesis, the maximum temperature increase is less than 10 °C. Therefore, the impact of the RTA peak temperature shown in section 4.3 on the carrier lifetime evolution does not significantly affect the results shown in this section.

Figure 4.9(a) shows the time evolution of the effective defect density $N^*(t)$ of the species responsible for the degradation effect in the mc-Si wafers on samples with different thicknesses ranging from 128 to 159 µm at 1 sun illumination intensity kept at 75 °C. The effective defect density of the 159 µm thick mc-Si wafer significantly increases within the first 80 h of illumination and decreases under prolonged illumination until after $\approx$ 600 h the sample has been completely regenerated, that is $N^*(t) \approx 0$. As can be seen from Fig. 4.9(a), the sample thickness has a pronounced impact on the lifetime evolution. The maximum defect density N^*_{max} decreases by a factor of $\approx$ 6 when decreasing the wafer thickness from 159 to 128 µm. Figure 4.9(b) shows a plot of the N^*_{max} data extracted from Fig. 4.9(a), as a function of the sample thickness W (black circles). In the examined thickness range, the $N^*_{\mathrm{max}}(W)$ dependence is perfectly linear. Based on the linear fit shown as a solid line in Fig. 4.9(b), one implication of this thesis is that one would not expect a pronounced lifetime degradation for mc-Si wafers thinner than $\approx$ 120 µm under the given degradation conditions. We confirmed this hypothesis experimentally on 1.7 Ω cm high-performance mc-Si wafers shown as green squares in Fig. 4.9(b), which are etched back to a thickness down to 100 µm. Note that the overall degradation extent in the high-performance mc-Si material seems to be lower than in the conventional mc-Si material, which is probably due to the lower metal contamination in the high-performance state-of-the-art material. The negligible degradation extent, however, for very thin mc-Si wafers can be clearly verified in this experiment.

4.7 Impact of surface passivation schemes

Figure 4.10(a) shows the lifetime evolution of one mc-Si sample passivated with an Al_2O_3/SiN_x stack and one mc-Si sample passivated with Al_2O_3 single layers. Both samples, featuring a base resistivity of 1.4 Ω cm, received a phosphorus diffusion step. On the sample with the Al_2O_3/SiN_x stack passivation, a pronounced degradation and subsequent regeneration of the carrier lifetime under illumination at an intensity of 0.5 suns and an elevated temperature of 120 °C is observed. The lifetime decreases from initially

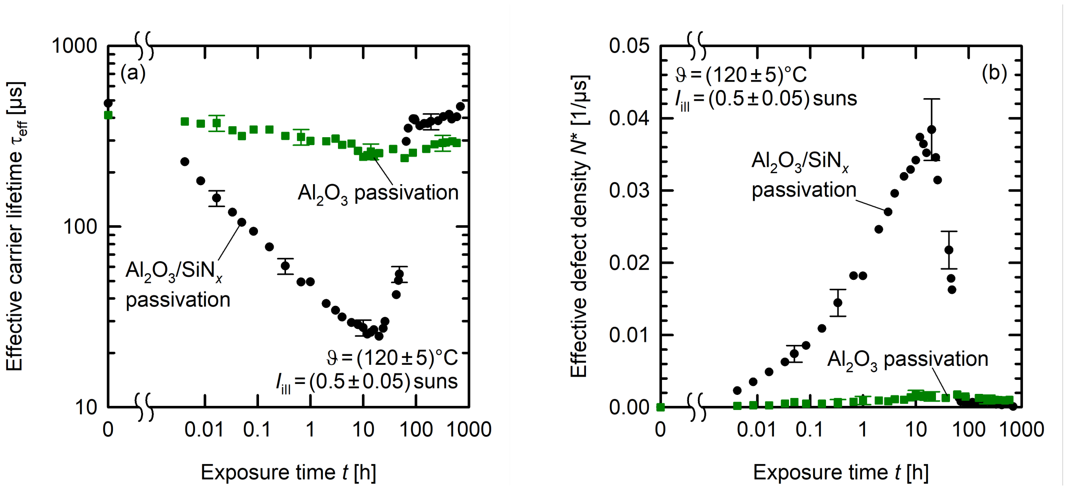

FIGURE 4.10: (a) Effective carrier lifetimes of neighboring 1.4 Ω cm mc-Si wafers plotted versus the exposure time at 0.5 suns illumination and 120 °C. One wafer is symmetrically passivated with an Al_2O_3/SiN_x-stack (black circles) and the other wafer is symmetrically passivated with Al_2O_3 single layers (green squares). (b) Effective defect density calculated from the lifetime values shown in (a) plotted versus the exposure time. The degradation on wafers passivated with Al_2O_3/SiN_x-stacks is 20 times more pronounced than on samples passivated with Al_2O_3 single layers.

481 µs to 25 µs within 20 h. In contrast to that, the sample passivated with Al_2O_3 single layers only shows a slight degradation from initially 414 µs to a minimum of 244 µs after 10 h of illumination and a subsequent regeneration to a saturation lifetime value of 291 µs after 589 h. The corresponding effective defect densities are plotted in Fig. 4.10(b). The degradation extent on samples with Al_2O_3/SiN_x stack is about 20 times more pronounced than on identically processed neighboring mc-Si wafers passivated with Al_2O_3 single layers. These results point towards the involvement of hydrogen in the carrier lifetime limiting defect in mc-Si, since hydrogen is known to diffuse from hydrogen-rich passivation layers into the silicon upon RTA treatment [64]. Since silicon nitride films typically contain more hydrogen than aluminium oxide films, this would be consistent with the results shown above that silicon wafers passivated with Al_2O_3 single layers do not show a pronounced degradation of the carrier lifetime.

Kersten et al. also reported that mc-Si lifetime samples passivated with Al_2O_3 single layers show a less pronounced carrier lifetime degradation than the samples passivated with SiN_x single layers or with Al_2O_3/SiN_x stacks. However, their samples with Al_2O_3 single layer passivation still show a carrier lifetime decrease from initially about 70 µs to 20 µs. This might be due to different deposition tools and that the actual film properties depend on the deposition conditions of the respective film. Furthermore, Kersten et al.

found that mc-Si lifetime samples with the passivation layers absent during RTA treatment do not show a pronounced carrier lifetime degradation [65]. The involvement of hydrogen would explain the lack of a pronounced carrier lifetime degradation if the samples are RTA treated without a passivation layer (i.e. without any hydrogen source) on the sample surface.

Therefore, we investigate the impact of hydrogen in the passivation layers and in the silicon bulk on LeTID in detail in the next chapter.

4.8 Chapter summary

Within this chapter, we performed a series of experiments on mc-Si lifetime samples to elucidate the effect of light and elevated temperature induced degradation (LeTID). We showed that mc-Si lifetime samples both with and without n^+-layers show a pronounced carrier lifetime degradation under illumination and elevated temperature (1 sun, 75 °C) for samples which received an RTA treatment at a set-peak temperature of 900 °C. Reducing the RTA peak temperature led to a strong decrease of the degradation extent. At a set-peak temperature of 650 °C only a weak lifetime degradation was observed. In addition, a phosphorus gettering step significantly decreased the degradation extent compared to samples that received no phosphorus diffusion. A comparison with Cz-Si samples processed in parallel showed that a degradation of the surface passivation quality cannot be considered the root cause of the observed behaviour and that the lifetime evolution is due to the activation of a recombination center in the silicon bulk.

For the first time, we investigated the detailed kinetics of the defect activation in dependence of both temperature and illumination intensity. We showed that the lifetime degradation takes place in two stages: a fast stage followed by a slow stage. From an Arrhenius fit of the degradation rates in a temperature range from 75 to 120 °C, we extracted an activation energy of $E_{\mathrm{A.fast}} = (0.89 \pm 0.04)\,\mathrm{eV}$ for the fast stage and of $E_{\mathrm{A.slow}} = (0.94 \pm 0.06)\,\mathrm{eV}$ for the slow stage. Keeping the temperature constant at 143 °C and varying the illumination intensity between 0.25 and 1.5 suns led to a linear dependence of both degradation rates on the illumination intensity.

Furthermore, we showed for the first time that mc-Si lifetime samples with sample thicknesses between 128 and 159 µm show a pronounced dependence of the carrier lifetime degradation and regeneration on the sample thickness. The regeneration proceeds faster and the degradation extent decreases the thinner the wafer is. We showed that samples thinner than $\approx$ 120 µm show a negligible degradation.

Finally, we demonstrated that the degradation extent depends on the surface passivation scheme. Multicrystalline silicon lifetime samples passivated with Al_2O_3 single layers only showed a negligible carrier lifetime instability. However, adding a SiN_x film on top of the Al_2O_3 layer, led to significant LeTID. This points towards the involvement of hydrogen, because SiN_x films are known to be hydrogen-rich and release part of their hydrogen into the silicon bulk upon RTA at sufficiently high temperature.

Chapter 5

Correlation of LeTID in multicrystalline silicon with in-diffused hydrogen

5.1 In-diffusion of hydrogen into silicon

Many beneficial effects in silicon photovoltaics are associated with hydrogen being present in the silicon bulk. The so-called 'hydrogenation' of the silicon bulk may passivate lifetime-limiting bulk defects [66, 67]. In addition, hydrogen can also passivate interface defects, improving the effectiveness of surface passivation layers on silicon [68, 69]. This 'hydrogenation' is typically performed by depositing a hydrogen-rich SiN$_x$ film on the surface of a silicon wafer. Upon RTA treatment, hydrogen is released from the SiN$_x$ film mainly into the environment, but partly into the hydrogen bulk [70]. As shown in section 4.7, there is a pronounced impact of the passivation scheme on the degradation and regeneration cycles in mc-Si. Only the sample involving a hydrogen-rich SiN$_x$ film in the passivation scheme shows the pronounced lifetime evolution.

Within this chapter, we deposit silicon nitride films with different compositions and film properties on mc-Si wafers and the respective film properties are correlated to the extent of the defect activation after RTA treatment. Furthermore, we deposit the same broad variation of SiN$_x$ films on parallel processed FZ-Si samples and the film properties are linked to the fraction of hydrogen introduced into the silicon bulk during RTA. We deduce the bulk hydrogen concentration in the FZ-Si wafers after RTA from measurements of resistivity changes of the silicon bulk due to the formation of boron-hydrogen pairs.

TABLE 5.1: Process parameters applied for the deposition of SiN_x films in this study. The films are deposited using the Oxford Plasmalab 80 Plus remote-PECVD tool. The film thickness is adjusted by changing the process time.

Process parameter	Set Value
Silane gas flow	1.5 to 21 sccm
Ammonia gas flow	200 sccm
Nitrogen gas flow	100 sccm
Chamber pressure	150 mTorr
Deposition temperature	400 °C
Microwave excitation power	150 W
Microwave excitation frequency	2.45 GHz

This experiment is performed on mc-Si and FZ-Si wafers with a base resistivity of 1.2 Ω cm. The SiN_x films are deposited using remote-PECVD in an Oxford Plasmalab 80 Plus tool with the process parameters listed in Table 5.1. All samples receive an RTA treatment at a set-peak temperature of 900 °C, resulting in measured peak temperatures of $\theta_{\text{peak}} = (767 \pm 8)\,°\text{C}$ for the mc-Si samples and $\theta_{\text{peak}} = (743 \pm 10)\,°\text{C}$ for the FZ-Si samples. In both cases the measured peak temperatures show no major dependence on the composition of the respective silicon nitride film. As the final process step, the wafers are cut into 45 mm × 45 mm samples. The final thickness is (150 ± 5) µm for the mc-Si samples and (162 ± 3) µm for the FZ-Si samples.

5.2 SiN_x material properties

With increasing silane gas flow during the SiN_x deposition, the silicon content in the resulting SiN_x film increases and thus also the refractive index n measured by ellipsometry at a wavelength of 633 nm. Applying the minimum silane gas flow in this study of 1.5 sccm results in a nearly stoichiometric silicon nitride film with a refractive index of $n = 1.93$. In contrast to that, the maximum gas flow in this study of 21 sccm results in a very silicon-rich film with a refractive index of $n = 3$. As shown in Fig. 5.1(a), the dependence of the silicon-to-nitrogen ratio Si/N on the refractive index n can be described by our newly introduced empirical quadratic relationship:

$$\text{Si/N} = 0.69 \cdot n^2 - 1.75 \cdot n + 1.62, \tag{5.1}$$

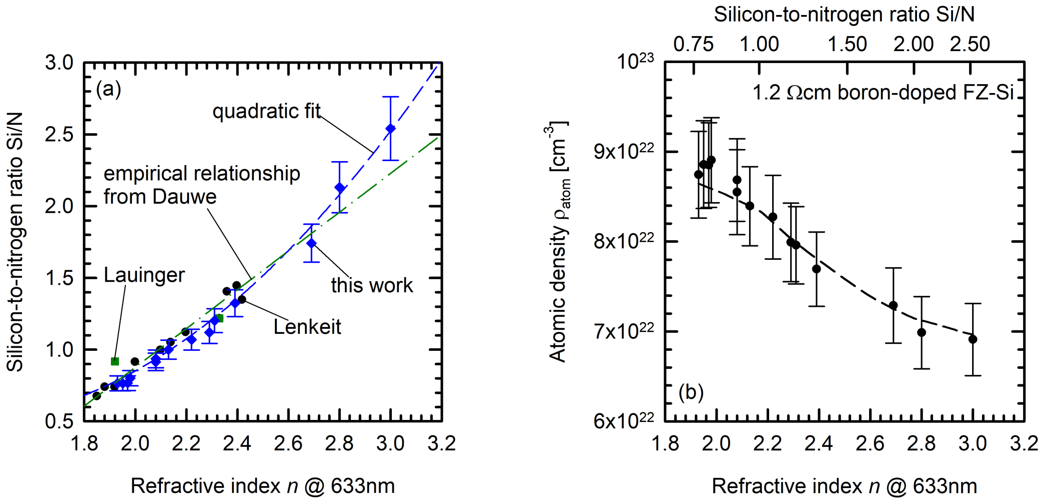

FIGURE 5.1: (a) Silicon-to-nitrogen ratio plotted versus the refractive index n of SiN$_x$ films. The refractive index is well known to increase with increasing silicon content of the films. The dashed line is a quadratic fit including all data points (see Eqn. 5.1). The green dashed-dotted line is a linear fit from Dauwe [71]. The black data points (circles) are taken from Lenkeit [72] and the green data points (squares) are taken from Lauinger [73]. The blue data points are measured in this work. All measurements are carried out on remote-PECVD deposited films at a set-temperature of 400 °C. (b) Measured atomic density ρ_{atom} of the SiN$_x$ films plotted versus the refractive index n measured at a wavelength of 633 nm (lower axis) and the silicon-to-nitrogen ratio (upper axis). The dashed line is a guide to the eyes.

with Si/N being the silicon-to-nitrogen ratio. Dauwe reported the empirical relationship Si/N = $1.35 \cdot n - 1.82$ (green dashed-dotted line), however, with most of the data points in the range of $n < 2.4$ [71]. Within this thesis, we show for the first time, that a linear empirical relationship between the silicon-to-nitrogen ratio and the refractive index cannot be used for silicon-rich SiN$_x$ films, i.e. for SiN$_x$ films with a high refractive index ($n > 2.4$). Therefore, our new quadratic relation given by Eqn. 5.1 as dashed blue line and shown in Fig. 5.1(a) is used throughout this thesis.

Figure 5.1(b) shows that the atomic density ρ_{atom} of the SiN$_x$ films depends on the silicon-to-nitrogen ratio of the film and thus also on the refractive index. Nearly stoichiometric SiN$_x$ films with a refractive index close to $n = 1.9$ show the highest atomic density. With increasing silicon content and thus refractive index, the atomic density decreases. This is due to the silicon atoms: Despite having a higher mass than the nitrogen atoms, they feature a larger covalent radius of 1.17 Å compared to 0.7 Å for the nitrogen atoms [74].

As shown in Fig. 5.2(a), the concentration of silicon-hydrogen bonds [Si-H] increases with increasing refractive index n of the SiN$_x$ film and thus with increasing silicon content.

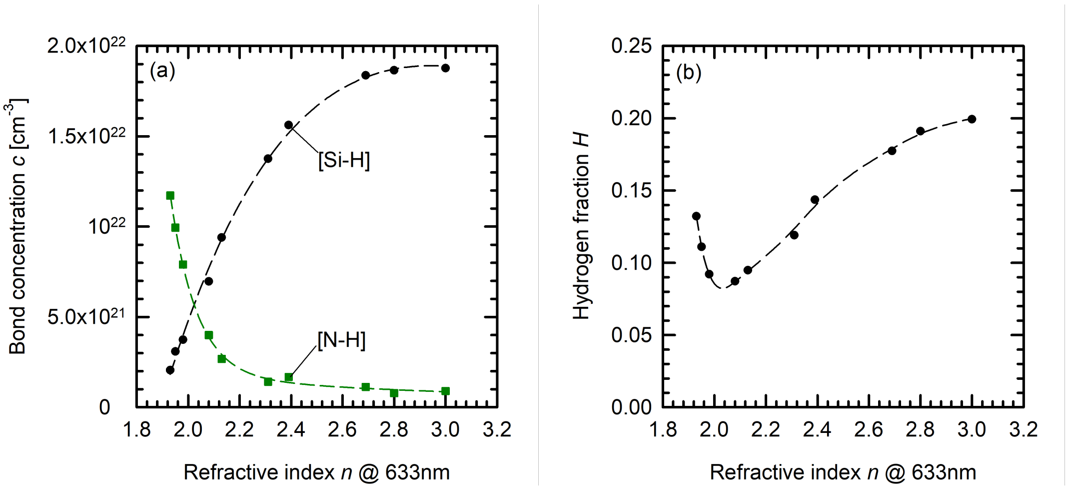

FIGURE 5.2: (a) Concentration of silicon-hydrogen (Si-H) bonds and of nitrogen-hydrogen (N-H) bonds plotted versus the refractive index n measured at a wavelength of 633 nm. The Si-H bond concentration increases with increasing refractive index and thus increasing silicon content. The N-H bond concentration increases with decreasing refractive index and thus increasing nitrogen content. The dashed lines are guides to the eyes. (b) Hydrogen fraction in the SiN_x films after deposition plotted versus the refractive index n measured at a wavelength of 633 nm. The hydrogen fraction shows a minimum at $n \approx 2$ and increases with increasing and decreasing n. The dashed line is a guide to the eyes.

In contrast to that, the concentration of nitrogen-hydrogen bonds [N-H] decreases with increasing silicon content, but strongly increases for a refractive index of $n \lesssim 2$. Figure 5.2(b) shows that the hydrogen fraction in SiN_x films, calculated according to Eqn. 3.8, increases with increasing refractive index ($n \gtrsim 2$) and with decreasing refractive index ($n \lesssim 2$). For silicon-rich silicon nitride films ($n \gtrsim 2.3$) the hydrogen fraction is mainly determined by the concentration of Si-H bonds in the film. With decreasing refractive index n, the concentration of Si-H bonds strongly decreases and thus the hydrogen fraction of nitrogen-rich SiN_x films with $n \lesssim 2$ is mainly determined by the N-H bond concentration. This bond concentration strongly increases towards nearly stoichiometric films and thus the hydrogen fraction shows a minimum at a refractive index of $n \approx 2$.

5.3 Impact of SiN_x composition on LeTID

Figure 5.3 shows the impact of SiN_x films on the maximum LeTID extent on mc-Si samples with different Si/N ratios and thus varying refractive indices n. To separate beween effects stemming from the SiN_x composition and the film thickness, the films used in Fig.

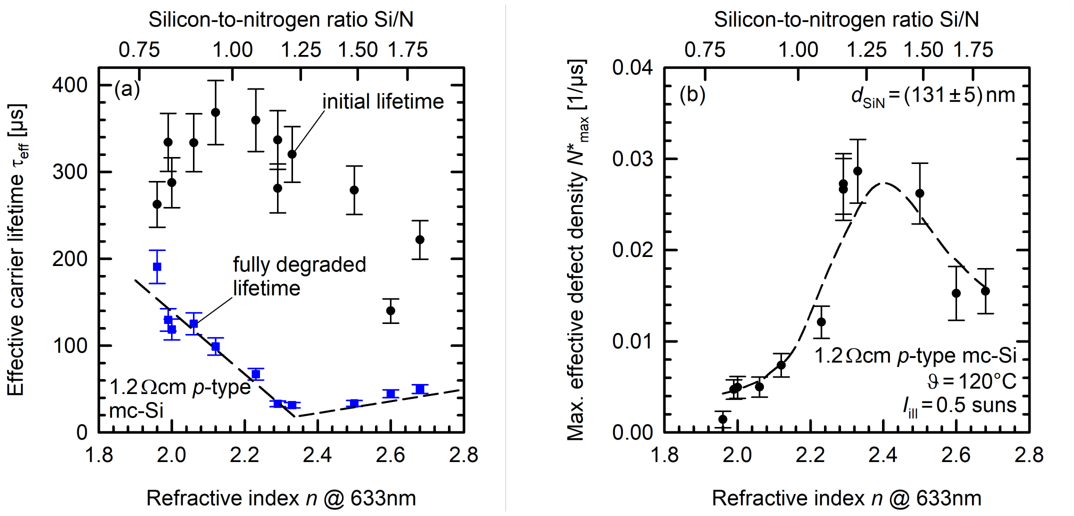

FIGURE 5.3: (a) Effective carrier lifetime τ_eff and (b) maximum effective defect density N^*_max of 1.2 Ω cm *p*-type mc-Si samples plotted versus the refractive index *n* of the deposited SiN$_x$ layers (lower axis) and the corresponding silicon-to-nitrogen ratio (upper axis) of the SiN$_x$ film. The SiN$_x$ film thickness is constant at d_SiN = (131 ± 5) nm. The dashed lines are guides to the eyes.

5.3 have a constant film thickness of (131 ± 5) nm. The sample with the lowest refractive index of $n = 1.96$ only shows a weak degradation from 263 µs after RTA treatment to 191 µs in the fully degraded state. The degradation extent strongly increases with increasing refractive index up to a value of $n = 2.33$. For this sample, the lifetime drops from initially 320 µs down to 31 µs in the fully degraded state, which is reached after 10.2 h at an illumination intensity of 0.5 suns and a temperature of 120 °C. There seems to be a broad peak in the maximum degradation extent between $n = 2.33$ and $n = 2.5$. For even higher refractive indices, the degradation extent decreases up to a refractive index of $n = 2.68$. Unfortunately, samples with refractive indices above $n = 2.7$ show a pronounced surface recombination increase after RTA treatment. Thus, the defect activation cannot be clearly distinguished from effects stemming from the surface recombination on those samples.

5.4 Impact of SiN$_x$ film thickness on LeTID

Figure 5.4 shows the LeTID extent as a function of the SiN$_x$ film thickness d_SiN using a constant refractive index of $n = 2.28$. The lifetimes in the fully degraded state decrease with increasing film thicknesses between 74 and 105 nm, thus the degradation extent

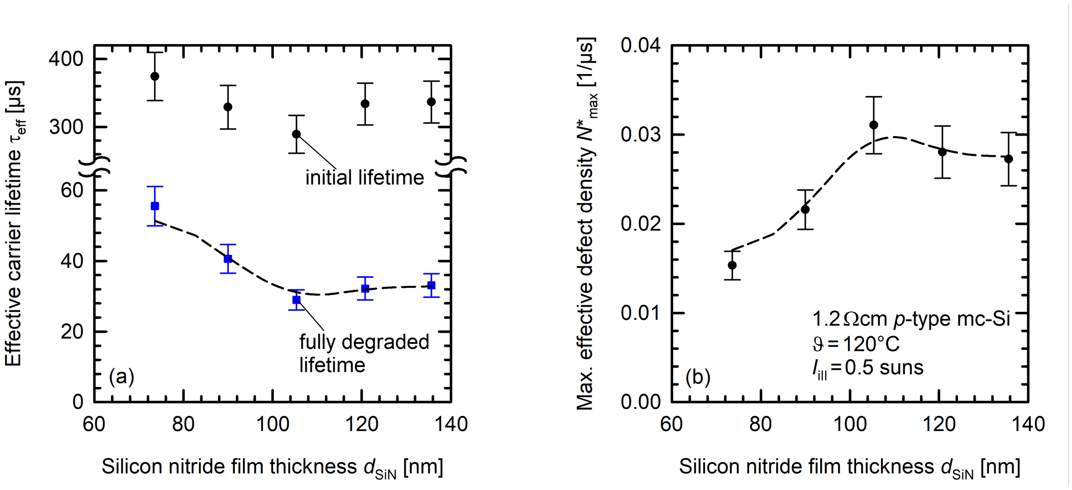

FIGURE 5.4: (a) Effective carrier lifetime τ_{eff} and (b) maximum effective defect density N^*_{max} plotted versus the silicon nitride film thickness d_{SiN}. The refractive index of the silicon film is kept constant at $n = 2.28$ (measured at a wavelength of 633 nm). The dashed lines are guides to the eyes.

increases. However, the degradation extent seems to saturate for film thicknesses above 105 nm up to the maximum investigated film thickness of 136 nm.

5.5 Determination of the bulk hydrogen concentration

In order to correlate the findings of sections 5.3 and 5.4 with the actual hydrogen concentration diffused into the silicon bulk upon RTA treatment, we measure the evolution of boron-hydrogen (BH) pairs in FZ-Si [76]. Due to the formation of BH pairs, the base resistivity during dark annealing at 160 °C increases as shown in Fig. 5.5(a). According to the model of Voronkov and Falster, the hydrogen in the silicon bulk is largely quenched-in in the form of hydrogen dimers of a configuration $\text{H}_{2\text{A}}$ during cool down of the RTA process [75]. Upon annealing at 160 °C, these hydrogen dimers dissociate and the released atomic hydrogen forms boron-hydrogen pairs (BH pairs). Thus, the resistivity increases, because the fraction of boron bound in the BH pairs does no longer contribute to the sample's conductivity. Let $[\text{H}]_{2\text{A}}$ denote the concentration of hydrogen dimers of a configuration A [75]. Then, the evolution of $[\text{H}]_{2\text{A}}$ and [BH] is described by the differential equation [75]:

$$\frac{\mathrm{d}[\text{H}]_{2\text{A}}}{\mathrm{d}t} = -\alpha_A \left(p[\text{H}]_{2\text{A}} - \chi_A \left(\frac{\left(\frac{[\text{BH}]}{[\text{B}]}\right)^2}{p} \right) \right), \tag{5.2}$$

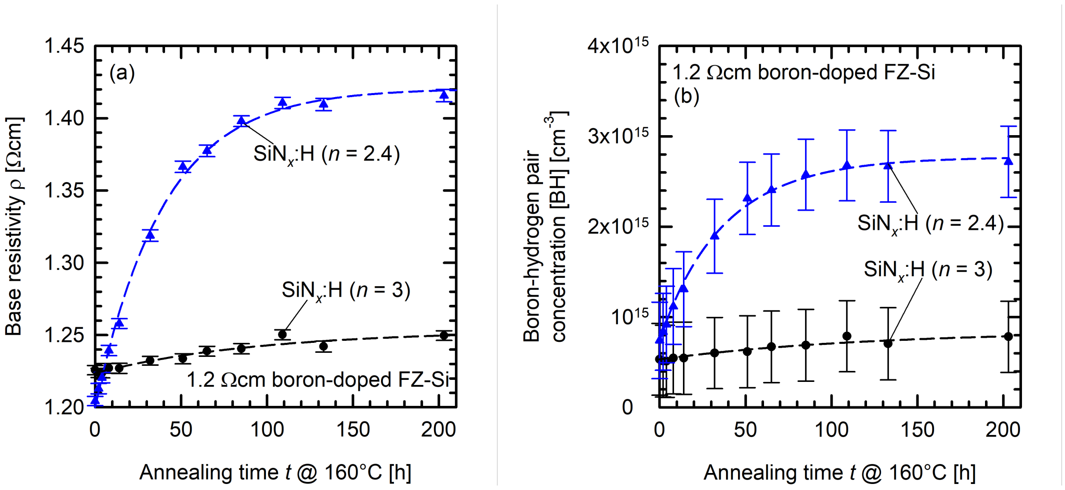

FIGURE 5.5: (a) Evolution of the base resistivity ρ plotted versus the annealing time t at 160 °C in the dark for boron-doped 1.2 Ω cm FZ-Si wafers. The blue triangles show a sample with large hydrogen concentration $[H]_{tot}$, while the black circles show a sample with a low $[H]_{tot}$. Uncertainties are given for the reproducibility of the measurements. The dashed lines are guides to the eyes. The base resistivity increases due to the formation of boron-hydrogen pairs. (b) Boron-hydrogen pair concentration [BH] calculated for the samples shown in (a). The dashed lines are fits according to the model of reference [75] with $\chi_A = 4 \times 10^{46}\,\text{cm}^{-9}$ and α_A and $[H]_{tot}$ as free fit parameters. Uncertainties are given including systematic deviations in our measurements.

with [B] being the concentration of boron that is not bound in BH pairs, p the hole concentration, α_A the dissociation rate constant of H_{2A} and χ_A an equilibrium constant. The total hydrogen concentration is the sum of the concentrations of BH pairs and the amount of hydrogen bound in H_{2A} dimers: $[H]_{tot} = [BH] + 2[H]_{2A}$. Figure 5.5(b) shows the calculated concentrations of BH pairs from the measured resistivity changes shown in Fig. 5.5(a) and the solution of Eqn. 5.2 (dashed lines) with $\chi_A = 4 \times 10^{46}\,\text{cm}^{-9}$ taken from Voronkov and Falster [75]. Least-square fitting shows that all samples can be well described by $\alpha_A = (4.8 \pm 1.0) \times 10^{-22}\,\text{cm}^{-3}\text{s}^{-1}$. Figure 5.6(a) shows the extracted total hydrogen concentrations $[H]_{tot}$ in the silicon bulk versus the refractive index n measured at a wavelength of 633 nm of the respective SiN$_x$ coating. The SiN$_x$ film thickness is constant with $d_{SiN} = (131 \pm 7)\,\text{nm}$. The minimum hydrogen concentration in the silicon bulk after RTA treatment is measured for nearly stoichiometric SiN$_x$ films with n close to 1.9. The total hydrogen concentration $[H]_{tot}$ increases with increasing refractive index n up to a refractive index of $n \approx 2.4$. For further increasing refractive indices, however, $[H]_{tot}$ decreases again with increasing n, that is increasing silicon content in the SiN$_x$ film. Figure 5.6(b) shows the maximum effective defect density N^*_{max} of mc-Si lifetime samples plotted versus the total hydrogen concentration $[H]_{tot}$ in FZ-Si wafers processed in parallel to the

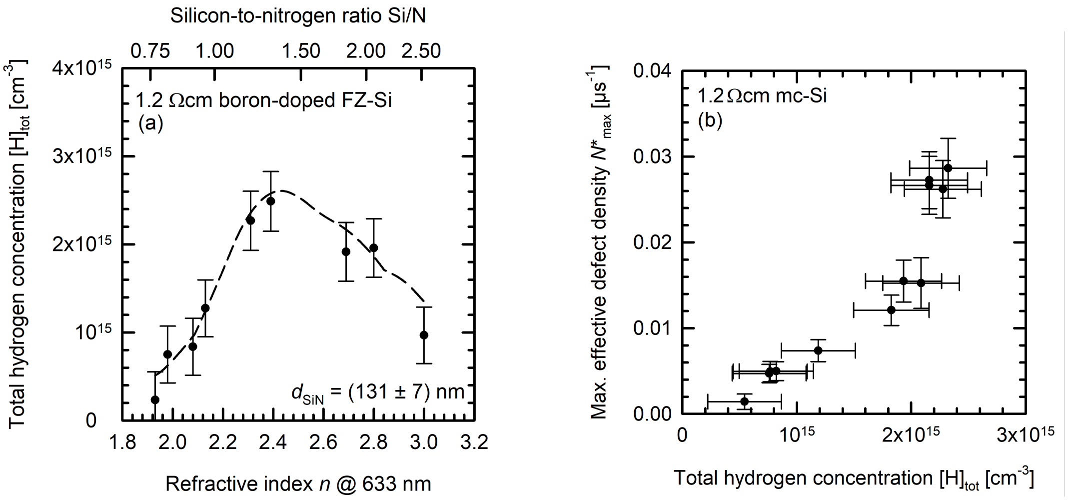

FIGURE 5.6: (a) Total hydrogen concentration $[H]_{tot}$ after RTA treatment of SiN_x-coated FZ-Si wafers plotted versus the refractive index n of the SiN_x films measured at a wavelength of 633 nm. The dashed line is a guide to the eyes. (b) Maximum effective defect density N^*_{max} of mc-Si wafers extracted from Fig. 5.3 plotted versus the total hydrogen concentration $[H]_{tot}$ extracted from (a) (interpolated piecewise linear). The degradation extent in mc-Si shows a pronounced positive correlation with the hydrogen content introduced from SiN_xfilms during RTA.

mc-Si samples. The total hydrogen concentration in the FZ-Si samples is interpolated piecewise linear to fit with the refractive indices of the SiN_x films on the mc-Si samples. The pronounced correlation between $[H]_{tot}$ and N^*_{max} depicted in Fig. 5.6(b) is a strong indication that hydrogen is directly involved in the carrier lifetime degradation observed on mc-Si lifetime samples. Note that the mean actual peak temperature during RTA treatment of the FZ-Si samples is 24 °C lower than on the mc-Si samples, which might lead to a reduced hydrogen in-diffusion on the FZ-Si samples compared to the mc-Si samples. It is assumed that this only affects the total hydrogen concentrations and not the qualitative comparisons between the samples. Also, note that the hydrogen diffusivity in FZ-Si and mc-Si might be different, which adds another uncertainty to the quantitative comparison between both sample types. However, the experimental results show no indication that the impact of the SiN_x composition and thickness on the hydrogen in-diffusion into the silicon bulk is qualitatively different on mc-Si material compared to FZ-Si.

5.6 Hydrogen in-diffusion during RTA

As shown in the previous section, our measurements reveal that the total hydrogen concentration $[H]_{tot}$ in the FZ-Si samples after RTA treatment reaches a maximum for SiN_x

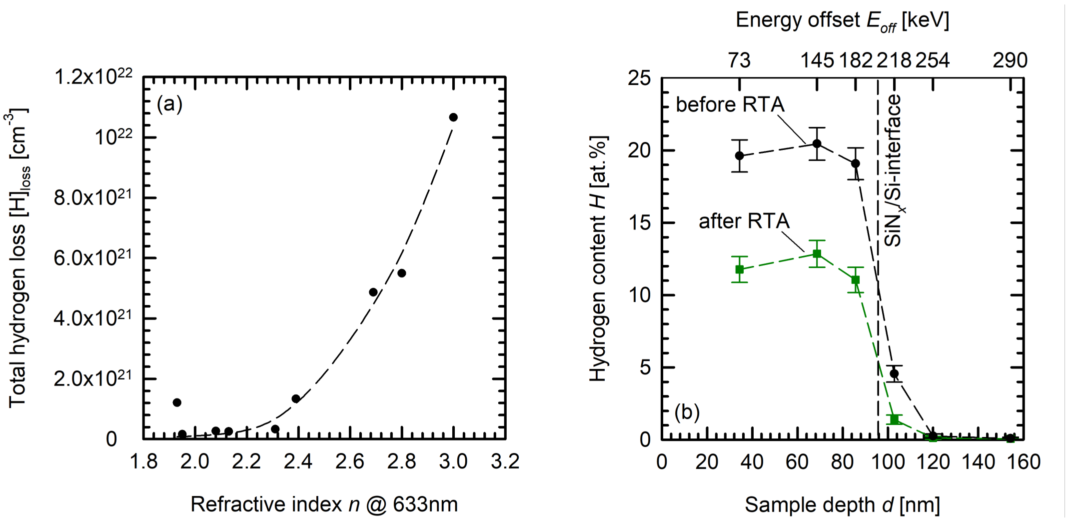

FIGURE 5.7: (a) Total hydrogen loss $[H]_{loss}$ of SiN_x films upon RTA treatment plotted versus the refractive index of the SiN_x film measured at a wavelength of 633 nm. Silicon nitride films with a high refractive index release more hydrogen during RTA treatment, while nearly stoichiometric films release the least hydrogen. The dashed line is a guide to the eyes. (b) Hydrogen content H of a 96 nm thick SiN_x film before and after RTA treatment plotted versus the thickness d of the film. The hydrogen depth profile is measured using the NRA method and scaled to the measured film thickness. The top axis displays the energy offset of the ion beam to the energy at which the nuclear reaction takes place. The approximate position of the Si/SiN_x interface is indicated by a vertical dashed line.

films with a refractive index n between 2.3 and 2.5 and decreases for higher and lower refractive indices, respectively. This finding is in good agreement with previous results of Hong et al., who showed that the degree of silicon bulk passivation, presumably due to a larger amount of hydrogen in the silicon bulk, increases with increasing mass density of the silicon nitride films [77]. According to the RBS measurements on our samples, the maximum mass density in the study of Hong et al. of $\rho \approx 2.5\,\mathrm{gcm}^{-3}$ corresponds roughly to a refractive index of $n \approx 2.4$ of the SiN_x films in this study. Thus, we can confirm that the amount of hydrogen introduced during RTA treatment increases with increasing refractive index up to $n \approx 2.4$.

Figure 5.7(a) shows the total hydrogen loss $[H]_{loss}$ calculated from the total hydrogen concentrations in the SiN_x films before and after RTA treatment. The total hydrogen concentrations in the respective SiN_x films are measured using FTIR. The hydrogen loss during RTA treatment increases with increasing refractive index n. This finding in combination with the finding displayed in Fig. 5.6(a) clearly shows that the total amount of hydrogen released from the SiN_x films during RTA treatment is no meaningful measure for the actual in-diffusion of hydrogen into the silicon bulk. The films with a refractive index of $n > 2.6$ show the largest hydrogen loss during RTA treatment, however, they introduce less hydrogen than SiN_x films with a refractive index of $n \approx 2.4$. This is because most of the hydrogen released from the SiN_x films diffuses into the environment. Figure 5.7(b) shows depth-resolved measurements of the hydrogen concentration in a SiN_x film before and after RTA treatment. Before the RTA treatment as well as after the RTA treatment, the hydrogen concentration is homogeneous along the film's thickness. Note that the depth resolution of the displayed measurement is not sufficient to show a possible build up of hydrogen due to the hydrogen diffusion during RTA treatment at the silicon/silicon nitride interface.

Our experimental results are interpreted in the framework of a defect model that includes the in-diffusion of hydrogen from hydrogen-rich SiN_x coatings into the silicon bulk during RTA treatment. Details of the defect model, which was developed in this thesis, are described in chapter 6. Our RBS measurements depicted in Fig. 5.1(b) show that the atomic density ρ_{atom} of the SiN_x films increases with decreasing refractive index n, thus stoichiometric SiN_x films have the highest atomic density. Since the hydrogen diffusivity in SiN_x films with a high atomic density is known to be low [78], hydrogen cannot effectively diffuse into the silicon bulk during RTA treatment (cf. Fig. 5.6(a), increasing hydrogen content with increasing refractive index for $n < 2.4$). With increasing refractive index, and thus decreasing atomic density, hydrogen becomes more mobile in the SiN_x layer and the fraction of hydrogen entering the silicon bulk increases. However, with decreasing atomic density the hydrogen in the SiN_x tends to form hydrogen dimers [52, 78]. Since those dimers cannot effectively diffuse into the silicon bulk, the hydrogen fraction in the silicon bulk decreases for the SiN_x films with the lowest atomic density, i.e. the highest refractive index (cf. Fig. 5.6(a), decreasing hydrogen content with increasing refractive index n for $n > 2.4$). Since the hydrogen in-diffusion depends largely on the film properties near the SiN_x/Si interface, an increase of the SiN_x film thickness impedes the out-diffusion of hydrogen from near the interface into the environment. Thus, the greater concentration gradient causes the hydrogen fraction in the silicon bulk to increase with increasing film thickness. However, for film thicknesses much larger than the diffusion length of hydrogen in SiN_x during RTA treatment, the fraction of hydrogen introduced into the silicon bulk saturates. Therefore, the maximum defect density N^*_{max} shown in Fig. 5.4 saturates for SiN_x film thicknesses larger than $\approx 105\,\mathrm{nm}$.

5.7 Chapter summary

In this chapter, we investigated the impact of hydrogen-rich SiN_x films of various compositions on the amount of hydrogen introduced into the silicon bulk during an RTA treatment. We measured the bulk hydrogen concentration on boron-doped FZ-Si samples by monitoring resistivity changes of the silicon bulk due to the formation of boron-hydrogen pairs. Most hydrogen was found to be introduced from silicon-rich SiN_x layers with a refractive index n (measured at a wavelength of 633 nm) between 2.3 and 2.5. For both higher and lower refractive indices (i.e. for higher and lower silicon-to-nitrogen ratios), the hydrogen amount in the silicon wafer decreases. Almost stoichiometric SiN_x films with a refractive index close to 1.9 were found to introduce the minimum hydrogen content into the silicon bulk. On mc-Si wafers, we showed for the first time that the LeTID extent directly correlates with the concentration of hydrogen introduced into the silicon bulk. The higher the hydrogen content in the silicon bulk, the more pronounced is the carrier lifetime degradation. In addition, we showed that LeTID on mc-Si lifetime samples depends on the SiN_x film thickness. The degradation extent increases with increasing film thickness (at a constant refractive index of $n = 2.28$) from 74 to 105 nm. However, the LeTID extent saturates for SiN_x film thicknesses larger than 105 nm up to the maximum investigated film thickness of 136 nm.

Our investigations of the SiN_x film properties revealed that the total hydrogen loss of the respective film during RTA is not a meaningful measure of the amount of hydrogen introduced into the silicon bulk. Furthermore, we derived a model explaining the dependence of the hydrogen bulk concentration on the respective SiN_x film properties.

Chapter 6

LeTID defect model

Based on the measurements presented in chapters 4 and 5, we propose a defect model including complexes of metal impurities with hydrogen. As described in the previous chapter, hydrogen diffuses from hydrogen-rich silicon nitride films into the silicon bulk upon RTA treatment. Also, during RTA treatment at sufficiently high temperature, latent precipitates of a particular metal M_p dissolve into most likely interstitial metal atoms M_i. This is a realistic assumption because of the high concentrations of metal impurities diffusing from the crucible into the mc-Si material during crystallization [17, 18]. In the model proposed in this thesis, the interstitial metal atoms M_i bind to hydrogen atoms in-diffused from the silicon nitride coating. The binding to hydrogen prevents the M_i from rejoining by forming M_i-H complexes. The resulting M_i-H complexes are no strong recombination centers or might even be completely recombination-inactive. However, upon illumination at elevated temperature, the M_i-H complexes reconfigure and eventually dissociate. The reconfigured M_i-H* complex and the interstitial metal atoms M_i are both assumed to be recombination-active, thus limiting the carrier lifetime by a two-stage lifetime degradation, as observed on the mc-Si samples (cf. Fig. 4.6). Meanwhile, the free hydrogen binds to other traps, abundant in mc-Si.

We further propose a model of the carrier lifetime regeneration, based on the pronounced wafer thickness dependence found in this thesis and described in detail in section 4.6. The pronounced wafer thickness dependence is explained by the recombination-active interstitial metal atoms M_i diffusing mainly to the wafer surfaces and to crystallographic defects, where they are trapped and become recombination-inactive. The defect model is summarized in Fig. 6.1, however note that for the sake of clarity the degradation is displayed as a single stage (i.e. the reconfigured M_i-H* stage is omitted).

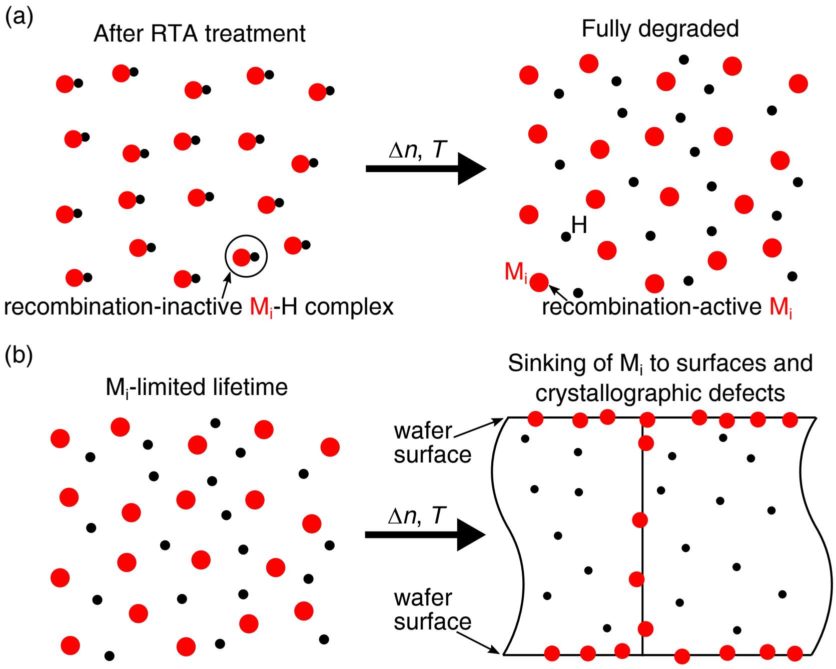

FIGURE 6.1: Suggested defect model for the carrier lifetime evolution in mc-Si. (a) Rapid thermal annealing at sufficiently high temperature introduces hydrogen from hydrogen-rich silicon nitride coatings into the silicon bulk and dissolves precipitates of metal impurities. The resulting metal-hydrogen complexes dissociate under illumination (i.e. excess carrier injection) at elevated temperature into highly recombination-active interstitial metal atoms and hydrogen. The reconfiguration of the M_i-H complexes leading to a two stage degradation is not shown. (b) Upon prolonged illumination at elevated temperature, the interstitial metal atoms diffuse to the wafer surfaces and crystallographic defects where they are trapped.

The following sections discuss the experimental results which led to the above-mentioned defect model. First, the experimental results with indications towards the involvement of a metal impurity in the lifetime-limiting defect are presented. Together with the results from chapter 5 concerning the direct involvement of hydrogen, this work concludes that metal-hydrogen complexes are most likely the root cause of LeTID in mc-Si. These results are accompanied by our experiments on mc-Si wafers with different thicknesses. Spatially resolved lifetime imaging reveals that the rate of the carrier lifetime regeneration strongly depends on the respective wafer thickness. Therefore, we propose the above-mentioned diffusion mechanism of metal atoms to the wafer surfaces, explaining the observed behaviour shown in Fig. 4.8. Furthermore, by numerical modelling of the proposed defect model, we extract the diffusion coefficient of the recombination-active species at a temperature of 75 °C.

6.1 Indications for the involvement of a metal impurity

As shown in chapter 5, there are strong indications that hydrogen is directly involved in the lifetime-limiting defect. However, the experimental results presented in this section point towards the involvement of a metallic impurity. This renders metal-hydrogen complexes, as proposed in the above-described defect model, the likely root cause of the LeTID effect.

6.1.1 Dependence on RTA peak temperature

There is a pronounced impact of the RTA peak temperature on the degradation extent, i.e. the maximum effective LeTID defect density. As can be seen from Fig. 4.3, the maximum effective defect density strongly increases with increasing peak temperature. In fact, for a low set-peak temperature of ϑ_{peak} = 650 °C only a very weak carrier lifetime degradation is observed (cf. Fig. 4.2(b)).

This behaviour can be explained by both the in-diffusion of hydrogen from hydrogen-rich surface passivation layers and the dissolution of metal precipitates into interstitial metal atoms during RTA treatment. Jiang et al. [70] showed that the amount of hydrogen diffusing from silicon nitride films into the silicon bulk during annealing depends on the temperature of the anneal. They observed that the bulk hydrogen concentration after annealing increases with increasing temperature. This is consistent with our defect model, since with increasing RTA peak temperature more hydrogen diffuses into the silicon bulk, preventing more interstitial metal atoms from rejoining into metal precipitates. On the other hand, the dissolution of metal precipitates also depends on the peak temperature during RTA. Lelièvre et al. [79] showed that the concentration of interstitial iron, stemming from the dissolution of iron precipitates in mc-Si wafers, increases with increasing RTA temperature. According to the proposed defect model, an increase in metal precipitate dissolution leads to an increase in degradation extent. In the proposed defect model, the presence of hydrogen as well as interstitial metal atoms is required, as the hydrogen is assumed to prevent the metal atoms from rejoining into metal precipitates. The metal precipitates are either recombination-inactive or recombination-active. However, in the latter case, they do not limit the carrier lifetime due to the low density of precipitates. Since the interstitial metal atoms are assumed to be highly recombination-active and the M_i density is large, the dissolution of metal precipitates during RTA limits the defect activation.

6.1.2 Dependence on phosphorus gettering

As shown in Fig. 4.5, mc-Si lifetime samples that underwent phosphorus gettering exhibit a pronounced reduction in the degradation extent compared to samples that received no phosphorus gettering step. Since phosphorus gettering is known to effectively getter metallic impurities from the silicon bulk [56, 80–82], this points towards the involvement of such a getterable impurity in the lifetime-limiting defect.

6.1.3 Injection-dependent lifetime spectroscopy

In order to characterize the recombination properties of LeTID we use injection-dependent lifetime measurements on mc-Si lifetime samples. Based on the approach described in more detail in subsection 2.3.4, the electron-to-hole capture cross-section ratio Q is extracted from injection-dependent lifetime measurements in the initial state and in the fully degraded state. We determine the Q value for the LeTID defect on two different high-performance mc-Si materials. The base resistivities are $1.6\,\Omega\,\text{cm}$ (material A) and

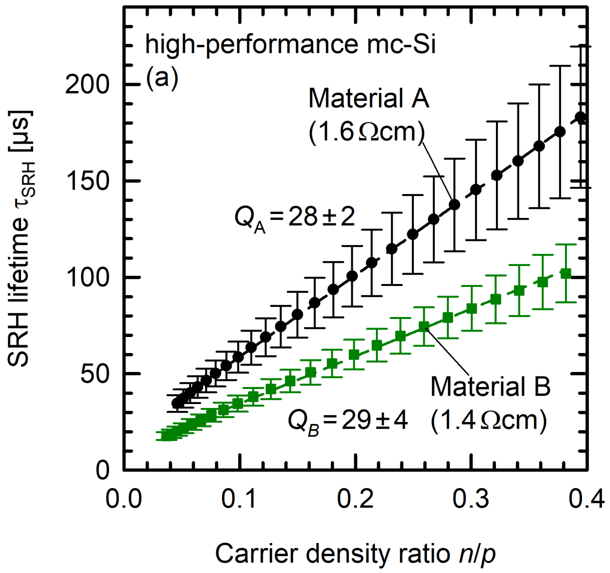

FIGURE 6.2: (a) SRH lifetime calculated from $\tau_{SRH} = \left(1/\tau_{min} - 1/\tau_0\right)^{-1}$ with τ_{min} the carrier lifetime in the fully degraded state and τ_0 the initial lifetime plotted versus the ratio of minority carriers to majority carriers. The Q values are extracted from linear fits to the calculated data, weighting the data points according to their respective uncertainty. The dashed lines are guides to the eyes.

1.4 Ω cm (material B). Under the assumption of a deep-level center, the Q value determined for material A is $Q_A = 28 \pm 2$ and $Q_B = 29 \pm 4$ for material B, as depicted in Fig. 6.2(a). The Q values for both materials are identical within the measurement uncertainty, indicating that the same defect center limits the carrier lifetime after LeTID in both materials.

The capture cross-section ratios determined in this thesis are consistent with values reported in the literature by Morishige et al. ($26 \leq Q \leq 36$) [83], Nakayashiki et al. ($Q = 28.5$) [58] and Niewelt et al. ($Q \approx 35$) [84]. The reported Q values for the LeTID-specific defect are relatively large ($Q \gg 1$) and hence point towards the involvement of a metallic impurity in the LeTID process [85].

6.1.4 Photoluminescence imaging of mc-Si lifetime samples

Figure 6.3 shows a carrier lifetime image measured by PC-PLI of an mc-Si lifetime sample before and after LeTID. The grain boundaries in the degraded image appear brighter than the intra-grain areas and are less affected by LeTID. This is consistent with mobile metallic impurities causing LeTID, because of metal gettering by grain boundaries, which

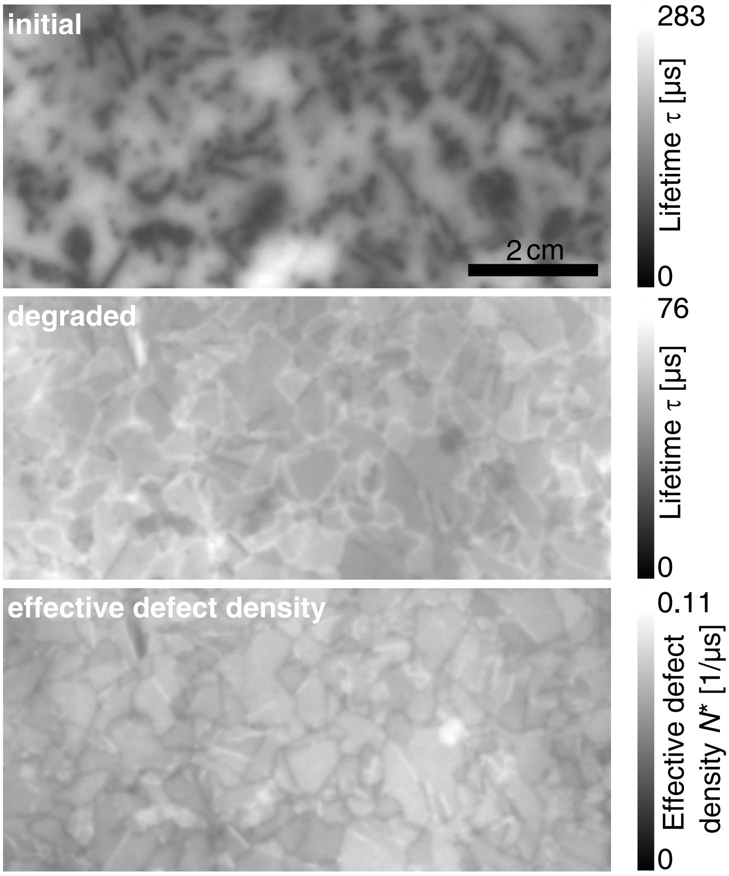

FIGURE 6.3: Carrier lifetime images measured by PC-PLI at a constant excess carrier density $\Delta n = 2 \times 10^{14}\,\mathrm{cm}^{-3}$ of an mc-Si lifetime sample before and after LeTID. The bottom image shows the calculated effective defect density $N^* = 1/\tau_{\mathrm{degraded}} - 1/\tau_{\mathrm{initial}}$. The grain boundaries in the degraded image show a higher lifetime and thus a lower effective defect density compared to the intra-grain areas.

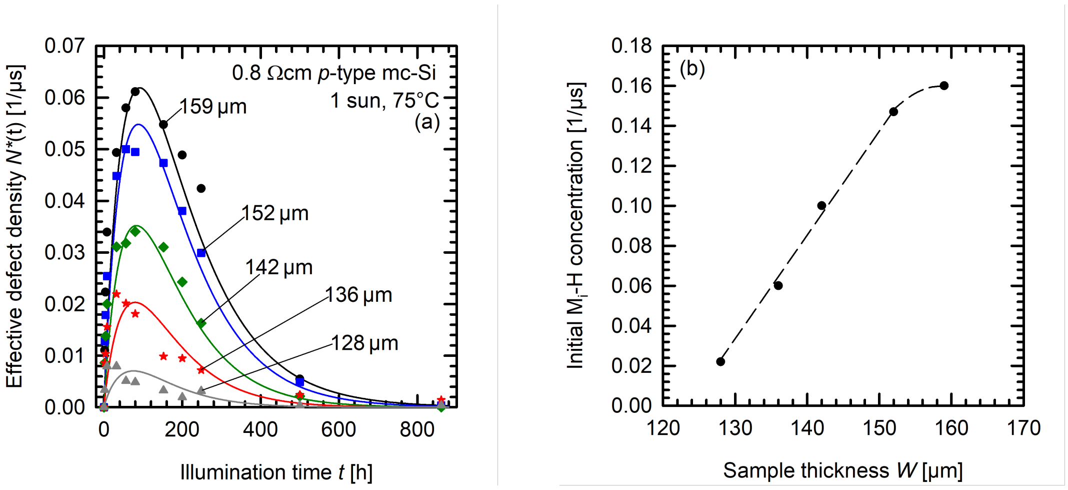

FIGURE 6.4: (a) Evolution of the effective defect density $N^*(t)$ of mc-Si wafers of various thicknesses (symbols) during illumination at 1 sun and at 75 °C. The solid lines are numerically simulated by solving equation 6.1 using the same diffusion coefficients of $D = 5 \times 10^{-11}\,\mathrm{cm^2 s^{-1}}$ for all curves shown. (b) Initial $\mathrm{M_i}$-H* concentration $c_1(0)$ used in our numerical simulation plotted versus the sample thickness W. The initial $\mathrm{M_i}$-H* concentration increases with increasing sample thickness. The dashed line is a guide to the eyes.

results in a metal concentration depletion in the direct vicinity of the grain boundaries.

6.2 Kinetics of the carrier lifetime regeneration

As described in section 4.6, the time evolution of the effective defect density of the species responsible for LeTID in mc-Si wafers shows a pronounced dependence on the wafer thickness. We use mc-Si lifetime samples with thicknesses between 128 µm to 159 µm illuminated at 1 sun light intensity at 75 °C. We numerically simulate the evolution of the effective defect density based on the defect model described above and compare the results with the measured data. Within this defect model, interstitial metal atoms $\mathrm{M_i}$ are assumed to be the lifetime-limiting species after complete LeTID, thus a direct proportionality between the effective defect density and the actual concentration of interstitial metal atoms is assumed. During prolonged ilumination at elevated temperature, the mobile $\mathrm{M_i}$ atoms diffuse to the wafer surfaces and to crystallographic defects. This mechanism explains the observed regeneration effect.

In the case that the mobile M_i atoms diffuse mainly to both wafer surfaces, the evolution of the defect density can be calculated in one dimension using the following differential equations:

$$\begin{aligned} &\frac{d}{dt} c_1(t) = -k_{12} \cdot c_1(t), \\ &\frac{\partial}{\partial t} c_2(x,t) - D \frac{\partial^2}{\partial x^2} c_2(x,t) = k_{12} \cdot c_1(t), \end{aligned} \tag{6.1}$$

with $c_2(x,t)$ being the defect density of the recombination-active defect M_i at time t and depth x, $c_1(t)$ the concentration of the M_i-H* complex, assumed to be homogeneously distributed throughout the wafer, k_{12} the rate constant of the M_i-H* dissociation and D the diffusion coefficient of M_i in crystalline silicon. In order to solve Eqn. 6.1, the time and space variables are discretized and the forward-time central-space (FTCS) method is implemented in the Octave software [86, 87]. As boundary condition it is assumed that the defect concentration $c_2(t)$ at the wafer surfaces equals zero at all times. The value of the dissociation rate constant $k_{12} = 4 \times 10^{-6}\,\mu s^{-1}$ has been chosen to reproduce the degradation kinetics at 1 sun illumination intensity at a temperature of 75 °C and is kept constant throughout this experiment. However, the value of the dissociation rate does not have a major impact on the extracted diffusion coefficient D. This is because the diffusion is much slower than the dissociation, and hence the diffusion is the limiting process. Since the effective defect density is extracted from lifetime measurements, which average over the entire sample thickness, this study displays the arithmetic mean of the calculated defect density over the sample thickness: $\overline{c_2}(t) \propto N^*(t)$.

Figure 6.4(a) shows the defect densities $\overline{c_2}(t)$ (solid lines) according to the solution of Eqns. 6.1 using a single diffusion coefficient of $D = 5 \times 10^{-11}\,\text{cm}^2\text{s}^{-1}$ for all sample thicknesses. Comparing the simulated solid lines with the experimentally determined $N^*(t)$ data, it can be seen that for this diffusion coefficient, the $N^*(t)$ dependence can be well described by the model used in this study. Note that an increasing deviation in the position of the maximum defect density with decreasing wafer thickness between the experimental data and the simulated data is observed. This deviation might be due to slightly higher excess carrier densities in thinner samples at constant illumination, however, it does not have a major impact on the extracted diffusion coefficient. The uncertainty of the extracted diffusion coefficient is estimated according to the measurement scatter to be $D = (5 \pm 2) \times 10^{-11}\,\mathrm{cm^2s^{-1}}$.

It is important to note that the good agreement between the measured and the calculated defect evolution in Fig. 6.4(a) requires the adjustment of the initial M_i-H* concentration $c_1(0)$ for the different curves, resulting in a strongly decreasing M_i-H* concentration with decreasing wafer thickness. Figure 6.4(b) shows the used values for the initial M_i-H* concentration $c_1(0)$ plotted versus the sample thickness W. For wafer thicknesses below 150 µm, $c_1(0)$ increases linearly with increasing thickness, whereas $c_1(0)$ seems to saturate for $W > 150\,\mu\mathrm{m}$. The pronounced dependence of the initial M_i-H* concentration on the wafer thickness is not expected from the defect model described above. One possible explanation of this unexpected behaviour is a surface gettering effect during the RTA step, which reduces the available M_i concentration for the complex formation. Thus, the thinner the wafer, the larger the fraction of impurities (M_i) trapped at the wafer surfaces would be. For thicker wafers ($> 150\,\mu\mathrm{m}$) the impact of the sample thickness on $c_1(0)$ decreases, because the impurities are rather gettered by crystallographic defects than by the wafer surfaces. However, note that the apparent saturation for $W > 150\,\mu\mathrm{m}$ is based on one data point, thus further studies including wafers with a broader sample thickness range are necessary.

In the following, we compare the extracted diffusion coefficient D with published data of diffusion coefficients of various relevant impurities in silicon. Note that most diffusion coefficients in the literature are not measured at a temperature of 75 °C. Hence, the ranges shown in Fig. 6.5 are extrapolated from measurements performed at higher temperatures, resulting in very large uncertainty ranges. In addition, the diffusion coefficients reported in the literature are determined for monocrystalline silicon only, and hence the diffusivities in mc-Si might deviate from the ones reported in the literature. As can be seen from Fig. 6.5, the diffusion coeffcients of mobile impurities in crystalline silicon vary over many orders of magnitude. Regarding the metallic impurities, only cobalt and nickel are reported to have diffusion coefficients within the same order of magnitude as determined from our thickness-dependent regeneration measurements. Interestingly, there are known recombination centers for cobalt and nickel in silicon. In particular, cobalt is known to form two recombination centers in silicon: one with an electron-to-hole capture cross-section ratio of $Q = 0.15$ and the other one with a value of $Q = 16$ [101]. However, the $Q = 16$ value reported for cobalt is lower than the values determined in this study and

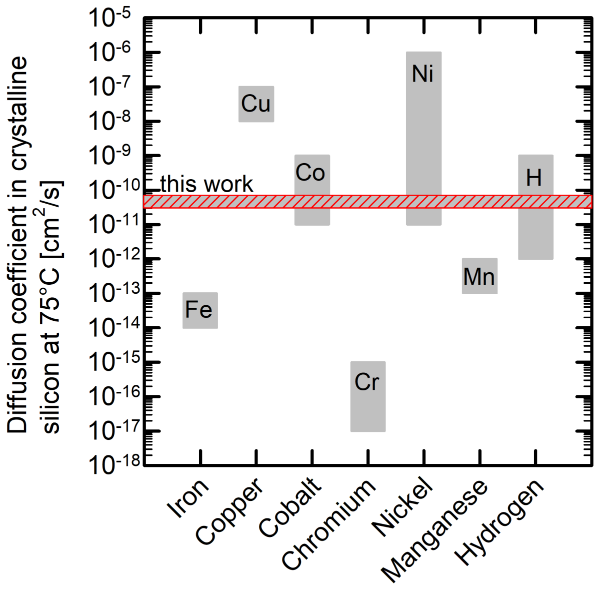

FIGURE 6.5: Comparison of the diffusion coefficient determined in this work (red shaded bar) with diffusion coefficients of various impurities in crystalline silicon extrapolated to a temperature of 75 °C. References: iron [88], copper [89, 90], cobalt [91, 92], titanium [88, 93], chromium [88, 94, 95], nickel [96, 97], manganese [98], and hydrogen [99, 100].

the values reported in the literature for the degradation in mc-Si. Nonetheless, this does not exclude cobalt as a likely candidate for one component of the lifetime limiting-defect in mc-Si. The capture cross-section ratio for cobalt defects was measured on intentionally contaminated monocrystalline silicon samples, thus there might be other cobalt-related recombination centers with a different Q value in the mc-Si samples studied in this work. Concerning nickel, there are no reported Q values for isolated nickel in silicon. This is because nickel is a very fast diffusor and tends to form precipitates as indeed described in the defect model in this study [102]. Nickel as a candidate for the metallic species is supported by Deniz et al. [103], who found nickel-containing defects in degraded PERC solar cells using energy dispersive X-ray spectroscopy (EDX).

6.3 Comparison with the literature

This section compares our presented experimental results on the LeTID effect and our resulting defect model with results published in the literature. Niewelt et al. [84] found that the total width of the metal concentration depletion zones (so-called denuded zones) around grain boundaries (cf. Fig. 6.3) ranges from 200 to 400 µm. They stated that the denuded zones are likely caused by internal gettering of a defect precursor species during the RTA treatment. Under this assumption, they ruled out some common metallic impurities based on their respective diffusivity. They found that cobalt remains as a likely candidate for the impurity, which is consistent with our results.

Luka et al. [104] showed that degraded mc-Si solar cells regenerate under dark annealing conditions at temperatures above 150 °C. However, the regenerated state after dark annealing was found unstable, because switching back to LeTID conditions (1 sun light intensity at 75 °C) resulted in a second degradation. More recently, Fung et al. [105, 106] performed experiments cycling between dark annealing conditions and laser illumination at elevated temperature. In contrast to the study of Luka et al., they performed multiple cycles and waited within each laser illumination cycle until the fully regenerated state was reached. They reported that the maximum LeTID defect density decreases with increasing cycle count and attributed this effect to a depletable reservoir state for the LeTID precursor, which was assumed to include hydrogen [106]. A depletable reservoir state is fully compatible with the LeTID model proposed within this thesis. There are two possible mechanisms: (i) hydrogen is released from hydrogen-containing bonds during dark annealing conditions and (ii) metal precipitates partly dissolve during dark annealing conditions and emit interstitial metal atoms M_i. Interestingly, Chan et al. [107] found that the LeTID extent is modulated by the applied dark annealing temperature. This effect could be explained by the partial out-diffusion of the interstitial metal atoms M_i to the wafer surfaces under dark annealing conditions. Our LeTID model is also consistent with observations from Chen et al. [108], who found that a degradation effect with similar characteristics as LeTID can be observed under dark annealing conditions. This might be due to a purely thermal dissociation of the M_i-H complexes.

There are experiments from Jensen et al. [109], who evaluated the role of hydrogen in the context of the high-temperature RTA treatment. They found that an RTA treatment is not necessary to trigger the LeTID defect, if the samples have previously been treated in a hydrogen plasma at temperatures between 350 and 375 °C, sufficient to introduce a small amount of hydrogen into the samples. They concluded that the dependence of LeTID on the high-temperature RTA treatment is due to the in-diffusion of hydrogen rather than the actual temperature profile. However, the samples from Jensen et al. [109] received a phosphorus diffusion step prior to the hydrogen plasma treatment. It can be conjectured that during the phosphorus diffusion step at temperatures around 835 °C the metal precipitates already started to dissolve into M_i, which after the subsequent hydrogenation led to the formation of M_i-H complexes. In addition to that, Jensen et al. [109] found that samples which were RTA treated without hydrogen-rich passivation layer being present, but with a subsequent hydrogen plasma treatment, only showed a small LeTID extent. This can be explained by the renewed precipitation of M_i during RTA, if during the cooling-down no hydrogen is present to bind the M_i.

6.4 Chapter summary

Based on the experimental findings in this study, we derived a novel defect model for the LeTID effect in mc-Si. The experiments showed that the defect activation cannot solely be attributed to hydrogen, but requires another most likely metallic species. Hence we propose metal-hydrogen complexes as precursors for the LeTID defect. Upon RTA treatment at sufficiently high temperature, latent precipitates of a metallic impurity dissolve and form interstitial metal atoms. Those metal atoms are immediately captured by hydrogen stemming from hydrogen-rich surface passivation layers, preventing the metal atoms from rejoining into metal precipitates. The so-formed metal-hydrogen complexes are no strong recombination centers or might even be completely recombination inactive. However, under illumination at elevated temperature those complexes dissociate and the free hydrogen is captured by other traps abundantly present in mc-Si. The remaining interstitial metal atoms are assumed to be highly recombination-active, thus causing the degradation of the carrier lifetime. Upon prolonged illumination at elevated temperature, the interstitial metal atoms diffuse mainly to the wafer surfaces and to crystallographic defects, where they are trapped. This diffusion process explains the observed regeneration of the carrier lifetime.

Experimental indications pointing towards the involvement of a metallic impurity include injection-dependent lifetime spectroscopy and photoluminescence imaging results. We found electron-to-hole capture cross-section ratios for the lifetime-limiting defect of $Q_A = 28 \pm 2$ and $Q_B = 29 \pm 4$ on two different mc-Si materials A and B. The relatively large value of $Q \gg 1$ points towards the involvement of a metallic impurity. In addition to that, photoluminescence imaging in the fully degraded state reveals that grain boundaries appear brigher than the intra-grain areas and are less affected by the degradation. This observation is consistent with mobile metallic impurities causing the lifetime degradation, because of metal gettering at the grain boundaries.

Finally, we modelled the pronounced dependence of the degradation extent and the regeneration kinetics based on the proposed defect model, where a mobile species diffuses to the wafer surfaces. Based on a lifetime study including samples with different thicknesses, we extracted the diffusion coefficient D of the mobile species at a temperature of 75 °C. The value of $D = (5 \pm 2) \times 10^{-11}\,\mathrm{cm^2 s^{-1}}$ renders cobalt and nickel likely candidates to be responsible for the LeTID effect.

Chapter 7

Summary and outlook

Within this thesis, we investigated the carrier lifetime degradation and regeneration in multicrystalline silicon (mc-Si) material under illumination at elevated temperature. The focus of this work is to uncover the underlying physical principle of the defect activation and to create a defect model based on it. In this thesis, for the first time, we examined the detailed dependence of the degradation kinetics on temperature and illumination intensity. The degradation proceeds in a fast and a slow stage, thus it does not follow a mono-exponential decay. Both the slow and fast degradation rates increase linearly with increasing illumination intensity. Increasing the temperature at constant illumination intensity leads to an increase of both rates according to an Arrhenius law. In contrast to the degradation, the subsequent regeneration proceeds in a single stage and after complete regeneration, the carrier lifetime is comparable or even higher compared to the initial state.

The process steps for the fabrication of both mc-Si solar cells and lifetime samples show a pronounced impact on the defect kinetics and the degradation extent. In this thesis, we showed for the first time that LeTID is greatly affected by rapid thermal annealing (RTA), typically used for the contact formation as the last process step in solar cell production. The degradation extent strongly increases with increasing RTA peak temperature. Furthermore, mc-Si samples which underwent a phosphorus gettering step, which is known to effectively remove metallic impurities from the silicon bulk, show a pronounced reduction of the degradation extent. Compared to samples which did not undergo a phoshorus gettering step, the degradation extent is four times less pronounced. In addition to that, the degradation extent shows a pronounced dependence on the applied dielectric passivation layers. We found that mc-Si lifetime samples passivated with

Al_2O_3 single layers only showed a negligible carrier lifetime instability. In contrast to that, samples passivated with an Al_2O_3/SiN_x stack passivation showed a pronounced carrier lifetime instability. Finally, we surprisingly found, that the carrier lifetime regeneration shows a strong dependence on the wafer thickness. The regeneration proceeds faster the thinner the wafer is.

Since silicon nitride films play a major role in the LeTID defect, we characterized their properties and their impact on LeTID in detail. We showed for the first time, that hydrogen diffusing from hydrogen-rich silicon nitride films into the silicon bulk during RTA shows a strong positive correlation with the degradation extent. The more hydrogen is introduced into the mc-Si material, the more pronounced is the observed degradation. The experiments in this thesis revealed that most hydrogen is introduced from silicon-rich silicon nitride layers with a refractive index n between 2.3 and 2.5. For both higher and lower refractive indices (i.e. for higher and lower silicon-to-nitrogen ratios), the introduced hydrogen amount decreases. In addition to that, the degradation extent also depends on the film thickness of the silicon nitride film. The degradation extent increases with increasing film thickness, however for film thicknesses larger than 105 nm the degradation extent saturates.

Based on the experimental findings of this thesis, we introduced a novel defect model describing the LeTID defect physics. The experimental results showed that the LeTID defect cannot be solely attributed to the in-diffusion of hydrogen into the silicon bulk during RTA treatment nor by metallic impurities, despite strong indications that both components are involved. Therefore, the defect model assumes metal-hydrogen complexes as precursors of the LeTID-specific defects. These complexes are assumed to dissociate upon illumination at elevated temperature into interstitial metal atoms and hydrogen. The free hydrogen binds to other traps abundantly present in mc-Si and the remaining interstitial metal atoms limit the carrier lifetime. The regeneration is explained by the diffusion of the interstitial metal atoms to the wafer surfaces and to crystallographic defects, where they are trapped. The proposed defect model is compared to results from the literature and is found to consistently describe most experimental findings.

Based on the results of this thesis, we proposed several pathways for avoiding lifetime instabilities in mc-Si. There are three main options: (i) Improve the material quality, in order to reduce the concentration of metallic impurities, (ii) to use thinner mc-Si wafers and (iii) to adapt process steps during solar cell fabrication. Especially the deposition of the SiN_x layers offers a powerful tool to avoid LeTID. Using nearly-stoichiometric SiN_x films and/or reducing the layer thickness results in a reduced LeTID extent.

There are several new questions that arise from the results presented in this thesis. We examined the hydrogen in-diffusion into the silicon bulk from SiN_x single layers. However, the impact of Al_2O_3 interlayers between SiN_x and the silicon bulk, as widely used in solar cells, on the hydrogen diffusion is not well understood, since Al_2O_3 might act as a diffusion barrier. In addition, the question arises whether hydrogen-correlated lifetime-limiting defects also exist in other silicon materials such as float-zone silicon and Czochralski-grown silicon. Further questions arise regarding the practical implementation of the pathways we proposed for avoiding LeTID. Since the peak temperature during RTA treatment is an important parameter for the metal contact formation, lowering the peak temperature could result in increased series resistance. Further research is necessary for the optimization of the metal pastes applied during screen-printing for the use at lower RTA peak temperatures. In addition to that, reducing the hydrogen in-diffusion into the silicon bulk by adjusting the SiN_x layers applied during solar cell fabrication could result in lower surface passivation quality and altered optical properties of the SiN_x layer. Further research is needed to find the optimum between suppressing LeTID on the one hand and a high surface passivation quality as well as good anti-reflective properties and low absorption of the SiN_x layer on the other hand.

Bibliography

[1] B. Burger, K. Kiefer, C. Kost, S. Nold, S. Philipps, R. Preu, J. Rentsch, T. Schlegl, G. Stryi-Hipp, G. Willeke, H. Wirth, and W. Warmuth. Fraunhofer ISE: Photovoltaics report, 2019.

[2] M. A. Green, Y. Hishikawa, E. D. Dunlop, D. H. Levi, J. Hohl-Ebinger, M. Yoshita, and A. W. Y. Ho-Baillie. Solar cell efficiency tables (version 53). *Progress in Photovoltaics: Research and Applications*, 27:3–12, 2019. doi: 10.1002/pip.3102.

[3] International technology roadmap for photovoltaic (ITRPV), 2019. 10th Edition.

[4] F. Schindler, A. Fell, R. Müller, J. Benick, A. Richter, F. Feldmann, P. Krenckel, S. Riepe, M. C. Schubert, and S. W. Glunz. Towards the efficiency limits of multicrystalline silicon solar cells. *Solar Energy Materials and Solar Cells*, 185:198–204, 2018. doi: 10.1016/j.solmat.2018.05.006.

[5] J. Schmidt, B. Veith, and R. Brendel. Effective surface passivation of crystalline silicon using ultrathin Al_2O_2 films and Al_2O_2/SiN_x stacks. *physica status solidi (RRL) - Rapid Research Letters*, 52:287–289, 2009. doi: 10.1002/pssr.200903272.

[6] K. Ramspeck, S. Zimmermann, H. Nagel, A. Metz, Y. Gassenbauer, B. Birkmann, and A. Seidl. Light induced degradation of rear passivated mc-Si solar cells. In WIP, editor, *27th European Photovoltaic Solar Energy Conference*, pages 861–865, Munich, 2012. WIP.

[7] J. Schmidt, A. G. Aberle, and R. Hezel. Investigation of carrier lifetime instabilities in Cz-grown silicon. In IEEE, editor, *26th IEEE Photovoltaic Specialists Conference*, pages 13–18, New York, 1997.

[8] S. W. Glunz, S. Rein, W. Warta, J. Knobloch, and W. Wettling. On the degradation of Cz-silicon solar cells. In WIP, editor, *2nd World Conference on Photovoltaic Energy Conversion*, pages 1343–1346, Munich, 1998.

[9] J. Schmidt and K. Bothe. Structure and transformation of the metastable boron- and oxygen-related defect center in crystalline silicon. *Physical Review B*, 69:3302, 2004. doi: 10.1103/PhysRevB.69.024107.

[10] L. J. Geerligs and D. Macdonald. Dynamics of light-induced FeB pair dissociation in crystalline silicon. *Applied Physics Letters*, 85:5227–5229, 2004. doi: 10.1063/1.1823587.

[11] J. Schmidt. Effect of dissociation of iron-boron pairs in crystalline silicon on solar cell properties. *Progress in Photovoltaics: Research and Applications*, 13:325–331, 2005. doi: 10.1002/pip.594.

[12] F. Fertig, K. Krauß, and S. Rein. Light-induced degradation of PECVD aluminium oxide passivated silicon solar cells. *physica status solidi (RRL) - Rapid Research Letters*, 9:41–46, 2015. doi: 10.1002/pssr.201409424.

[13] F. Kersten, P. Engelhart, H.-C. Ploigt, A. Stekolnikov, T. Lindner, F. Stenzel, M. Bartzsch, A. Szpeth, K. Petter, J. Heitmann, and J. W. Müller. Degradation of multicrystalline silicon solar cells and modules after illumination at elevated temperature. *Solar Energy Materials and Solar Cells*, 142:83–86, 2015. doi: 10.1016/j.solmat.2015.06.015.

[14] F. Chigondo. From metallurgical-grade to solar-grade silicon: An overview. *Silicon*, 10:789–798, 2018. doi: 10.1007/s12633-016-9532-7.

[15] Y. Dazhou. Siemens process. In Deren Yang, editor, *Handbook of Photovoltaic Silicon*, volume 42, pages 1–32. Springer Berlin Heidelberg, Berlin, Heidelberg, 2017. doi: 10.1007/978-3-662-52735-1_4-1.

[16] T. Saito, A. Shimura, and S. Ichikawa. A new directional solidification technique for polycrystalline solar grade silicon. In IEEE, editor, *15th Photovoltaic Specialists Conference*, pages 576–580, 1981.

[17] Y. P. B. Mouafi, B. Herzog, and G. Hahn. Effect of the crucible and its coating on the red zone in multicrystalline silicon - analysis on solar cell level. In WIP, editor, *29th European Photovoltaic Solar Energy Conference*, pages 780–785, Munich, 2014. WIP.

[18] W. Kwapil, A. Zuschlag, I. Reis, I. Schwirtlich, S. Meyer, R. Zierer, R. Krain, F. M. Kießling, M. Schumann, C. Schmid, and S. Riepe. Influence of crucible and coating on the contamination of directionally solidified silicon: First results of the german research network "SolarWins". In WIP, editor, *27th European Photovoltaic Solar Energy Conference*, pages 627–635, Munich, 2012. WIP.

[19] C. W. Lan, W. C. Lan, T. F. Lee, A. Yu, Y. M. Yang, W. C. Hsu, B. Hsu, and A. Yang. Grain control in directional solidification of photovoltaic silicon. *Journal of Crystal Growth*, 360:68–75, 2012. doi: 10.1016/j.jcrysgro.2012.01.007.

[20] Y. M. Yang, A. Yu, B. Hsu, W. C. Hsu, A. Yang, and C. W. Lan. Development of high-performance multicrystalline silicon for photovoltaic industry. *Progress in Photovoltaics: Research and Applications*, 23:340–351, 2015. doi: 10.1002/pip.2437.

[21] W. Zulehner. Czochralski growth of silicon. *Journal of Crystal Growth*, 65:189–213, 1983. doi: 10.1016/0022-0248(83)90051-9.

[22] A. Borghesi, B. Pivac, A. Sassella, and A. Stella. Oxygen precipitation in silicon. *Journal of Applied Physics*, 77:4169–4244, 1995. doi: 10.1063/1.359479.

[23] I. Yonenaga, K. Sumino, and K. Hoshi. Mechanical strength of silicon crystals as a function of the oxygen concentration. *Japanese Journal of Applied Physics*, 56: 2346–2350, 1984. doi: 10.1063/1.334272.

[24] R. Falster and W. Bergholz. The gettering of transition metals by oxygen-related defects in silicon. *Journal of The Electrochemical Society*, 137:1548, 1990. doi: 10.1149/1.2086709.

[25] H. Fischer and W. Pschunder. Investigation of photon and thermal induced changes in silicon solar cells. In IEEE, editor, *10th IEEE PVSC*, page 404, 1974.

[26] T. Niewelt, J. Schön, W. Warta, S. W. Glunz, and M. C. Schubert. Degradation of crystalline silicon due to boron–oxygen defects. *IEEE Journal of Photovoltaics*, 7: 383–398, 2017. doi: 10.1109/JPHOTOV.2016.2614119.

[27] H. C. Theuerer. Method of processing semiconductive materials, 1962. U.S. Patent 3060123A.

[28] G. Lasher and F. Stern. Spontaneous and stimulated recombination radiation in semiconductors. *Physical Review*, 133:A553–A563, 1964. doi: 10.1103/PhysRev.133.A553.

[29] P. P. Altermatt, F. Geelhaar, T. Trupke, X. Dai, A. Neisser, and E. Daub. Injection dependence of spontaneous radiative recombination in crystalline silicon: Experimental verification and theoretical analysis. *Applied Physics Letters*, 88:261901, 2006. doi: 10.1063/1.2218041.

[30] A. R. Beattie and P. T. Landsberg. Auger effect in semiconductors. *Proceedings of the Royal Society of London. Series A. Mathematical and Physical Sciences*, 249: 16–29, 1959. doi: 10.1098/rspa.1959.0003.

[31] L. Huldt. Band-to-band Auger recombination in indirect gap semiconductors. *Physica Status Solidi (a)*, 8:173–187, 1971. doi: 10.1002/pssa.2210080118.

[32] A. Haug. Carrier density dependence of Auger recombination. *Solid-State Electronics*, 21:1281–1284, 1978. doi: 10.1016/0038-1101(78)90193-4.

[33] J. Dziewior and W. Schmid. Auger coefficients for highly doped and highly excited silicon. *Physica Status Solidi (a)*, 31:346–348, 1977. doi: 10.1063/1.89694.

[34] M. J. Kerr and A. Cuevas. General parameterization of Auger recombination in crystalline silicon. *Journal of Applied Physics*, 91:2473–2480, 2002. doi: 10.1063/1.1432476.

[35] A. Richter, S. W. Glunz, F. Werner, J. Schmidt, and A. Cuevas. Improved quantitative description of Auger recombination in crystalline silicon. *Physical Review B*, 86:187, 2012. doi: 10.1103/PhysRevB.86.165202.

[36] B. A. Veith-Wolf, S. Schäfer, R. Brendel, and J. Schmidt. Reassessment of intrinsic lifetime limit in n-type crystalline silicon and implication on maximum solar cell efficiency. *Solar Energy Materials and Solar Cells*, 186:194–199, 2018. doi: 10.1016/j.solmat.2018.06.029.

[37] W. Shockley and W. T. Read. Statistics of the recombinations of holes and electrons. *Physical Review*, 87:835–842, 1952. doi: 10.1103/PhysRev.87.835.

[38] R. N. Hall. Electron-hole recombination in germanium. *Physical Review*, 87:387, 1952. doi: 10.1103/PhysRev.87.387.

[39] A. Schlachetzki. *Halbleiter-Elektronik: Grundlagen und moderne Entwicklung*. Teubner-Studienbücher Angewandte Physik. Teubner, Stuttgart, 1990. ISBN 3-519-03070-5.

[40] S. Rein. *Lifetime Spectroscopy: A Method of Defect Characterization in Silicon for Photovoltaic Applications*, volume 85 of *Springer Series in Material Science*. Springer-Verlag Berlin Heidelberg, Berlin, Heidelberg, 2005. ISBN 3-540-25303-3. doi: 10.1007/3-540-27922-9.

[41] V. V. Voronkov, R. Falster, K. Bothe, B. Lim, and J. Schmidt. Lifetime-degrading boron-oxygen centres in p-type and n-type compensated silicon. *Journal of Applied Physics*, 110:063515, 2011. doi: 10.1063/1.3609069.

[42] J. D. Murphy and R. J. Falster. The relaxation behaviour of supersaturated iron in single-crystal silicon at 500 to 750°C. *Journal of Applied Physics*, 112:113506, 2012. doi: 10.1063/1.4767378.

[43] J. Schmidt. *Untersuchungen zur Ladungsträgerrekombination an den Oberflächen und im Volumen von kristallinen Silicium-Solarzellen*. PhD thesis, University of Hannover, Hannover, 1998.

[44] J. Schmidt and A. G. Aberle. Accurate method for the determination of bulk minority-carrier lifetimes of mono- and multicrystalline silicon wafers. *Journal of Applied Physics*, 81:6186–6199, 1997. doi: 10.1063/1.364403.

[45] A. B. Sproul. Dimensionless solution of the equation describing the effect of surface recombination on carrier decay in semiconductors. *Journal of Applied Physics*, 76:2851–2854, 1994. doi: 10.1063/1.357521.

[46] K. Bothe. *Oxygen-related trapping and recombination centres in boron-doped crystalline silicon*. PhD thesis, University of Hannover, Hannover, 2006.

[47] P. P. Altermatt, J. Schmidt, M. Kerr, G. Heiser, and A. G. Aberle. Exciton-enhanced Auger recombination in crystalline silicon under intermediate and high injection conditions. In WIP, editor, *16th European Photovoltaic Solar Energy Conference*, page 243, Munich, 2000. WIP.

[48] H. Nagel, C. Berge, and A. G. Aberle. Generalized analysis of quasi-steady-state and quasi-transient measurements of carrier lifetimes in semiconductors. *Journal of Applied Physics*, 86:6218–6221, 1999. doi: 10.1063/1.371633.

[49] S. Herlufsen, J. Schmidt, D. Hinken, K. Bothe, and R. Brendel. Photoconductance-calibrated photoluminescence lifetime imaging of crystalline silicon. *physica status solidi (RRL) - Rapid Research Letters*, 2:245–247, 2008. doi: 10.1002/pssr.200802192.

[50] H. Fujiwara. *Spectroscopic Ellipsometry*. John Wiley & Sons, Ltd, Chichester, UK, 2007. doi: 10.1002/9780470060193.

[51] E. D. Palik, editor. *Handbook of Optical Constants of Solids*. Elsevier, 1997. ISBN 9780125444156.

[52] A. W. Weeber, H. C. Rieffe, W. C. Sinke, and W. J. Soppe. Structural and passivating properties of SiN_x:H deposited using different precursor gases. In WIP, editor, *19th European Photovoltaic Solar Energy Conference*, pages 1005–1008, Munich, 2004. WIP.

[53] Z. Yin and F. W. Smith. Optical dielectric function and infrared absorption of hydrogenated amorphous silicon nitride films: Experimental results and effective-medium-approximation analysis. *Physical review. B, Condensed matter*, 42:3666–3675, 1990.

[54] E. J. Evers and F. H. P. M. Habraken. Determination of the hydrogen concentration in silicon nitride films with the resonant nuclear reaction 1H(15N, $\alpha\gamma$)12C. *Spectrochimica Acta Part B: Atomic Spectroscopy*, 39:1553–1556, 1984. doi: 10.1016/0584-8547(84)80181-0.

[55] M. Mayer. SIMNRA, a simulation program for the analysis of NRA, RBS and ERDA. In *AIP Conference Proceedings*, pages 541–544. AIP, 4-7 Nov 1998. doi: 10.1063/1.59188.

[56] W. Schröter, A. Döller, A. Zozime, Vitaly V. Kveder, M. Seibt, and E. Spiecker. Phosphorus diffusion gettering of metallic impurities in silicon: Mechanisms beyond segregation. *Solid State Phenomena*, 95-96:527–538, 2003. doi: 10.4028/www.scientific.net/SSP.95-96.527.

[57] J. D. Moschner, J. Henze, J. Schmidt, and R. Hezel. High-quality surface passivation of silicon solar cells in an industrial-type inline plasma silicon nitride deposition system. *Progress in Photovoltaics: Research and Applications*, 12:21–31, 2004. doi: 10.1002/pip.523.

[58] K. Nakayashiki, J. Hofstetter, A. E. Morishige, T.-T. A. Li, D. B. Needleman, M. A. Jensen, and T. Buonassisi. Engineering solutions and root-cause analysis for light-induced degradation in p-type multicrystalline silicon PERC modules. *IEEE Journal of Photovoltaics*, 6:860–868, 2016. doi: 10.1109/JPHOTOV.2016.2556981.

[59] C. E. Chan, D. N. R. Payne, B. J. Hallam, M. D. Abbott, T. H. Fung, A. M. Wenham, B. S. Tjahjono, and S. R. Wenham. Rapid stabilization of high-performance multicrystalline p-type silicon PERC cells. *IEEE Journal of Photovoltaics*, 6:1473–1479, 2016. doi: 10.1109/JPHOTOV.2016.2606704.

[60] R. Eberle, W. Kwapil, F. Schindler, M. C. Schubert, and S. W. Glunz. Impact of the firing temperature profile on light induced degradation of multicrystalline silicon. *physica status solidi (RRL) - Rapid Research Letters*, 10:861–865, 2016. doi: 10.1002/pssr.201600272.

[61] A. Zuschlag, D. Skorka, and G. Hahn. Degradation and regeneration in mc-Si after different gettering steps. *Progress in Photovoltaics: Research and Applications*, 25:545–552, 2017. doi: 10.1002/pip.2832.

[62] D. Sperber, A. Graf, A. Heilemann, A. Herguth, and G. Hahn. Bulk and surface instabilities in boron doped float-zone samples during light induced degradation treatments. *Energy Procedia*, 124:794–798, 2017. doi: 10.1016/j.egypro.2017.09.349.

[63] W. Kwapil, T. Niewelt, and M. C. Schubert. Kinetics of carrier-induced degradation at elevated temperature in multicrystalline silicon solar cells. *Solar Energy Materials and Solar Cells*, 173:80–84, 2017. doi: 10.1016/j.solmat.2017.05.066.

[64] S. Kleekajai, F. Jiang, M. Stavola, V. Yelundur, K. Nakayashiki, A. Rohatgi, G. Hahn, S. Seren, and J. Kalejs. Concentration and penetration depth of H introduced into crystalline Si by hydrogenation methods used to fabricate solar cells. *Journal of Electronic Materials*, 100:093517, 2006. doi: 10.1063/1.2363684.

[65] F. Kersten, J. Heitmann, and J. W. Müller. Influence of Al_2O_3 and SiN_x passivation layers on LeTID. *Energy Procedia*, 92:828–832, 2016. doi: 10.1016/j.egypro.2016.07.079.

[66] B. Sopori. Silicon solar-cell processing for minimizing the influence of impurities and defects. *Journal of Electronic Materials*, 31:972–980, 2002. doi: 10.1007/s11664-002-0030-x.

[67] P. Karzel, J. Junge, and G. Hahn. Mapping of hydrogen bond energies in EFG silicon samples by analysis of spatially resolved minority charge carrier lifetimes after annealing steps. In WIP, editor, *24th European Photovoltaic Solar Energy Conference*, Munich, 2009. WIP.

[68] J. Schmidt, M. Kerr, and A. Cuevas. Surface passivation of silicon solar cells using plasma-enhanced chemical-vapour-deposited SiN films and thin thermal SiO_2/plasma SiN stacks. *Semiconductor Science and Technology*, 16:164–170, 2001. doi: 10.1088/0268-1242/16/3/308.

[69] R. S. Bonilla, C. Reichel, M. Hermle, and P. R. Wilshaw. Extremely low surface recombination in 1 Ωcm n-type monocrystalline silicon. *physica status solidi (RRL) - Rapid Research Letters*, 11:1600307, 2017. doi: 10.1002/pssr.201600307.

[70] F. Jiang, M. Stavola, A. Rohatgi, D. Kim, J. Holt, H. Atwater, and J. Kalejs. Hydrogenation of Si from SiN_x(H) films: Characterization of H introduced into the Si. *Applied Physics Letters*, 83:931–933, 2003. doi: 10.1063/1.1598643.

[71] S. Dauwe. *Low-Temperature Surface Passivation of Crystalline Silicon and its Application to the Rear Side of Solar Cells*. PhD thesis, University of Hannover, Hannover, 2003.

[72] B. Lenkeit. *Elektronische und strukturelle Eigenschaften von Plasma-Siliziumnitrid zur Oberflächenpassivierung von siebgedruckten, bifazialen Silizium-Solarzellen*. PhD thesis, University of Hannover, Hannover, 2002.

[73] T. Lauinger. *Untersuchung und Optimierung neuartiger Plasmaverfahren zur Siliciumnitrid-Beschichtung von Silicium-Solarzellen*. PhD thesis, University of Hannover, Hannover, 2001.

[74] A. F. Holleman, E. Wiberg, and N. Wiberg. *Lehrbuch der anorganischen Chemie*. de Gruyter, Berlin, 102., stark umgearb. u. verb. Aufl. edition, 2007. doi: 10.1515/9783110177701.

[75] Vladimir V. Voronkov and Robert Falster. Formation, dissociation, and diffusion of various hydrogen dimers in silicon. *physica status solidi (b)*, 254:1600779, 2017. doi: 10.1002/pssb.201600779.

[76] D. C. Walter, D. Bredemeier, R. Falster, V. V. Voronkov, and J. Schmidt. Easy-to-apply methodology to measure the hydrogen concentration in boron-doped crystalline silicon. *Solar Energy Materials and Solar Cells*, 200:109970, 2019. doi: 10.1016/j.solmat.2019.109970.

[77] J. Hong, W. M. M. Kessels, W. J. Soppe, A. W. Weeber, W. M. Arnoldbik, and M. C. M. van de Sanden. Influence of the high-temperature “firing” step on high-rate plasma deposited silicon nitride films used as bulk passivating antireflection

coatings on silicon solar cells. *Journal of Vacuum Science & Technology B: Microelectronics and Nanometer Structures*, 21:2123, 2003. doi: 10.1116/1.1609481.

[78] H. F. W. Dekkers, L. Camel, G. Beaucarne, and W. Beyer. Diffusion mechanism of hydrogen through PECVD SiN_x:H for fast defect passivation of mc-Si solar cells. In WIP, editor, *20th European Photovoltaic Solar Energy Conference*, pages 721–724, Munich, 2005. WIP.

[79] J.-F. Lelièvre, J. Hofstetter, A. Peral, I. Hoces, F. Recart, and C. del Cañizo. Dissolution and gettering of iron during contact co-firing. *Energy Procedia*, 8:257–262, 2011. doi: 10.1016/j.egypro.2011.06.133.

[80] J. S. Kang and D. K. Schroder. Gettering in silicon. *Physica Status Solidi (a)*, 65: 2974–2985, 1989. doi: 10.1063/1.342714.

[81] A. Cuevas, M. Stocks, S. Armand, M. Stuckings, A. Blakers, and F. Ferrazza. High minority carrier lifetime in phosphorus-gettered multicrystalline silicon. *Applied Physics Letters*, 70:1017–1019, 1997. doi: 10.1063/1.118469.

[82] A. Bentzen and A. Holt. Overview of phosphorus diffusion and gettering in multicrystalline silicon. *Materials Science and Engineering: B*, 159-160:228–234, 2009. doi: 10.1016/j.mseb.2008.10.060.

[83] A. E. Morishige, M. A. Jensen, D. B. Needleman, K. Nakayashiki, J. Hofstetter, T.-T. A. Li, and T. Buonassisi. Lifetime spectroscopy investigation of light-induced degradation in p-type multicrystalline silicon PERC. *IEEE Journal of Photovoltaics*, 6:1466–1472, 2016. doi: 10.1109/JPHOTOV.2016.2606699.

[84] T. Niewelt, F. Schindler, W. Kwapil, R. Eberle, J. Schön, and M. C. Schubert. Understanding the light-induced degradation at elevated temperatures: Similarities between multicrystalline and floatzone p-type silicon. *Progress in Photovoltaics: Research and Applications*, 26:533–542, 2018. doi: 10.1002/pip.2954.

[85] D. Macdonald and L. J. Geerligs. Recombination activity of interstitial iron and other transition metal point defects in p- and n-type crystalline silicon. *Applied Physics Letters*, 85:4061–4063, 2004. doi: 10.1063/1.1812833.

[86] J. W. Eaton, D. Bateman, S. Hauberg, and R. Wehbring. *GNU Octave version 4.0.0 manual: a high-level interactive language for numerical computations*. 2015. URL `http://www.gnu.org/software/octave/doc/interpreter`.

[87] K. W. Morton and D. F. Mayers. *Numerical solution of partial differential equations: An introduction*. Cambridge Univ. Press, Cambridge, 2. ed. edition, 2012. doi: 10.1017/CBO9780511812248.

[88] H. Nakashima, T. Sadoh, H. Kitagawa, and K. Hashimoto. Diffusion and electrical properties of 3d transition-metal impurity series in silicon. *Materials Science Forum*, 143-147:761–766, 1993. doi: 10.4028/www.scientific.net/MSF.143-147.761.

[89] A. A. Istratov, C. Flink, H. Hieslmair, E. R. Weber, and T. Heiser. Intrinsic diffusion coefficient of interstitial copper in silicon. *Physical Review Letters*, 81:1243–1246, 1998. doi: 10.1103/PhysRevLett.81.1243.

[90] T. Heiser and A. Mesli. Determination of the copper diffusion coefficient in silicon from transient ion-drift. *Applied Physics A Solids and Surfaces*, 57:325–328, 1993. doi: 10.1007/BF00332285.

[91] D. Gilles. PhD thesis, University of Göttingen, Göttingen, 1987.

[92] J. Utzig and D. Gilles. Diffusion of cobalt in silicon. *Materials Science Forum*, 38-41:729–734, 1991. doi: 10.4028/www.scientific.net/MSF.38-41.729.

[93] S. Hocine and D. Mathiot. Diffusion and solubility of titanium in silicon. *Materials Science Forum*, 38-41:725–728, 1991. doi: 10.4028/www.scientific.net/MSF.38-41.725.

[94] N. T. Bendik, V. S. Garnyk, and L. S. Milkovski. *Sov. Phys. - Solid State*, page 150, 1970.

[95] W. Würker, K. Roy, and J. Hesse. Diffusion and solid solubility of chromium in silicon. *Materials Research Bulletin*, 9:971–977, 1974. doi: 10.1016/0025-5408(74)90178-0.

[96] M. K. Bakhadyrkhanov, S. Zainalidinov, and A. Khanidov. *Sov. Phys. Semicond.*, page 243, 1980.

[97] J. Lindroos, D. P. Fenning, D. J. Backlund, E. Verlage, A. Gorgulla, S. K. Estreicher, H. Savin, and T. Buonassisi. Nickel: A very fast diffuser in silicon. *Journal of Applied Physics*, 113:204906, 2013. doi: 10.1063/1.4807799.

[98] D. Gilles, W. Bergholz, and W. Schröter. Diffusion of manganese in silicon studied by deep–level transient spectroscopy and tracer measurements. *Journal of Applied Physics*, 59:3590–3593, 1986. doi: 10.1063/1.337042.

[99] A. Hara. Diffusion coefficient of hydrogen in silicon at an intermediate temperature. *Japanese Journal of Applied Physics*, 46:962–964, 2007. doi: 10.1143/JJAP.46.962.

[100] S. Bédard and L. J. Lewis. Diffusion of hydrogen in crystalline silicon. *Physical Review B*, 61:9895–9898, 2000. doi: 10.1103/PhysRevB.61.9895.

[101] S. Diez, S. Rein, T. Roth, and S. W. Glunz. Cobalt related defect levels in silicon analyzed by temperature- and injection-dependent lifetime spectroscopy. *Journal of Applied Physics*, 101:033710, 2007. doi: 10.1063/1.2433743.

[102] D. Macdonald. Impact of nickel contamination on carrier recombination in n- and p-type crystalline silicon wafers. *Applied Physics A Solids and Surfaces*, 81:1619–1625, 2005. doi: 10.1007/s00339-005-3371-5.

[103] H. Deniz, J. Bauer, and O. Breitenstein. Nickel precipitation in light and elevated temperature degraded multicrystalline silicon solar cells. *Solar RRL*, 2:1800170, 2018. doi: 10.1002/solr.201800170.

[104] T. Luka, S. Großer, C. Hagendorf, K. Ramspeck, and M. Turek. Intra-grain versus grain boundary degradation due to illumination and annealing behavior of multi-crystalline solar cells. *Solar Energy Materials and Solar Cells*, 158:43–49, 2016. doi: 10.1016/j.solmat.2016.05.061.

[105] T. H. Fung, C. E. Chan, B. J. Hallam, D. N. R. Payne, M. D. Abbott, and S. R. Wenham. Impact of annealing on the formation and mitigation of carrier-induced

defects in multi-crystalline silicon. *Energy Procedia*, 124:726–733, 2017. doi: 10.1016/j.egypro.2017.09.087.

[106] T. H. Fung, M. Kim, D. Chen, C. E. Chan, B. J. Hallam, R. Chen, D. N. R. Payne, A. Ciesla, S. R. Wenham, and M. D. Abbott. A four-state kinetic model for the carrier-induced degradation in multicrystalline silicon: Introducing the reservoir state. *Solar Energy Materials and Solar Cells*, 184:48–56, 2018. doi: 10.1016/j.solmat.2018.04.024.

[107] C. Chan, T. H. Fung, M. Abbott, D. Payne, A. Wenham, B. Hallam, R. Chen, and S. Wenham. Modulation of carrier-induced defect kinetics in multi-crystalline silicon PERC cells through dark annealing. *Solar RRL*, 1:1600028, 2017. doi: 10.1002/solr.201600028.

[108] D. Chen, M. Kim, B. V. Stefani, B. J. Hallam, M. D. Abbott, C. E. Chan, R. Chen, D. N. R. Payne, N. Nampalli, A. Ciesla, T. H. Fung, K. Kim, and S. R. Wenham. Evidence of an identical firing-activated carrier-induced defect in monocrystalline and multicrystalline silicon. *Solar Energy Materials and Solar Cells*, 172:293–300, 2017. doi: 10.1016/j.solmat.2017.08.003.

[109] M. A. Jensen, A. Zuschlag, S. Wieghold, D. Skorka, A. E. Morishige, G. Hahn, and T. Buonassisi. Evaluating root cause: The distinct roles of hydrogen and firing in activating light- and elevated temperature-induced degradation. *Journal of Applied Physics*, 124:085701, 2018. doi: 10.1063/1.5041756.

Appendix A

List of Publications

Publications arising from the work in this thesis:

Peer-reviewed journal papers

1. D. Bredemeier, D. Walter, S. Herlufsen, and J. Schmidt, Lifetime degradation and regeneration in multicrystalline silicon under illumination at elevated temperature, AIP Adv. **6**, 035119 (2016).
2. D. Bredemeier D. Walter, and J. Schmidt, Light-induced Lifetime Degradation in High-Performance Multicrystalline Silicon: Detailed Kinetics of the Defect Activation, Sol. Energ. Mat. Sol. Cells **173**, 2-5 (2017).
3. D. Bredemeier, D. Walter, and J. Schmidt, Possible Candidates for Impurities in mc-Si Wafers Responsible for Light-Induced Lifetime Degradation and Regeneration, Solar RRL **2**, 1700159 (2017).
4. L. Helmich, D. Walter, D. Bredemeier, R. Falster, V. V. Voronkov, and J. Schmidt, In-situ characterization of electron-assisted regeneration of Cz-Si solar cells, Sol. Energ. Mat. Sol. Cells **185**, 283-286 (2018).
5. D. Bredemeier, D. Walter, R. Heller, and J. Schmidt, Impact of hydrogen-rich silicon nitride material properties on light-induced lifetime degradation in multicrystalline silicon, Phys. Stat. Sol. RRL **13**, 1900201 (2019).
6. D. Walter, D. Bredemeier, R. Falster, V. V. Voronkov, and J. Schmidt, Easy-to-apply methodology to measure the hydrogen concentration in boron-doped crystalline silicon, Sol. Energ. Mat. Sol. Cells **200**, 109970 (2019).

7. M. Winter, D. Walter, D. Bredemeier, and J. Schmidt, Light-induced lifetime degradation effects at elevated temperature in Czochralski-grown silicon beyond boron-oxygen-related degradation, Sol. Energ. Mat. Sol. Cells **201**, 110060 (2019).
8. J. Schmidt, D. Bredemeier, and D. Walter, On the Defect Physics Behind Light and Elevated Temperature-Induced Degradation (LeTID) of Multicrystalline Silicon Solar Cells, IEEE J. Photovolt. **9**, 1497 (2019).

Conference Proceedings

1. D. Bredemeier, D. Walter, S. Herlufsen, and J. Schmidt, Measures for eliminating light-induced degradation in multicrystalline silicon, in: Proceedings of the 32nd EUPVSEC, (WIP, Munich, Germany), 2016.
2. D. Bredemeier, D. Walter, S. Herlufsen, and J. Schmidt, Understanding the light-induced lifetime degradation and regeneration in multicrystalline silicon, Energy Procedia **92**, 773-778 (2016).
3. D. Bredemeier, D. Walter, and J. Schmidt, Lifetime Degradation in Multicrystalline Silicon under Illumination at Elevated Temperature: Indications for the Involvement of Hydrogen, AIP Conf. Proc. **1999**, 130001 (2018).
4. D. Bredemeier, D. Walter, T. Pernau, O. Romer, and J. Schmidt, Production compatible remedy against LeTID in high-performance multicrystalline silicon solar cells, in: Proceedings of the 35th EUPVSEC, (WIP, Munich, Germany), 2018.
5. D. Walter, L. Herlmich, D. Bredemeier, V. V. Voronkov, R. Falster, and J. Schmidt, Lifetime evolution during regeneration in boron-doped Czochralski-silicon, in: Proceedings of the 35th EUPVSEC, (WIP, Munich, Germany), 2018.
6. D. Bredemeier, D. Walter, R. Heller, and J. Schmidt, Impact of Silicon Nitride Film Properties on Hydrogen In-Diffusion into Crystalline Silicon, in: Proceedings of the 36th EUPVSEC, (WIP, Munich, Germany), 2019.

Further peer-reviewed journal papers:

- F. Krause, D. Bredemeier, M. Schowalter, T. Mehrtens, T. Grieb, and A. Rosenauer, Using molecular dynamics for multislice TEM simulation of thermal diffuse scattering in AlGaN, Ultramicroscopy **189**, 124 (2018).

Appendix B

List of Awards

Received awards for results obtained in this thesis:

- Best Paper Award for the paper entitled ’Improved Understanding of Light-Induced Degradation and Regeneration in Multicrystalline Silicon Solar Cells’. (27th International Photovoltaic Science and Engineering Conference, PVSEC)
- EU PVSEC Student Award 2019 for the presentation ’Impact of Silicon Nitride Film Properties on Hydrogen In-Diffusion into Crystalline Silicon’. (36th European Photovoltaic Solar Energy Conference and Exhibition, EU PVSEC)

List of Figures

List of Tables

Appendix C

Danksagung

Abschließend möchte ich mich bei allen bedanken, die zum Gelingen dieser Arbeit beigetragen haben:

- Prof. Dr. Jan Schmidt für die sehr gute wissenschaftliche Betreuung und seine Hilfe beim Erstellen wissenschaftlicher Publikationen,
- Prof. Dr. Herbert Pfnür und Prof. Dr. Arthur Weeber für die freundliche Übernahme der Korreferate,
- Prof. Dr. Olaf Lechtenfeld für die Übernahme des Vorsitzes der Promotionskommission,
- Cornelia Marquardt für das Prozessieren der Silizium-Lebensdauerproben sowie
- Dr. René Heller vom Helmholtz-Zentrum Dresden-Rossendorf für die Ermöglichung und Durchführung von sowohl NRA als auch RBS Messungen.

Darüber hinaus möchte ich mich insbesondere bei meinen Bürokollegen Dr. Dominic Walter und Peter Giesel für die gute Arbeitsatmosphäre und für gute Diskussionen bedanken. Zudem bedanke ich mich bei allen weiteren Mitarbeitern des ISFH, insbesondere bei der Arbeitsgruppe Materialforschung.
Abschließend möchte ich mich bei Anja Bredemeier, Karl Bredemeier und Ursula Bredemeier, bei meiner Freundin Karo sowie allen hier nicht namentlich genannten Personen für ihre Unterstützung bedanken.

Appendix D

Curriculum vitae

Persönliche Daten

Name	Dennis Bredemeier
Anschrift	Dannenbergstraße 27, 30459 Hannover
Geburtsdatum	21. August 1990
Geburtsort	Bremen
Staatsangehörigkeit	deutsch

Schulbildung

1997 bis 2001	Grundschule, Grundschule am Ellenerbrokweg in Bremen
2001 bis 2003	Orientierungsstufe, Schule an der Graubündener Straße in Bremen
2003 bis 2009	Gymnasium, Hermann-Böse Gymnasium in Bremen

Universitätsausbildung

2009 bis 2012	Bachelorstudium der Physik an der Universität Bremen
2012 bis 2014	Masterstudium der Physik an der Universität Bremen

Anstellung

seit 2015	wissenschaftlicher Mitarbeiter Institut für Solarenergieforschung Hameln / Emmerthal (ISFH)
seit Dezember 2019	wissenschaftlicher Mitarbeiter Leibniz Universität Hannover, Institut für Festkörperphysik Abteilung Solarenergie